Properties of Nanoscale Biomaterials for Cancer Detection and Other Applications

Brian Lee Geist

Virginia Polytechnic Institute and State University

A dissertation submitted in partial fulfillment of the degree of

Doctor of Philosophy in Physics

Hans Robinson, chair

John Robertson, chair

Guy Indebetouw

Kyungwha Park

Kurt Zimmerman

Blacksburg, VA

April, 2009

Keywords: Surface-enhanced Raman spectroscopy, Ionic self-assembled multilayer films, DNA melting, Localized surface Plasmon resonance, Nanoscale biomaterials, cancer detection.

ABSTRACT

Properties of Nanoscale Biomaterials for Cancer Detection and Other Applications

Brian Lee Geist

The first thermal cycling experiments of ionic self-assembled multilayer (ISAM) films have been reported examining their survivability through repeated thermal cycles from -20° C to 120° C in ambient atmospheric conditions. The films were constructed from alternating layers of Nile Blue A and gold nanoparticles which provided a strong absorbance in the optical wavelength range. No degradation of the optical characteristics of the ISAM films was observed [1]. Techniques for measuring the capacitance and resistivity of various ISAM films have also been developed allowing for a more complete electrical characterization of ISAM films. Capacitance measurements enabled a calculation of the dielectric function and breakdown field strength of the ISAM films. The capacitance measurement technique was verified by measuring the dielectric function of a spin-coated thin film PMMA, which has a well characterized dielectric function [2]. Surface-enhanced Raman spectroscopy (SERS) has been studied as a possible detection method for malignant melanoma revealing spectral differences in blood sera from healthy horses and horses with malignant melanoma. A SERS microscope system was constructed with the capability of resolving the Raman signal from biologically important molecules such as beta-carotene and blood sera. The resulting Raman signals from sera collected from horses with malignant melanoma were found to have additional peaks not found in the Raman signals obtained from sera collected from healthy horses. A systematic analysis of the combination of absorbance and fluorescence signals of blood sera collected from populations of healthy dogs and dogs with cancer has resulted in a rapid and cost-effective method for monitoring protein concentrations that could possibly be used as part of a cancer screening process. This method was developed using the

accurate determination of protein concentrations in blood sera [3]. Finally, a novel method for measuring the melting point of DNA in solution using capacitance measurements is presented. This method allows for the determination of the melting temperature as well as the melting entropy and melting enthalpy of DNA strands. Two different short strands of DNA, 5'-CAAAATAGACGCTTACGCAACGAAAAC-3' along with its complement and 5'-GGAAGAGACGGAGGA-3' along with its complement were used to validate the technique as the characteristics of these strands could be modeled using theoretical methods. This experimental technique allows for the precise determination of the melting characteristics of DNA strands and can be used to evaluate the usefulness of theoretical models in calculating the melting point for particular strands of DNA. Additionally, a micro-fluidic device has been proposed that will allow for a rapid and cost-effective determination of the melting characteristics of DNA [4].

ACKNOWLEDGMENTS

My journey through graduate school has been one of many challenges and was navigable only with the help of many teachers, mentors and fellow students. My utmost respect and admiration is due to Professors Blecher and Täuber for their commitment to teaching difficult subjects to a student who at times struggled to truly understand the course material. Thank you for caring enough to be dedicated to my learning and for your love of teaching. Dr. Spillman provided support, guidance and friendship introducing me to research and other scientists working in bio-physics. Thank you for your tireless efforts in teaching me how to present ideas. My committee members have been a constant source of support and have helped me to tie different areas of science together. Thank you, Professor Zimmerman and Professor Indebetouw, for your attentiveness to my work as I was crafting this dissertation. To my advisors, Professor Robertson and Professor Robinson—Dr. Bob, your loyalty and friendship, as well as your love of science have been an inspiration for me. Thank you for your example and for the time to work with you against cancer. Dr. Robinson, your commitment to learning and understanding of science and how it explains what we observe has always been exemplary. I hope to emulate it throughout my career as a scientist. Thank you for your honesty and commitment to our research and for the support and effort in developing my abilities as a scientist. Your friendship is very valuable to me.

My family and many friends have also been a huge support to me in this endeavor. Jason Ridley, Chris Thomas and Cemil Durak especially have always been there for whatever was needed. To my parents, my first teachers, I wouldn't be anywhere without you and your love. I hope I provide you with joy. To my wife Leslie, and our little girls, I love you and dedicate my effort to you. All of you have been a gift from God.

Chapter 1 INTRODUCTION....1-1
The fabrication and characterization of ionic self-assembled multilayer (ISAM) films with applications....1-2
Surface-enhanced Raman spectroscopy (SERS) of serum for the detection of melanoma....1-4
Cancer detection and treatment methods using optical and electrical techniques....1-5
Absorbance and fluorescence measurements of serum....1-5
Dielectric function measurements of DNA melting point....1-8
Chapter 2 ANALYSIS OF ISAM FILMS WITH APPLICATIONS....2-10
Introduction....2-10
Thermal cycling and optical characterization techniques of ISAM films....2-10
Experimental procedure....2-12
Results and discussion....2-15
A method for measuring the capacitance of ISAM films....2-20
Theoretical background....2-22
Materials used for fabrication....2-24
Experimental design....2-26
Capacitance measurement and dielectric function calculation....2-27
ISAM films with heparin....2-32
Electric field breakdown determination....2-34
Summary....2-36
Chapter 3 LOCALIZED SURFACE PLASMON RESONANCE (LSPR) AND SURFACE-ENHANCED RAMAN SPECTROSCOPY (SERS)....3-38
Medical applications for surface-enhanced Raman spectroscopy....3-38
Scientific interest....3-38
Theory of LSPR....3-39

Application to SERS– Fabrication of substrates 3-41
Description of experimental setup 3-42
Results of standards 3-43
Results of sera measurements 3-46
Outlook for future success in cancer detection 3-48
Chapter 4 ABSORBANCE AND FLUORESCENCE MEASUREMENTS OF SERUM 4-49
Sample collection and processing techniques 4-50
Data analysis and processing techniques 4-52
Value of technique 4-62
Conclusion 4-68
Chapter 5 DIELECTRIC FUNCTION MEASUREMENTS OF THE MELTING POINT OF DNA 5-70
The structure of DNA 5-70
Methods and materials 5-72
Determination of T_m 5-72
Sample preparation 5-73
Description of fluid cell 5-74
Measurement electrodes 5-75
Calibration of fluid cell 5-76
Experiment configuration 5-77
Experiment results 5-79
Analysis of results 5-87
Comparison with theoretical models 5-88
Suggestions for future work 5-90
REFERENCES 5-93

LIST OF FIGURES

Figure 1-1 ISAM film diagram for the buildup of multilayer assemblies.....1-2

Figure 1-2 ISAM film processing.....1-3

Figure 2-1 Thermal cycling process used to test the Nile Blue A – Au film.....2-13

Figure 2-2 Schematic of resistivity measurement setup.....2-15

Figure 2-3 Absorbance of unheated Nile Blue A – Au 30 bilayer sample.....2-16

Figure 2-4 Maximum absorbance of Nile Blue A – Au film.....2-17

Figure 2-5 Thermal Cycling Effects on Nile Blue A – Au film (-20° to 120° C).....2-18

Figure 2-6 Voltage versus Current for 50 Bilayers of Nile Blue A – Au film.....2-18

Figure 2-7 Index of refraction and the extinction coefficient of Nile Blue A – Au film....2-19

Figure 2-8 Absorbance versus wavelength calculated from the extinction coefficient.....2-20

Figure 2-9 Schematic illustration of the guarded and guard electrodes.....2-23

Figure 2-10 AFM phase images.....2-25

Figure 2-11 (a) Top view of the prepared sample and (b) its schematic illustration.....2-26

Figure 2-12 Capacitance measurements of ISAM films.....2-28

Figure 2-13 Real dielectric function measurements.....2-29

Figure 2-14 Real dielectric function measurements of 75 bilayer of ISAM film.....2-31

Figure 2-15 Densification process of the ISAM film over a broad temperature range.....2-32

Figure 2-16 Dielectric function values of 75 bilayers of heparin and PDDA film.....2-33

Figure 2-17 Real dielectric function measurements of PMMA film.....2-34

Figure 2-18 Breakdown field (kV mm−1) of ISAM films.....2-36

Figure 3-1 SEM image of a silver coated substrate.....3-42

Figure 3-2 Sketch of experimental setup.....3-43

Figure 3-3 Raman spectra of Beta carotene 3-44

Figure 3-4 SERS spectra of Beta-carotene..... 3-45

Figure 3-5 SERS spectra of Nile Blue A..... 3-45

Figure 3-6 SERS spectra of sera samples from horses 3-47

Figure 3-7 SERS spectra of a serum sample from a horse with malignant melanoma..... 3-47

Figure 3-8 Individual SERS spectra of a serum sample collected from a healthy horse..... 3-48

Figure 4-1 Average UV absorbance spectra for diluted serum..... 4-52

Figure 4-2 Absorbance spectra of reference solutions for primary serum proteins..... 4-53

Figure 4-3 Fluorescence spectra of reference solutions for primary serum proteins..... 4-54

Figure 4-4 Linear absorbance of serum components..... 4-55

Figure 4-5 Scattering contributions to serum absorbance spectra..... 4-56

Figure 4-6 Fluorescence of serum components..... 4-57

Figure 4-7 Fitting typical serum spectra..... 4-58

Figure 4-8 Spectroscopic estimates of albumin concentration in mixtures..... 4-59

Figure 4-9 Spectroscopic estimates of globulins in mixtures..... 4-59

Figure 4-10 Spectroscopic estimates of total protein..... 4-60

Figure 4-11 Spectroscopic estimates of trace hemoglobin concentrations..... 4-60

Figure 4-12 Identifying selected low risk patients..... 4-61

Figure 4-13 Screening for cancer based on hemoglobin and total protein concentrations. 4-62

Figure 4-14 Tracking temporal changes in serum composition for a dog with cancer..... 4-66

Figure 5-1 Plastic dielectric fluid cell..... 5-75

Figure 5-2 Configuration of measurement electrodes..... 5-76

Figure 5-3 Experimental setup..... 5-77

Figure 5-4 (a) Real ε *vs.* temperature for buffer solution at various frequencies..... 5-79

Figure 5-5 Real ε vs. temperature for buffered sequence 1 and 2.....5-81

Figure 5-6 T_ms for both sequences.....5-83

Figure 5-7 Real ε difference between ds and ss states for sequence 1 and 2.....5-84

Figure 5-8 Calculated melting temperature, Tm, for DNA sequence 1 and 2.....5-85

Figure 5-9 Mean and SD for predicted T_m values for sequence 1 and 2.....5-86

Figure 5-10 Advanced device concept sketches.....5-91

LIST OF TABLES

Table 2-1 Dielectric function and breakdown field values of selected materials……..……2-24

Table 4-1 Correlation coefficients between canine serum protein concentrations and health group*.....4-65

Table 4-2 Medical history of a dog treated for lymphoma.....4-67

Table 5-1 Quadratic fits to real ε vs. temperature in °C for the buffer solution used to suspend the DNA sequences.....5-80

Table 5-2 Modified sigmoid function (Equation 5-4) fits to real ε vs. temperature in °C for the buffered solutions with DNA sequences 1 and 2.....5-82

Table 5-3 Real ε of ds and ssDNA for sequences 1 and 2.....5-83

Table 5-4 Base pair fractions and number of bp in the two sequences.....5-84

Table 5-5 Relationship of references to histogram bars in Figure 5-8.....5-86

Chapter 1 INTRODUCTION

This dissertation can be broken down into two paths. The first part of my research covered ionic self-assembled multilayer (ISAM) material properties and characterization techniques [1, 2]. The aging of an ISAM film through repeated thermal cycling is presented. Also, a method for measuring the conductivity as well as a method for measuring the capacitance of these films is developed. Theses two methods make measurements of nanoscale films that previously could only be made on macroscopic materials.

The second part of my research has been devoted to studying optical and electrical methods of cancer detection and treatment. It includes a study using absorbance and fluorescence measurements to quantify blood constituent ratios to predict the presence of cancer [3]. This optical method has been shown to be as accurate as other more complicated methods such as the common blood panel while providing results more quickly and in a more cost-effective manner. Also presented is the feasibility of using surface-enhanced Raman spectroscopy to detect malignant melanoma. This involved the development of a Raman microscope system and the construction of substrates that would be suitable for creating a surface enhancement effect. Blood serum samples from healthy horses and from horses with melanoma were compared for differences. Finally, the development of a technique for determining the melting point of DNA by using a capacitance bridge which could be useful in developing treatment techniques for certain cancers[4].

The fabrication and characterization of ionic self-assembled multilayer (ISAM) films with applications

ISAM films have been demonstrated for many specific applications [5, 6]. These films can be fabricated on glasses, metals and alloys, ceramics and polymers using a dipping technique to modify the performance (optical, electrical, tribological, thermal, magnetic and electrostatic) of the materials and also protect the surface from the environmental effects (e.g., humidity, ultraviolet light, temperature, static and dynamic forces, etc) [5-8].

Figure 1-1 shows the basic concept behind the ionic self-assembled (ISA) process. On the left, the substrate surface has been thoroughly cleaned using a piranha bath [9]. Typically, cleaning of the substrate exposes functional groups at the surface and thus effectively produces a surface that is charged in aqueous solution. The substrate is then dipped into a solution containing a polyelectrolyte. A positively charged polyelectrolyte (e.g., PDDA, Nile Blue A, etc) bonds to the negatively charged surface.

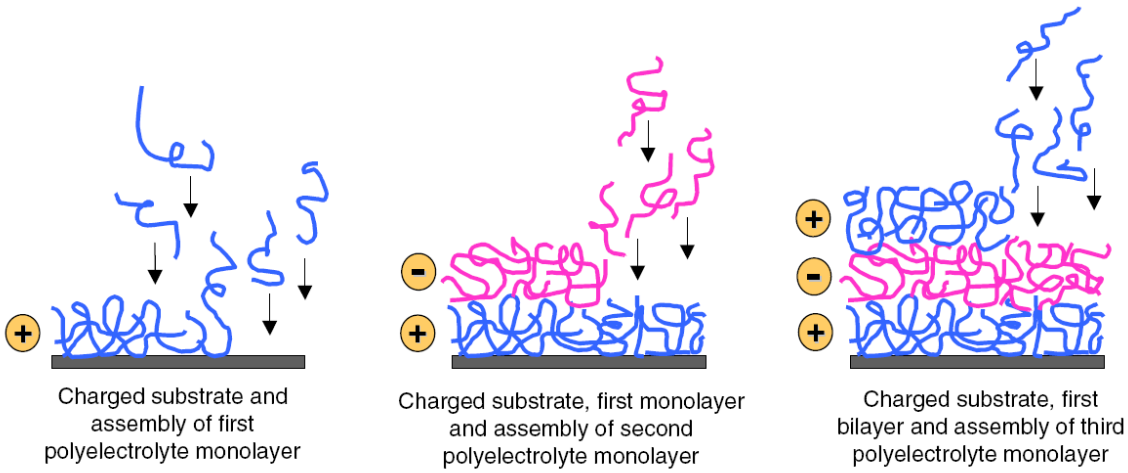

Figure 1-1 ISAM film diagram for the buildup of multilayer assemblies by consecutive adsorption of cationic and anionic molecule-based poly-electrolytes

Subsequent anionic (e.g., PS-119, heparin, etc) and cationic monolayers are added in bilayer pairs, by alternately dipping the substrate into those positively and negatively charged solutions to produce a multilayer thin-film structure as shown in Figure 1-2. Physical, chemical and physicochemical results show that the molecular order of each individual monolayer is fairly high [5], in much the same way that electrical charge on a free conducting surface distributes itself uniformly over the surface in order to minimize total system energy. Between each dipping step, the surface of the substrate is flushed with ultrapure water to remove loose particles that may be held within the residual liquid solution on the substrate and that are not part of the ionically attached thin film on the surface [6, 7]. Nanoparticles, (e.g., Pt,Au, CdSe,GaAs, TiO2, Al2O3, etc) can also be incorporated into the ISAM film as substitutes to either or both of the polymer layers to provide a wider range of possible nanoparticle/polymer combinations, and resulting in thin-film properties as shown schematically in Figure 1-2 [6, 7].

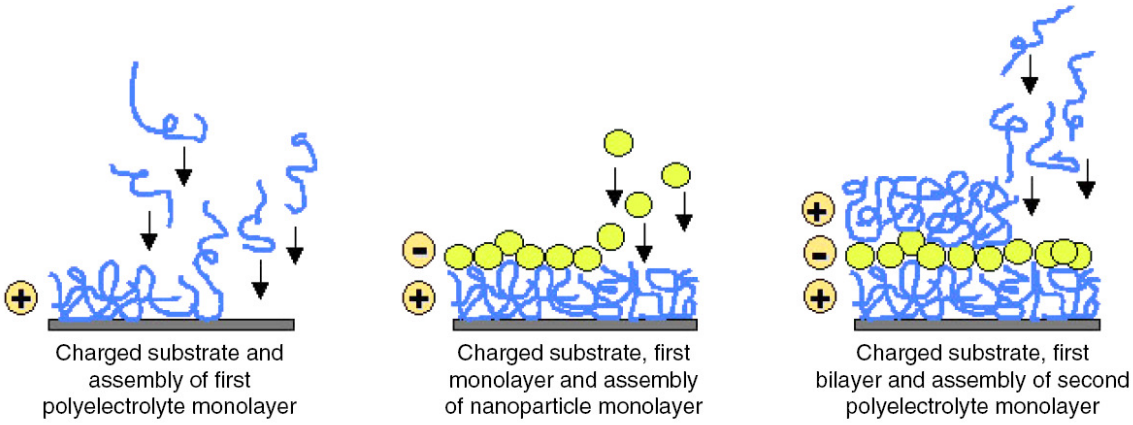

Figure 1-2 ISAM film processing of polymers in combination with nanocluster quantum dots allows a wide variation of coating properties

The study of ISAM films has led to several findings that will be of use to scientists and engineers who develop or produce these films: A method for testing film survivability through repeated temperature cycles has been developed. Techniques for measuring the capacitance and resistivity of ISAM films have also been created which will allow researchers to better characterize the electrical properties of nanoscale thin films.

Surface-enhanced Raman spectroscopy (SERS) of serum for the detection of melanoma

Optical spectroscopy measuring the Raman effect and the surface-enhanced Raman effect is a topic of considerable interest. The Raman effect describes the exchange of energy during inelastic scattering between light and the vibrational and rotational modes of molecules. This was discovered by Sir C. V. Raman in 1928. Raman spectroscopy has already been shown to be effective in measuring trace amounts of chemical compounds and can detect the presence of sugar in blood [10] and has been proposed for the detection of blood alcohol levels [11].

Melanin has also been detected using Raman spectroscopy in skin or other high concentration areas such as moles or hair [12]. The ability to detect trace amounts in the blood stream or in other body fluids as a means of detecting malignant melanoma would be very desirable as malignant melanoma accounts for around 8000 deaths in the United States every year [13]. Raman scattering is usually a very small effect and can be quite difficult to detect if there are other effects present such as fluorescence, therefore we have sought to increase our Raman scattering by using the SERS technique.

Surface-enhanced Raman spectroscopy is a method that greatly increases the potential for Raman scattering through the use of carefully prepared substrates which create a localized surface plasmon resonance (LSPR). LSPR occurs when light interacts with very

strong localized electric fields that result when a nano-rough surface made from one of the coinage metals is irradiated with light. Increases in signal strength of up to 14 orders of magnitude have been reported enabling Raman spectroscopy of single molecules [14]. These substrates can preferentially bond to analytes that have a particular charge through electrostatic attraction.

In vivo SERS has already been successful at tumor targeting by using nanoparticle tags [15]. The work presented here shows that there is a difference in the SERS spectra of blood serum between healthy horses and horses with malignant melanoma. This first step will hopefully ignite interest in pursuing this path to early detection.

Cancer detection and treatment methods using optical and electrical techniques

Absorbance and fluorescence measurements of serum

Nearly one fourth of all deaths in the United States are caused by cancer [16]. In 2004, over 500,000 Americans died from cancer. Early detection and treatment improves the odds of patient survival. Therefore, appropriate screening techniques are emphasized, such as regular mammograms for breast cancer. Given the carcinogenic risks of ionizing radiation, ultrasonic and optical techniques are desired as safer alternatives. Endoscopy can highlight tumors in the cervix, lungs [17], and colon based on tissue autofluorescence and structure. However, these invasive tests are only suitable for cancer screening in high risk populations. Encouraged by the success of several protein expression assays to detect specific carcinomas of the bladder and prostrate [18-20], oncologists have searched for a universal cancer marker. However, until a tumor attains a certain size (>1 cm) or its location is clinically detected, there are very few general indicators of occult cancer. The many forms of cancer make it impossible to

effectively detect or treat with any one method. Advanced new technologies have been developed, such as hybrid forms of mass spectroscopy [20-22] and arrays of fluorescent probes conjugated with antibodies or DNA sequences [23], which can be used by researchers searching for patterns in protein expression in the hope of identifying malignancies.

There are good reasons to focus on blood composition for early detection of cancer. Healthy human serum consists mainly of albumin (4.0±0.25 g/dL) and various globulins (~2.2 g/dL) in water [24]. Many forms of cancer disturb local vascular structure and trigger significant immune responses. Therefore, serum levels of globulins, albumin, and hemoglobin metabolites may be modified by the presence of various neoplasia.

Several studies have noted a downward shift from the normal human serum albumin:globulin ratio (1.33) as cancers progress [25-27]. During acute inflammation, α-globulins are released in response to cytokines, like the tumor necrosis factor. Elevated β-globulin levels and monoclonal γ-globulin levels are often observed with multiple myeloma and lymphoma. An increase in C-reactive protein (a β-globulin) may occur as the body regulates inflammation in response to cancer. Chronic cancer conditions may also increase the levels of γ-globulins IgG, IgA, and IgM [28]. Using UV fluorescence spectroscopy, Hubmann found higher serum levels of α_2-globulins at the expense of albumin in patients with malignancies [29].

The relationship between serum albumin and cancer is less clear. Albumin synthesis in the liver increases about 40% in cancer patients who experience a wasting of body mass, but cancer is often associated with low serum albumin levels. Changes in major protein levels (like albumin and globulins) due to cancer seem to be more consistent with a whole-body response, rather than with local over expression of specific proteins by tumor cells [30].

If tumors induce hemorrhaging inside the body or weaken red blood cell walls, then hemoglobin would be released into the serum, either within the body or after blood is drawn from the patient. Under normal circumstances, hemoglobin quickly binds to blood proteins and is usually not observed at meaningful concentrations in serum or plasma [31]. Instead, the concentrations of haptoglobin-hemoglobin complexes and some β-globulins increase when red blood cells lysis; and if hemolysis is severe, haptoglobin concentrations can become depleted [28]. Therefore, to monitor total hemoglobin concentrations in serum, it would be useful to find a method that accounts for hemoglobin complexes as well. Furthermore, if high pH within tumors alters serum pH, then the spectra of hemoglobin complexes (such as methemoglobin) may be modified [31]. Porphyrin can accumulate in tissue and serum if tumors alter iron metabolism [32-34]. The well-known, strong autofluorescence of porphyrin has facilitated the visual detection of colon cancer and other malignancies under UV light [35-37].

These biochemical interactions justify primary serum protein monitoring as a trial basis for cancer screening. However, traditional colorimetric techniques of measuring albumin, globulins, and hemoglobin in serum have limited accuracy, because the results can vary significantly depending on whether these proteins are initially in an isolated state or in the form of a protein complex [38, 39]. Different medical research laboratories using blood chemistry panels quote different normal physiological ranges for serum proteins and give disclaimers about comparing results obtained from different labs making something more than blood chemistry panels necessary to detect recurring cancer [40]. With advances in computers and spectrometers, there has been a recent renaissance in absorbance and fluorescence spectroscopy methods of quantifying albumin and total protein concentrations in

serum, with improved sensitivity and linearity [38]. These developments facilitate affordable cancer screening.

Dogs are considered to be a good model of some types of human cancer and its response to therapy. Canine mammary cancer has many parallels to human mammary carcinoma presentation [41]. Furthermore serum globulins and albumin levels in dogs are comparable with the levels in humans. Therefore, canine populations were chosen to test the feasibility of using ultra-violet serum spectroscopy for cancer screening. This spectroscopic method of estimating the concentration of albumin, globulins and hemoglobin compounds in canine serum, enables sensitive monitoring of a patient's physiological response to illness and therapy and which may help to determine the presence of cancer in suspect patients. This cost-effective detection of analytes in blood sera makes this method very promising as a method of detecting and monitoring cancer in humans [3].

Dielectric function measurements of DNA melting point

After the determination of the structure of deoxyribonucleic acid (DNA) structure in the early 1950s, the number of studies of DNA has greatly increased due to its physical, chemical and physicochemical importance [42-44]. DNA is a highly complex and variable polymer. It can be extracted from cultured organisms, including bacteria, yeast, plant cells or mammalian cells by physical breakdown and precipitation with isopropanol in the presence of a high salt concentration. It is reported that chemically, DNA is nontoxic, stable and water soluble [45]. Observations of the physical structure of DNA show that it can be flexible or rigid. DNA flexibility is thought to depend on sequence composition. Rigidity profiles for short DNA sequences based on dinucleotide torsional constants for the 136

unique tetranucleotides have recently been obtained and used to develop a four-base steps code useful for predicting DNA sequence rigidity [46].

There are several applications for DNA in nanotechnology and biotechnology fields due to its unique properties. For example, DNA molecules adsorb onto many surfaces (e.g., nylon sheet, nitrocellulose paper, polylysine coated polystyrene plates, mica, glass, etc.) by electrostatic interactions between negative charges of the DNA and positive charges of the substrates to make different nano/biomaterials [47-51].

DNA typically exists as a double helix in biological systems [45]. In this form, DNA in a cell's genome can replicate itself which allows for cell division. By unzipping or melting the double helix into two single strands, DNA replication can be stopped thus controlling cell division which could have implications for the treatment of cancer. DNA melting can be accomplished via an increase in temperature, increase in salt concentration, a chemical reaction or other methods. There are three common theoretical models used for calculating a melting temperature-- A basic model, a salt corrected model and a nearest-neighbor model. The last two models have a number of different variations. These theoretical models can produce good results for relatively short DNA sequences. Experimental methods are needed for determining the melting point for longer sequences.

A method for determining the melting point of DNA based upon the change of the capacitance of DNA in a buffer solution has been developed. This cost-effective method of determining the melting point of DNA will be useful to scientists and medical researchers needing to know the melting entropy and enthalpy of long strands of DNA as a response to imposed conditions [4].

Chapter 2 ANALYSIS OF ISAM FILMS WITH APPLICATIONS

Introduction

The characterization and behavior of nanoscale thin-films is an ongoing pursuit. Many of the techniques useful in the characterization of macro-materials won't work or need to be adjusted when working with nanoscale materials. For example, capacitance measurements of ISAM films were unavailable prior to the work presented here. The widespread use or study of thin films with applications for everything from anti-reflection coatings on optics to nanoscale circuits makes it important to know how the films respond to changing environmental conditions as well as what the electrical and optical properties of the thin films are.

Presented here is the aging of ISAM films through repeated temperature cycles to test film response to temperature changes. Experiments for measuring the resistivity and capacitance of ISAM films have also been developed [1, 2]. Several different types of ISAM films have been used in this work: Nile Blue A-gold thin films were used in the thermal cycling experiments and for testing resistivity measurement techniques on a nanoscale. Poly(diallyldimethylammonium chloride) (PDDA)-Poly s-119 (PS-119) and PDDA-heparin ISAM films and spin-coated poly(methyl methacrylate) (PMMA) thin films were used in the development of a technique for measuring the capacitance of nanoscale thin films.

Thermal cycling and optical characterization techniques of ISAM films

Little research has been done on the effects of temperature changes on the physical, optical and electrical properties of ISAM films. ISAM, Spin-coated and other nanoscale films

are often made from dissimilar materials where changes in temperature might cause a breakdown in the film due to different thermal expansion rates or other factors. Many examples of fabrication and characteristics of nanoscale films constructed using dissimilar materials exist: The properties of organic dye molecules have been investigated by examining experimentally spin-coated dyes on metal films [52]. ISAM films, consisting of alternating layers of metallic colloidal nanoparticles coated in combination with a polyelectrolyte and polymer dyes, have been shown to exhibit conductivities similar to bulk metal [8]. Further studies indicated that such ISAM films show an enhancement of optical absorption at specific wavelengths due to a strong resonance interaction between the metallic nanoparticles and the dye molecules [7]. Electro-deposition techniques have been used to construct oligothiophene-linked metallic nanoparticles using organic bridging molecules [53, 54] Additionally, polystyrene spheres have been used as a template for metallic nanoparticle adsorption, making it possible to tune the optical properties of a film by controlling particle sizes and densities [55]. Ionic self-assembly (ISA) has been used to attach fullerenes to the metallic nanoparticles which allowed for further tuning of the optical properties [56].

It is important to evaluate the survivability of these ultrathin films in changing environments to determine any limitations that might hamper their widespread use. To address this issue, we have conducted thermal cycling of ISAM films. Fabricated samples were exposed to temperature fluctuations which were thought to potentially either cause thermal breakdown or mechanical failure due to different thermal expansion rates of the individual monolayers, or the multilayer stack and the substrate.

In our experiments, ISA has been used to form alternating layers of Nile Blue A and Au on glass substrates. Nile Blue A, an organic dye whose peak absorbance wavelength is slightly higher than 632 nm, was chosen for one of the monolayers. The other alternating

monolayer was fabricated using gold colloidal nanoparticles. The use of gold nanoparticles as the other monolayer with a different thermal conductivity, expansion rate and response to temperature changes was thought to provide a good material to test thermal cycling. The gold nanoparticles also decreased the resistivity of the film [8]. The resulting film had a high optical absorption to thickness ratio. The ISA process produced a high film uniformity that ensured homogeneous absorbance spectra across the surface of the film [5]. The process can be easily adapted to form bilayers on any surface geometry at room temperature and at atmospheric pressure. We present the results of temperature degradation studies that were carried out to determine the survivability of the films over many thermal cycles from -20° C to 120° C in ambient atmospheric conditions.

Experimental procedure

All materials were purchased from Sigma-Aldrich (St. Louis, Missouri.) A concentration of 5 mM of Nile Blue A in deionized water was used throughout the experiment. A suspension of gold colloids was made by adding 1 mL of 24.3 mM $HAuCl_4$ in deionized water drop-wise into 106 mL of rapidly boiling 2.2 mM sodium citrate solution in deionized water.

Glass substrates were prepared by bathing them in 7:3 mixture of 30% solution of sulfuric acid and a 30% solution of hydrogen peroxide for 30 minutes. The solution cleans the surface of the substrate. Nitrogen gas was then used to dry the surface of the substrate. The films were constructed using a StratoSequence V dipping machine. The substrate, which is negatively charged in aqueous solution, is dipped into a solution of positively charged Nile Blue A molecules for five minutes. During this time, the Nile Blue A molecules were adsorbed to the surface of the substrate leaving a net positive charge on the surface. The dipping machine then rinsed the sample with deionized water to remove loosely bound

molecules and then dipped the substrate into a solution of negatively charged Au nanoparticles (gold colloids) for another five minutes. Further rinsing with deionized water was performed to remove any loosely adsorbed Au nanoparticles. The result of this process was one bilayer of Nile Blue A – Au with a negatively charged surface. During the building process, a Hitachi U-2001 UV-Vis spectrophotometer was used to measure the absorbance from 400 to 1000 nm every five bilayers up to 40 bilayers.

Thermal cycling was performed in a programmable ESPEC Temperature and Humidity Chamber SH-240 with temperatures ranging from -20° C to 120° C conducted on samples of 10, 20, and 30 bilayers to assess the survivability of the thin films in changing environments. The samples were held at each of the temperature extremes for one hour per cycle in ambient atmospheric conditions as shown in Figure 2-1. The absorbance was measured at the end of every five thermal cycles to determine if thermal cycling had any effects on the optical quality of the film.

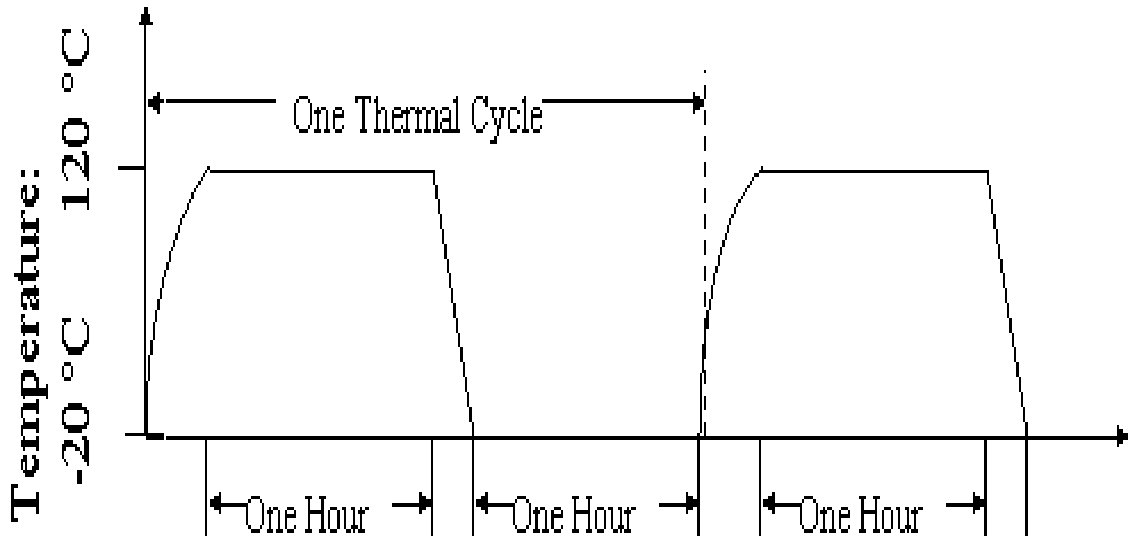

Figure 2-1 Thermal cycling process used to test the Nile Blue A – Au film

Resistivity measurements were conducted on samples of 50 and 100 bilayers. Four aluminum contact pads were deposited on to the sample using an Edwards FL 400 Thermal Evaporator. Sample current was driven by an Agilent E3630A DC power supply and the current through and the voltage across the sample were recorded using two Agilent 34401A 6 ½ Digit Multimeters as can be seen in the schematic shown in Figure 2-2. Atomic force microscopy (AFM) was performed to obtain a topographical image of the sample using a Dimension 3100 Atomic Force Microscope by Digital Instruments to determine film thickness by measuring the height difference between the surface of the film and the substrate at the film edge. The length and width of the film were measured with a caliper. Using the instruments mentioned above, a four point probe measuring system was used to measure sample resistivity. The sample was measured both current directions. Voltage was plotted against current for both cases with the slope of the plots equal to the resistance. The formula $R_{actual} = (R_{forward} + R_{reverse})/2$ was used to account for any offset voltages that might occur. R_{actual} and the dimensions measured with the AFM and the caliper were used to calculate the resistivity using the formula $\rho = (\text{width} \bullet \text{thickness} \bullet R_{actual} / \text{length})$ to obtain the resistivity. A Woollam Variable Angle Spectroscopic Ellipsometer was used to determine the index of refraction and the extinction coefficient of the film using the thickness obtained by the AFM and the modeling software provided by Woollam with the ellipsometer.

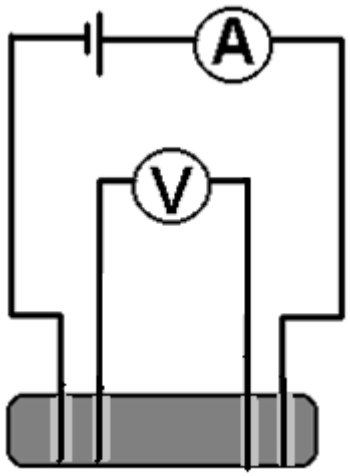

Figure 2-2 Schematic of resistivity measurement setup with wires connected to aluminum contact pads using silver epoxy

Results and Discussion

The ISA process using Nile Blue A – Au produces a relatively high absorbance versus thickness when compared to a dye alone. The absorbance spectrum indicates that the maximum absorption is around 700 nm as seen in Figure 2-3. The bilayers provide the individual dye molecules with direct contact to Au nanoparticles giving a greatly increased absorbance due to surface-enhancement phenomena [7]. The absorption enhancement is due to surface Plasmon resonance.

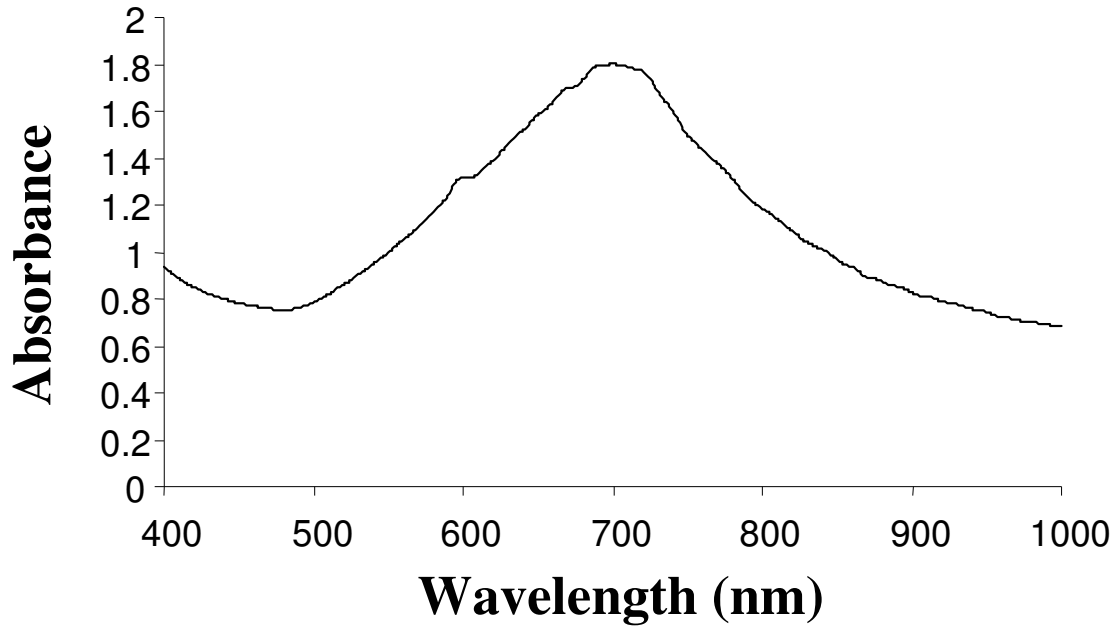

Figure 2-3 Absorbance of unheated Nile Blue A – Au 30 bilayer sample

A charge transfer mechanism may also exist where electronic excitation may be transferred between the dye molecule and the metallic nanocluster. As more bilayers are built, a slight redshift in maximum absorbance is observed in our data indicating a greater surface Plasmon resonance [52]. This results in a redshift because the plasma frequency of the Au nanoparticles has a corresponding wavelength which is greater than the absorbance maximum of the Nile Blue A molecules. A redshift of the absorbance peak occurs as a function of film thickness and shifts the maximum absorbance from about 680 nm for 5 bilayers to about 710 nm for 40 bilayers. Figure 2-4 shows that the growth in absorbance for the first ten bilayers is less than the absorbance growth rate after ten bilayers have been deposited suggesting that the coverage of the bilayers on the substrate were not complete until after ten bilayers had been formed creating a larger surface charge density. The growth in maximum absorbance is linear after the first ten bilayers are formed indicating that the

ISA process does not breakdown for up to 40 bilayers. The absorbance for larger numbers of bilayers was greater than could be determined by the spectrophotometer.

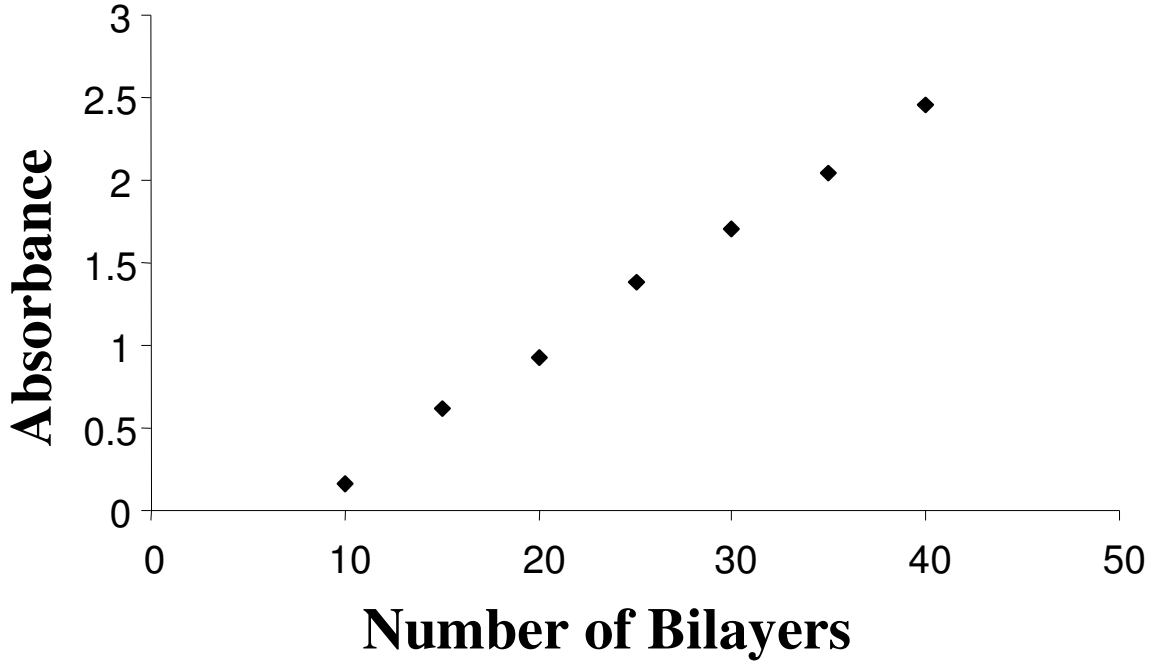

Figure 2-4 Maximum absorbance of Nile Blue A – Au film

Thermally cycled samples of 10, 20, and 30 bilayers displayed negligible degradation from temperatures up to 120° C. Figure 2-5 shows that the three samples maintain constant UV-Vis absorption characteristics. The absorbance of the samples was measured at the end of every five thermal cycles. It is interesting to note that the thickness of the films had no effect on film degradation throughout the cycling process. Atomic force microscopy in tapping mode found the film thickness to be about 2.4 nm per bilayer for fifty and hundred bilayer films. Resistivity was calculated to be about 10.4 Ohm•cm for a fifty bilayer film and 9.3 Ohm•cm for a hundred bilayer film. The film is Ohmic as can be seen by the linear increase in voltage as the current is increased as shown in Figure 2-6.

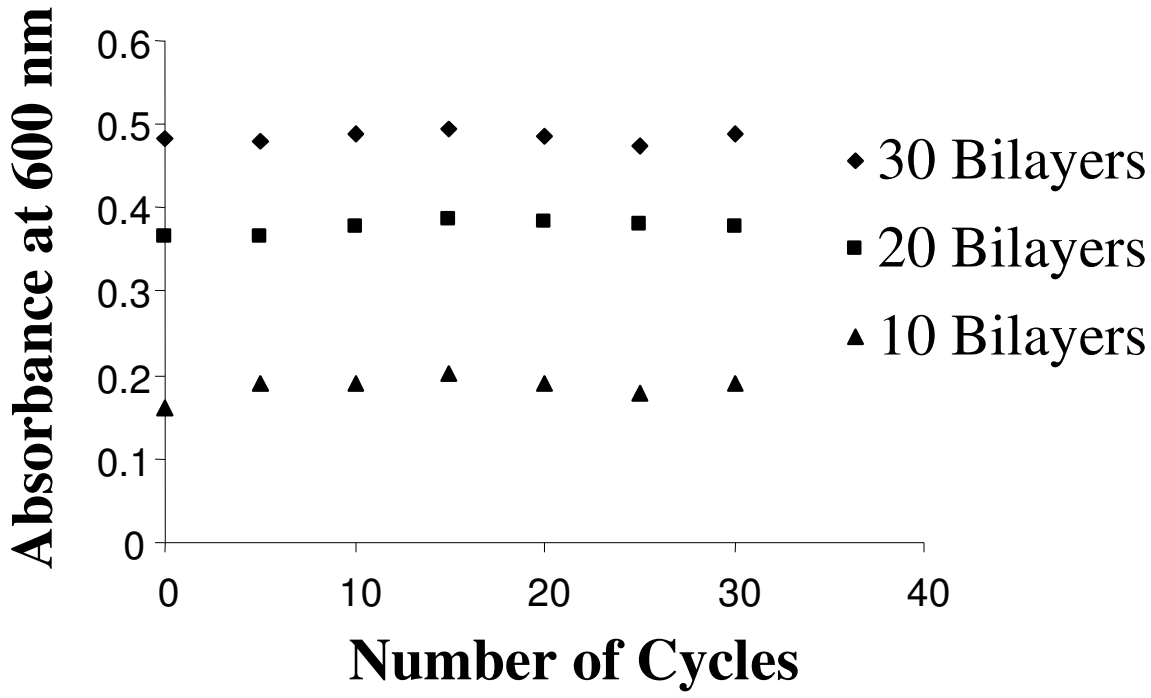

Figure 2-5 Thermal Cycling Effects on Nile Blue A – Au film (-20° to 120° C)

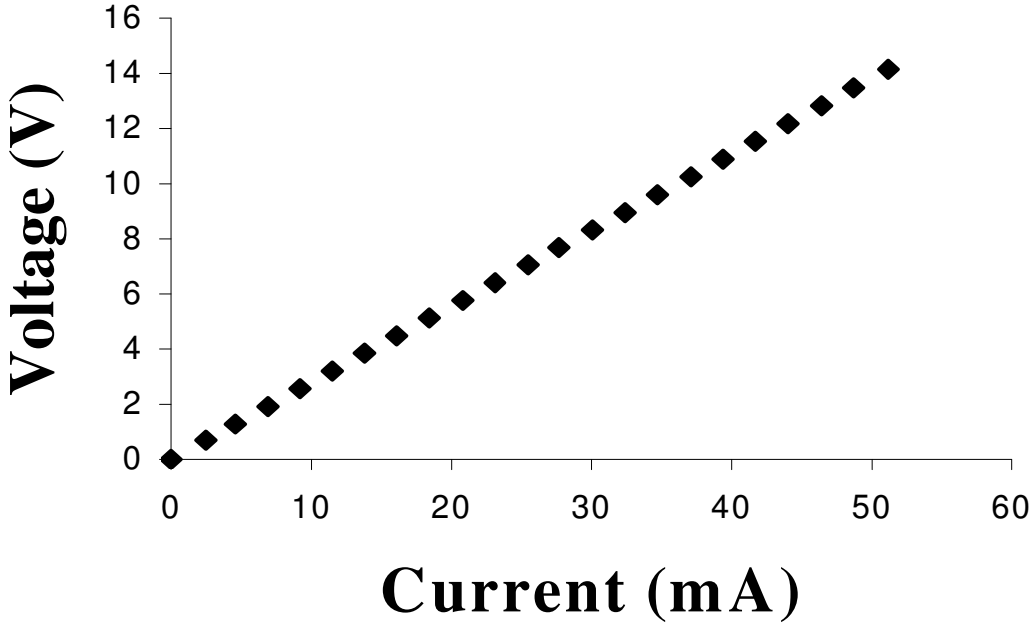

Figure 2-6 Voltage versus Current for 50 Bilayers of Nile Blue A – Au film

The index of refraction and the extinction coefficient for the thin film exhibit ultrathin metal-like behavior [57]. We can see from Figure 2-7 that a ten bilayer film has a high index of refraction in the optical range that decreases to about that of glass in the near infrared range. We converted the extinction coefficient k shown in Figure 2-7 to absorbance and plotted it versus wavelength as shown in Figure 2-8. A blueshift is seen in Figure 2-8 when compared to Figure 2-3, which can be attributed to the fact that the data shown in Figure 2-8 comes from a ten bilayer film while the data shown in Figure 2-3 comes from a thirty bilayer film and therefore has a greater surface Plasmon effect.

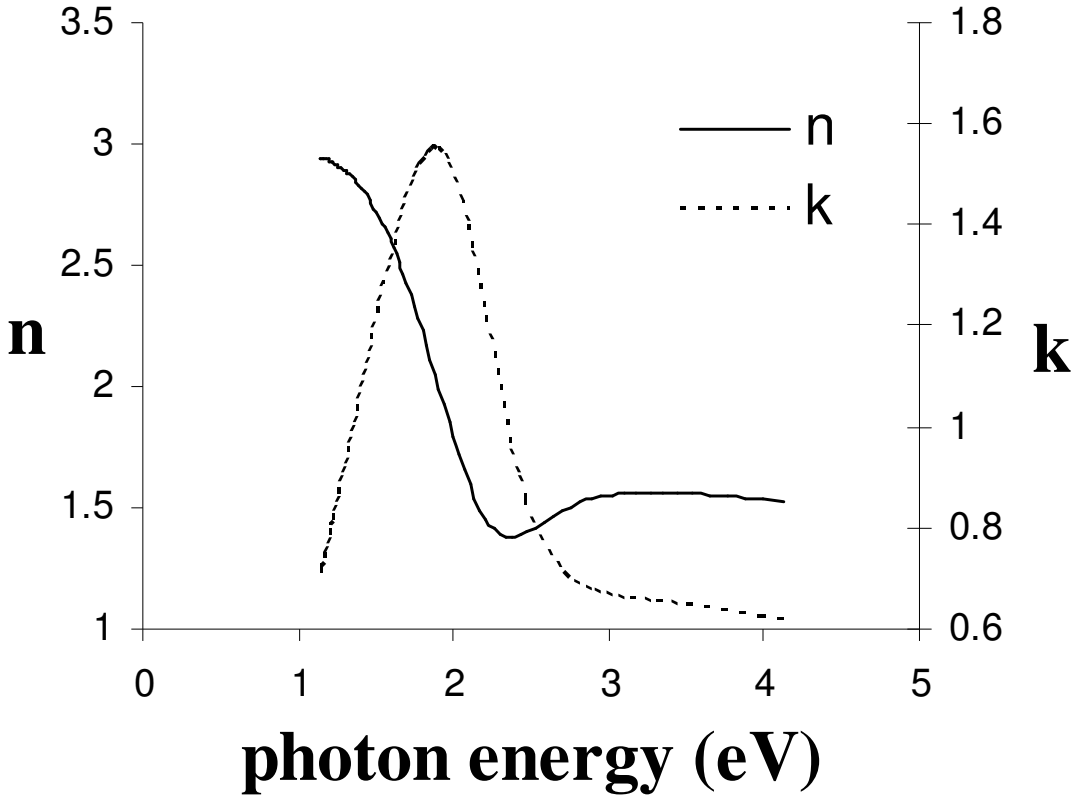

Figure 2-7 Index of refraction and the extinction coefficient of Nile Blue A – Au film

The Nile Blue A – Au ISAM thin films have shown linear growth in absorbance as a function of bilayer number. Therefore, using this method, it is relatively easy to build a film with the desired absorbance. When building the films, it was found necessary to always use a freshly made gold colloid solution. The gold colloid suspension was found to be very unstable as nanoparticles sometimes aggregated and fell out of solution.

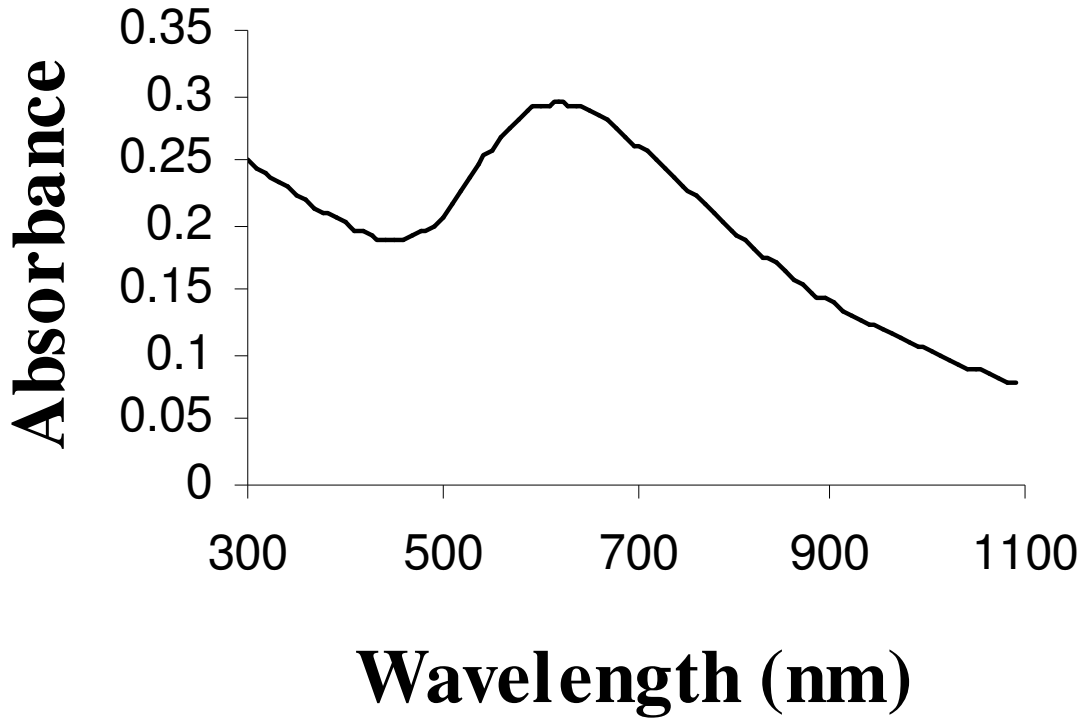

Figure 2-8 Absorbance versus wavelength calculated from the extinction coefficient

A method for measuring the capacitance of ISAM films

Capacitance, dielectric function and dissipation factor are important parameters for material selection and applications. The dielectric function is found by determining the ratio of the measured capacitance of a film between two electrode plates to the capacitance of the same plates separated by an equal thickness of air [58, 59]. Dissipation factor is the

inefficiency of an insulating material, and is defined as the ratio between the insulating material's impedance at a specific frequency and its capacitive reactance. It indicates the loss of energy from an applied field because of the internal and external defects and traps in the materials. These parameters can be modified by varying the temperature, frequency, humidity and structural defects [58-60].

Electrical breakdown field (or dielectric strength) is an important property of materials used in a high electric field, and is defined as the field value at which a material becomes conducting. Although there is no simple mechanism expressible analytically, the mechanisms of breakdown or dielectric failures possibly come from a combination of thermal, avalanche, local discharge and/or electrolytic effects. Breakdown failures depend on many parameters, including the fabrication conditions of materials, thickness, applied field, presence of additives (or impurities), degree of cure, temperature, internal and external defects (free volume, film rupture, etc), environment (especially humidity) and time. It is known that the breakdown fields of many polymeric materials (ranging mostly between 8 and 50 MV/m at room temperature) usually decrease with increasing temperature and frequency [58, 59].

ISAM films can experience environmental influences in service, and their properties can degrade at different rates depending on the temperature, humidity, voltage and frequency. Such degradation processes increase the external and/or internal stresses between coating materials and substrates. As a result, the physical, chemical and physicochemical properties of the films change, possibly resulting in film failure [5]. Characterization of polymeric ISAM films is important for many industrial applications. Here the dielectric functions and breakdown fields of ISAM films are measured using a new technique as a function of applied field, temperature and frequency at lower relative humidity.

Theoretical background

Dielectric materials can be either polar, where the molecular dipoles can rotate and align with the application of a field, or non-polar, where no rotation or alignment can be obtained. As the frequency and temperature increase in materials, the alignment is blocked by molecular collisions and drag, resulting in a loss of energy and a drop in the capacitance and dielectric function values. Therefore, effects of frequency and temperature upon dielectric function must be considered when selecting dielectric materials for specific applications [58-60].

Physical (mechanical, thermal, optical, magnetic and electrical), chemical (MW, glass transition temperature *(T_g)*, color, density, surface energy and hydrophobicity) and physicochemical (swelling and corrosion) properties of the ISAM coatings can be determined by using various methods [5]. For instance, the dielectric function of a material that is considered for a capacitor design is usually calculated from the capacitance *C* measurement value using a parallel plate geometry [58-60]:

$$C = \varepsilon \frac{A}{l}$$

Where *A* represents the area of plates, *l* is the distance between the plates (or film thickness) and ε is the permittivity of the dielectric medium between the plates, which is greater than the permittivity of the vacuum ε_0 (8.85 × 10-12 pF/m). As is seen, capacitance values increase with increasing the area and decreasing the distance between the parallel plates. When considering a parallel plate capacitor with circular plates separated by a distance *l*, and having an effective radius *r*, the effective radius due to the fringing fields is given by the following equation:

$$r = r_1 + \frac{w}{2} - \frac{2l}{\pi}\ln\left[\cosh\frac{\pi w}{4l}\right]$$

Where r_1 is the radius of a guarded electrode and w is the radial separation between the guarded electrode and guard electrode *(w = r2-r1)*. This will help measure the effective area (A) of the plate, and reduce the errors for the capacitance values of the nanoscale films. Figure 2-9 shows a schematic illustration of the guarded electrode and guard electrode used in the capacitance measurements.

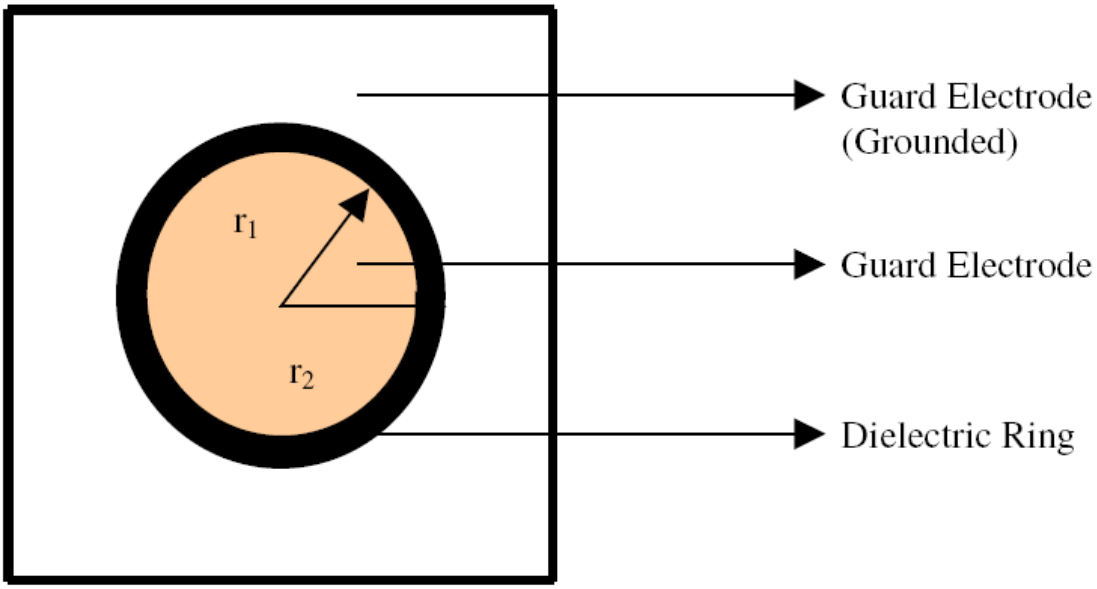

Figure 2-9 Schematic illustration of the guarded and guard electrodes

The relative permittivity (or dielectric function value) ε_r is equal to the ratio of both values:

$$\varepsilon_r = \frac{\varepsilon}{\varepsilon_0}$$

The relative permittivity is greater than 1 and symbolizes the increase in charge storing capacity. The dielectric function is used to determine the quality of an insulator, so it is one of the main parameters for characterizing and designing electronic components (e.g.,

capacitors). Table 2-1 gives dielectric and breakdown field values of selected materials at room temperature and 1000 Hz [5, 58-60].

Table 2-1 Dielectric function and breakdown field values of selected materials

Materials	Dielectric constant	Breakdown field (kV mm^{-1})
Air	1	2.8–3.0
Pure water	81	—
Ice	3.2	—
Expanded polystyrene	1.05	—
Polyamide 66	3.6–5.0	8
Nylon	3.5	14
Epoxy	3–5	16
Polyurethane	3.4	20
Polystyrene	2.56	20
Polyethylene	2.2	22
Polycarbonate	2.9	23
Polypropylene	2.3	28
PMMA	2.8	—
Teflon	2.1	60
Glass	3.8–14.5	200–400
Mica	4–8	200–700

Materials used for fabrication

For the present study, ISAM films were chosen to validate the new technique due to their uniformity, known thickness and ease of fabrication. In this technique, gold coated (~200 nm thickness) glass slides (2.5 cm × 2.5 cm) purchased from EMS, Inc. were used The gold surfaces were sonicated in acetone and ethanol before building the bilayers. ISAM films of PS-119–PDDA and heparin– PDDA were fabricated on the gold surface using a dipping

machine (nanoStrata, Inc., Tallahassee, FL) at different bilayers to obtain desired film thicknesses. The dipping machine is the most commonly used method for the fabrication of ISAM films on substrates[5]. Analytical grade poly(diallyldimethylammoniumchloride) (PDDA), poly dye Poly s-119 (PS-119) and heparin were purchased from Aldrich, Sigma and Celsus Laboratories, Inc. (Cincinnati, OH), respectively. Atomic force microscope (AFM) (Digital Instruments with tapping mode) image analysis confirmed that the surfaces were uniformly coated by the Au and ISAM films. Figure 2-10 illustrates AFM images of an Au-coated glass slide and 150 bilayers of the PS-119 and PDDA film covering such an Au-coated slides.

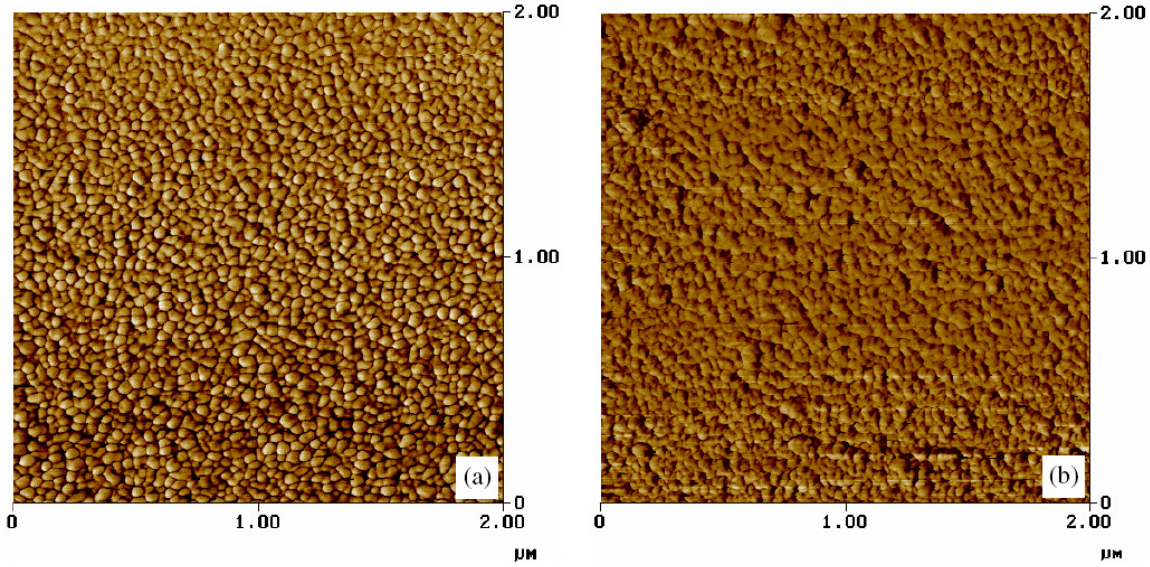

Figure 2-10 AFM phase images of (a) gold-coated glass slide and (b) 150 bilayers of PS-119 and PDDA film on the gold surface (2 μm × 2 μm).

A plastic ring with a known diameter was attached on the surface of the ISAM films using an epoxy (ITW Performance Polymers, # 47609/31345). 200 nm of Al coating was applied on the outside of the plastic ring using a physical vapor deposition technique (Edwards FL 400/AUTO 306 manufactured in Edwards High Vacuum—Part of BOC Ltd)

at 1×10^{-5} Torr vacuum and room temperature. Finally, a highly conductive silver grease (ITW Chemtronics, Inc.) layer was added inside the plastic ring, which was connected to the capacitance bridge through a brass electrode. In order to validate the technique, clean glass slides (2.5 cm×2.5 cm) were also coated by Al (200 nm) using the same deposition technique and then a 35 μm layer of poly(methyl methacrylate) (PMMA) (dissolved 20% in acetone)was spread by a spin coater (CEE— Brewer Science, Inc.) before a second Al coating (200 nm) was deposited.

Experimental Design

In the present study, the dielectric function and breakdown field of nanothickness ISAM films were measured using a commercially available AH 2700A Ultra-Precision 50 Hz– 20 kHz capacitance bridge (Andeen-Hagerling, Inc.). Figures 2-11(a) and (b) show the

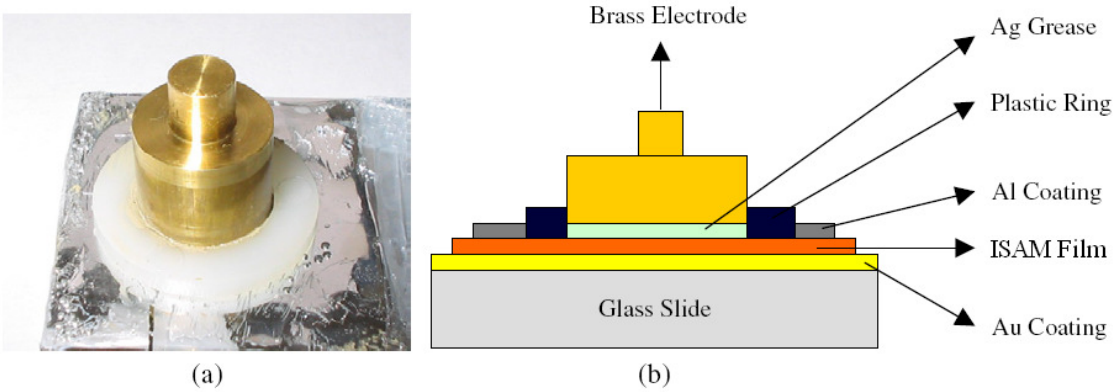

Figure 2-11 (a) Top view of the prepared sample and (b) its schematic illustration

samples proposed for capacitance and breakdown field measurements and a schematic of the measurement characterization. Silver grease and a brass electrode with a smooth surface were employed in these studies. The purpose of using the silver grease is to avoid any destruction on the ISAM films during measurements. The capacitance and breakdown field measurements were made in a temperature and humidity controlled chamber (Espec SH-240

manufactured by Hendrick Environmental Systems & Controls, Inc.). During the tests, temperature, frequency and voltage were varied over the ranges 0–50° C, 50–20 000 Hz and 0.001–15 V, respectively. In order to eliminate the external capacitance value of the Al top coating, it was grounded during all the tests.

Capacitance measurement and dielectric function calculation

Film thickness is critical for the development of advanced materials and devices. In order to find out the capacitance and dielectric function of films, a series of experimental tests was performed on nanoscale thickness ISAM films. Figure 2-12 shows the temperature-dependent capacitance values of PS-119 and PDDA films as a function of temperature between 0 and 50° C at 1000 Hz, 1 mV and 15% relative humidity. Our previous ellipsometry study showed that 75 bilayers, 150 bilayers and 225 bilayers gave 210, 410 and 630 nm thicknesses, correspondingly. As is seen, there are three distinct regions in the present Figure 2-12: (1) between 0 and 10° C no significant capacitance changes are distinguished for the three films; (2) the capacitance values start increasing in the temperature range between 10 and 40° C; and then (3) slowing down after 40° C. Although such phenomena in the regions of second and third stages are not clearly understood, they could be related to the charge blockage and release, surface charge polarization along with dipole screening, phase changes (solidifying temperature (T_s), melting temperature (T_m) and T_g), thermal expansion effects on the thickness of the films, and/or dipole pinning and depinning mechanisms during these temperature and frequency variations [58-60]. Future work could focus on the changes of capacitance values as a function of variations.

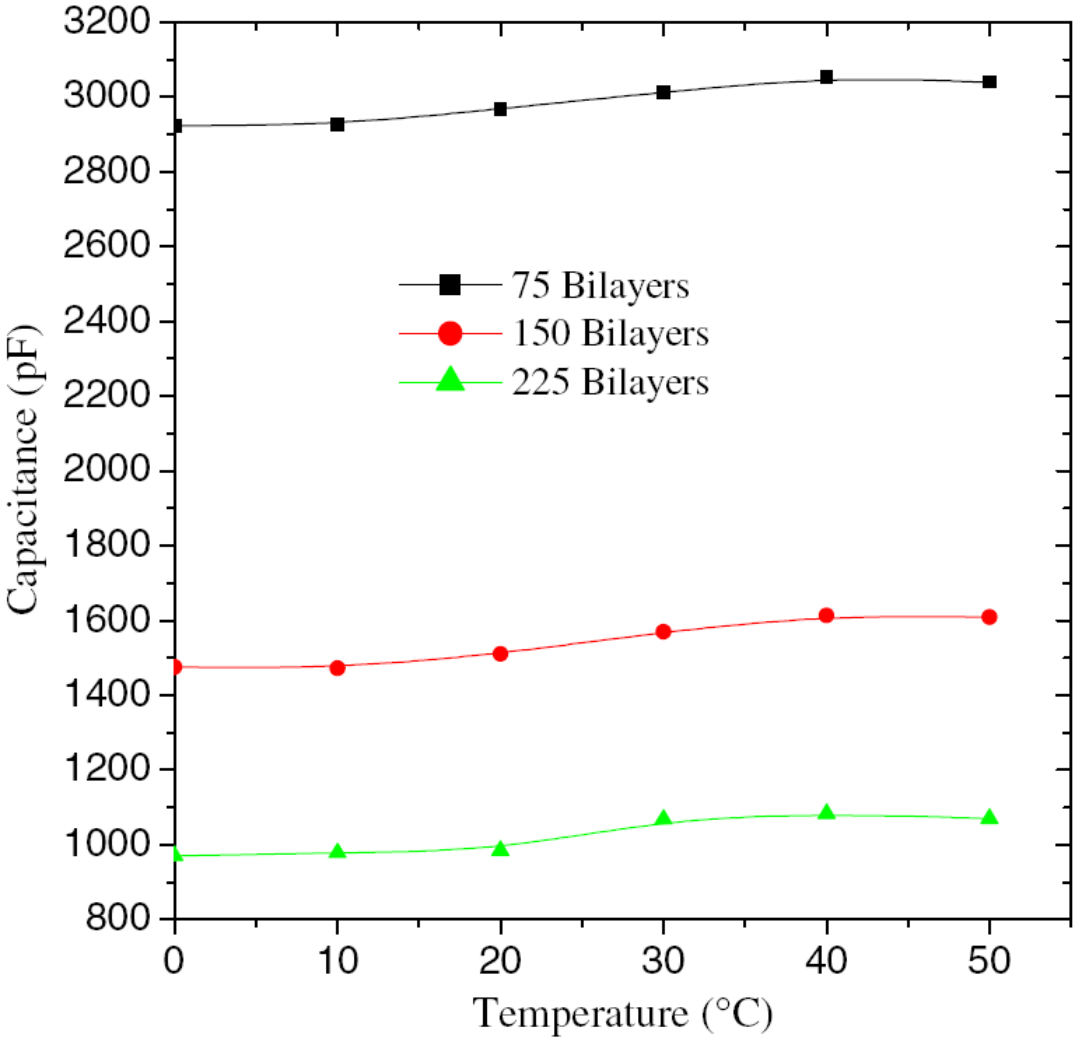

Figure 2-12 Capacitance measurements of ISAM films at 75 bilayers, 150 bilayers and 225 bilayers as a function of temperature: The tests were carried out at 1000 Hz, 1 mV and 15% relative humidity.

In the next step, dielectric function values were calculated from the capacitance measurement values using appropriate equations given above. The capacitance values were measured in the temperature range 0–50 .C and frequency range 50–20,000 Hz for each film. It was determined that beyond 50° C electrical arcs occurred, which may indicate a thermal failure at higher temperatures. In addition, when the relative humidity exceeded 80%, arcing

also occurred on some of the thinner films. Figure 2-13 displays the temperature- and frequency-dependent dielectric functions of (a) 75 bilayers, (b) 150 bilayers and (c) 225 bilayers of PS-119 and PDDA films. The applied voltage and relative humidity of the chamber were 1 mV and 15%, respectively.

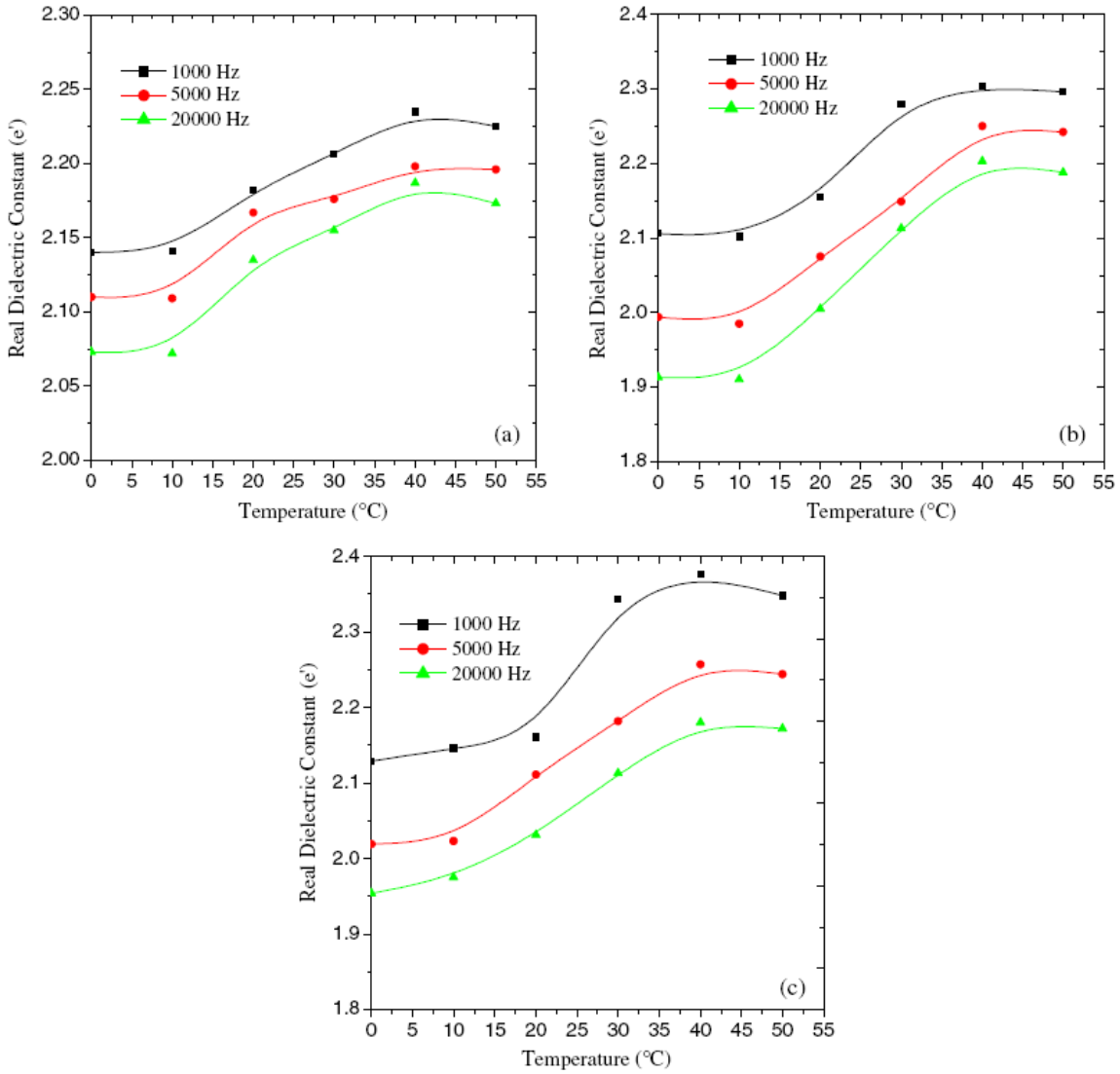

Figure 2-13 Real dielectric function measurements of (a) 75 bilayers, (b) 150 bilayers and (c) 225 bilayers of PS-119 and PDDS films as a function of temperature and frequency. The tests were conducted at 1 mV and 15% relative humidity.

It is seen that the frequency-dependent dielectric properties of the films are similar to those of most polymeric and ceramic capacitors [59, 61-66]. The dielectric function values at lower frequencies are larger than those at higher frequencies for all the film thicknesses. At higher frequencies, screening effects may be more dominant, while for the low frequencies dipole–dipole interactions seem enhanced at that particular temperature range. Figure 2-13 also confirms that the dielectric function values of ISAM films are temperature dependent. For instance, temperature ranges between 0 and 10° C give almost the same dielectric function values for all the thicknesses of the ISAM films; however, these values are considerably increased in the temperature ranges between 10 and 40° C, and then slightly decreased after 40° C. At all frequencies and temperatures, such variations can be seen for all the samples, which is an expected result based on the obtained capacitance values. It is reported that the capacitance and dielectric function variations may be attributed to the dipole–dipole interaction, thin-film thickness changes based on the thermal expansion/shrinkage and screening effects [58-61, 66].

It is known that temperature and humidity are important environmental parameters for many materials, and can cause permanent electrical property changes in their structures. To be able to determine such effects, one of the ISAM films (75 bilayers of PS-119 and PDDA) was exposed to five temperature cycles between 0 and 50° C at 3° C/ min and 15% relative humidity. Figure 2-14 illustrates the real dielectric function values of the ISAM film obtained at 1000 Hz and 1 mV. The capacitance and dielectric function values of ISAM films increased slightly after the temperature cycles. This may be because the fact that the thin-film condensation (or lower porosity), thermal shrinkage, charge release and surface charge polarization along with dipole screening mechanisms are more dominant after the

temperature cycles. Overall, these results indicate that effects of temperature cycling must be considered for polymeric ISAM thin films when constant temperature cannot be maintained.

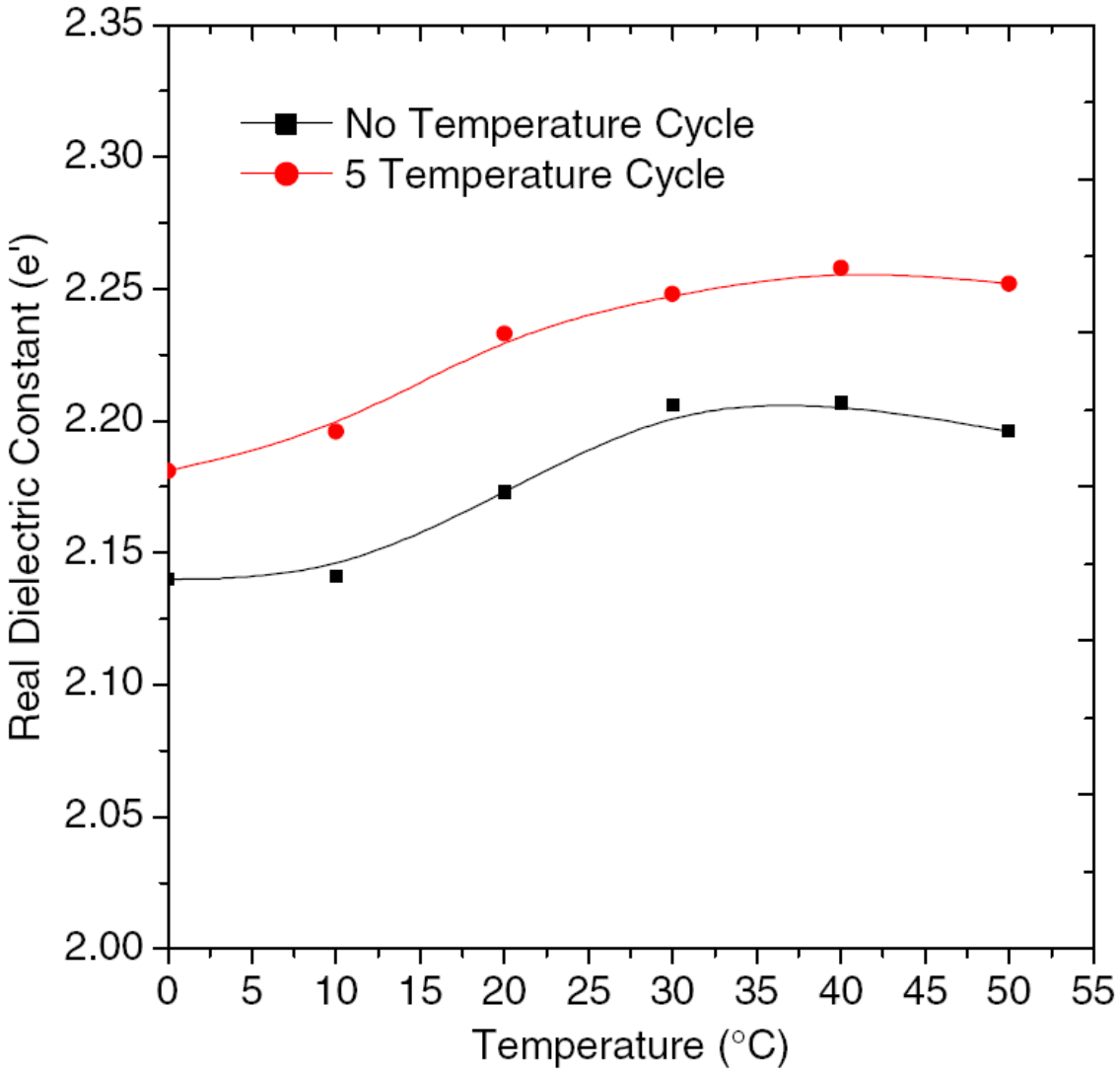

Figure 2-14 Real dielectric function measurements of 75 bilayer of ISAM film (PS-119 and PDDS) as a function of temperature at 1000Hz and 1 mV after five temperature cycles between 0 and 50 ◦C.

There are principally three possible ways of increasing the magnitude of the dielectric function and capacitance values: increasing the dipole strength (or the number of dipoles), thermal shrinkage and density of materials (or decreasing free volume in the material

structure) [58-60]. In the present study, we did not determine the changes of the dipole strength, thermal expansion coefficient values nor carry out film densification studies. However, we assumed that thickness of the ISAM film would be reduced after the temperature cycles. In other words, the porosity of the film decreased and the coating became more compacted during five temperature cycles between 0 and 50° C, which in turn increases the dielectric function values. Figure 2-15 shows a possible densification process of the ISAM films over a broad temperature range.

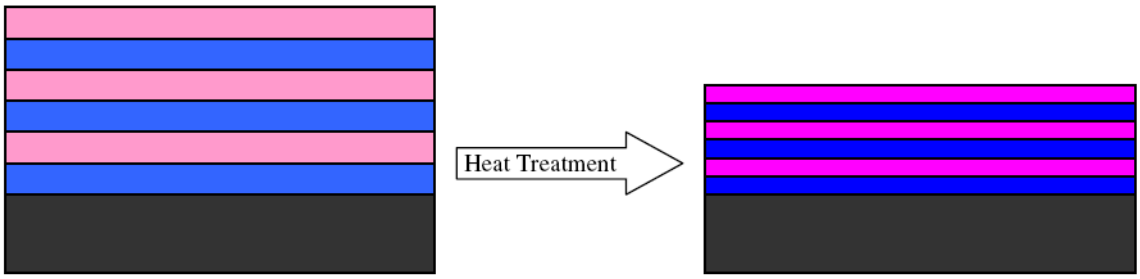

Figure 2-15 Densification process of the ISAM film over a broad temperature range

ISAM films with heparin

Heparin is a bio-oriented natural polymer, and is used for many medical applications. It is a heterogeneous group of straight-chain anionic mucopolysaccharides that have anticoagulant properties [67]. In the next test, a series of dielectric function measurements were carried out on 75 bilayers (120 nm) of heparin and PDDA film as a function of temperature and frequency at 15% relative humidity. As is seen in Figure 2-16, between 0 and 50° C the dielectric function maintains a nearly constant value.

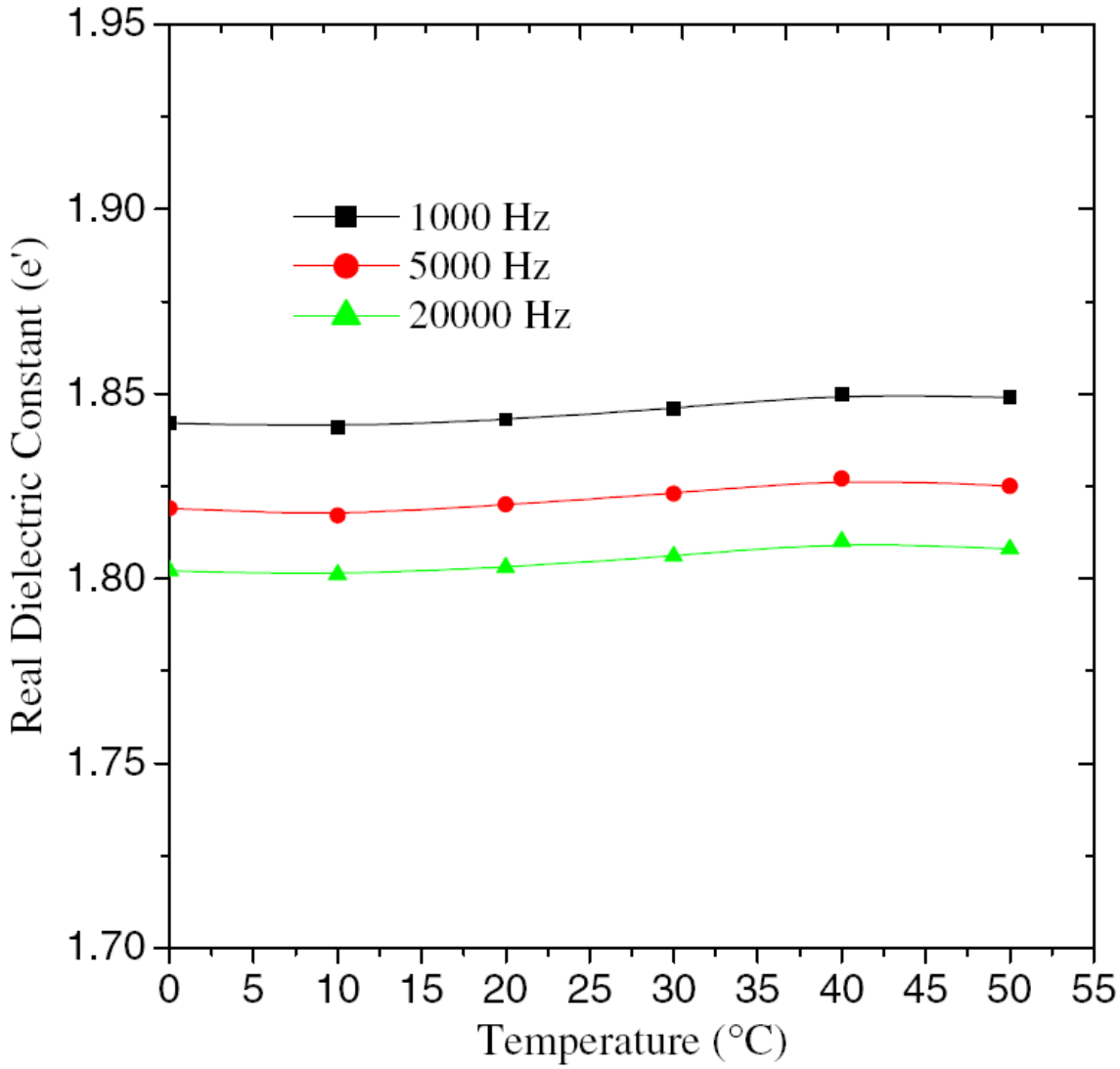

Figure 2-16 Dielectric function values of 75 bilayers of heparin and PDDA film as a function of temperature and frequency at 15% relative humidity

The same dielectric function measurement technique was performed on a relatively thick Poly(methyl methacrylate) (PMMA) film (35 μm) fabricated on Al coated glass slides (2.5 cm × 2.5 cm) using the same conditions. The electrical properties of PMMA are well known [58, 59]. The purpose of the present study is to confirm that the new technique can be appropriate for the property characterization of thin films. Figure 2-17 shows dielectric function measurements of PMMA film as a function of temperature and frequency at 1 mV

and 15% relative humidity. The test results showed that our dielectric function results matched values obtained using different dielectric measurement techniques [58-60].

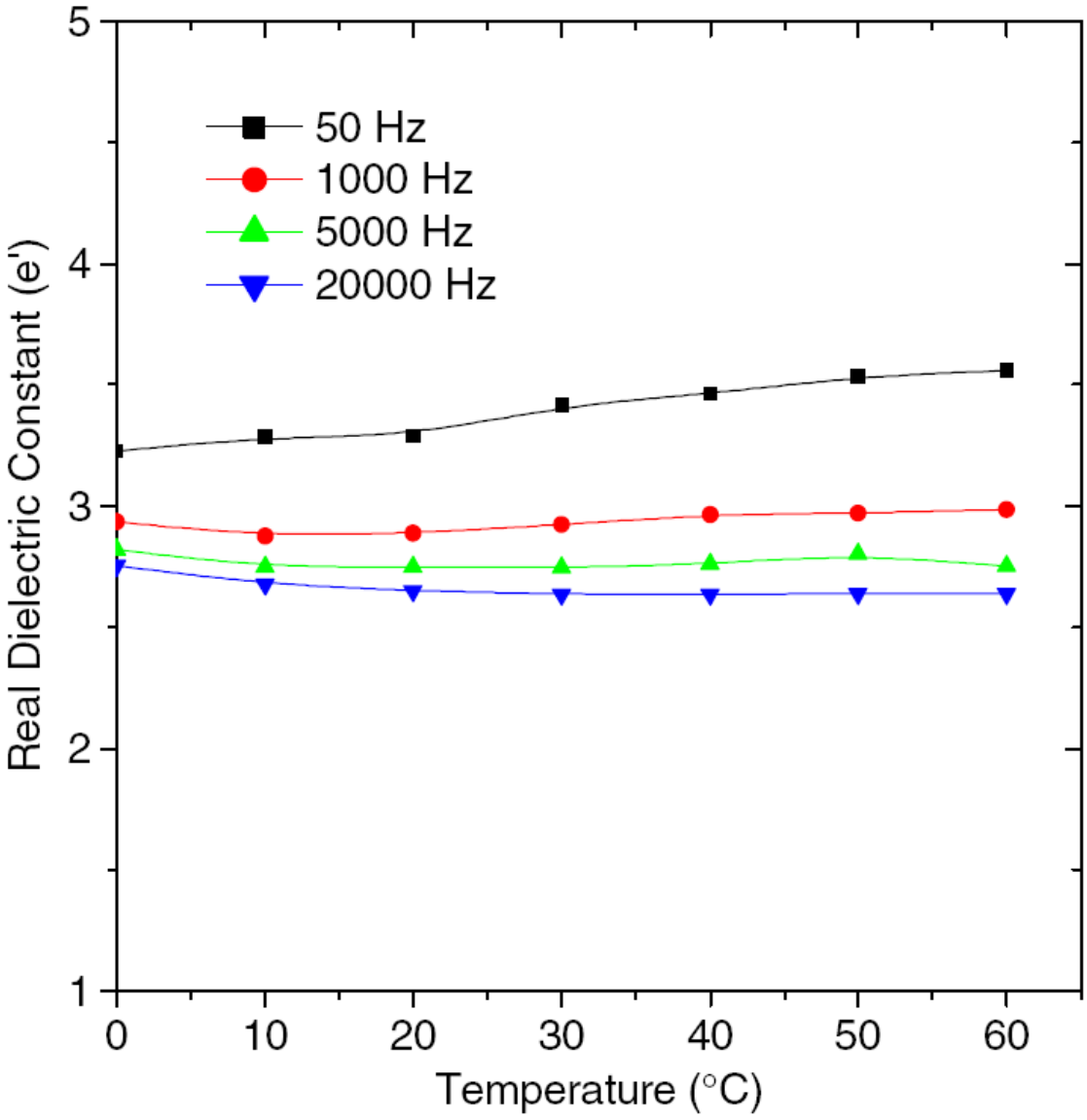

Figure 2-17 Real dielectric function measurements of PMMA film as a function of temperature and frequency at 15% relative humidity

Electric field breakdown determination

The electrical breakdown field is an important parameter for most electronic devices used under various temperature, humidity and frequency cycles. The breakdown field is usually

the result of a substantial increase in the concentration of mobile charge carriers (both ions and free electrons). It is assumed that such increase is due to the effect of an electric field and heat on the dielectric films. As is known, when the film degrades because of electrical fields, electric current arcs between electrodes resulting in the formation of a failure path by chemical decomposition and local erosion on the materials [58, 59, 68]. In the present studies, the relationship between the breakdown electric field (electric field corresponding to the current density) and thicknesses of PS-119 and PDDA films was investigated at 20° C and 40° C. Figure 2-18 shows the breakdown field (kV mm-1) of the ISAM films as a function of temperature and film thickness at 1000 Hz and 15% relative humidity.

As is seen in Figure 2-18, an applied electric field and temperature are the major causes of the breakdown in the ISAM films. In this study, the electric field breakdown seems to be related to the local overheating of the ISAM films in the vicinity of the defect areas of the material, resulting in electrical and thermal failure. In this breakdown, energy dissipation causes the temperature on the material to go above the critical temperature, which causes a failure point. In addition, we determined that external heat also lowered the breakdown field of the ISAM films. For example, when the temperature of the ISAM films increased from 20 to 40° C, the breakdown field decreased from approximately 9.8 to 9.0 kV/mm, which corresponds to a nearly 8% reduction in the breakdown field strength. Another interesting finding is that breakdown field lines were nearly independent of film thicknesses ranging from 50 bilayers (140 nm) to 225 bilayers (630 nm).

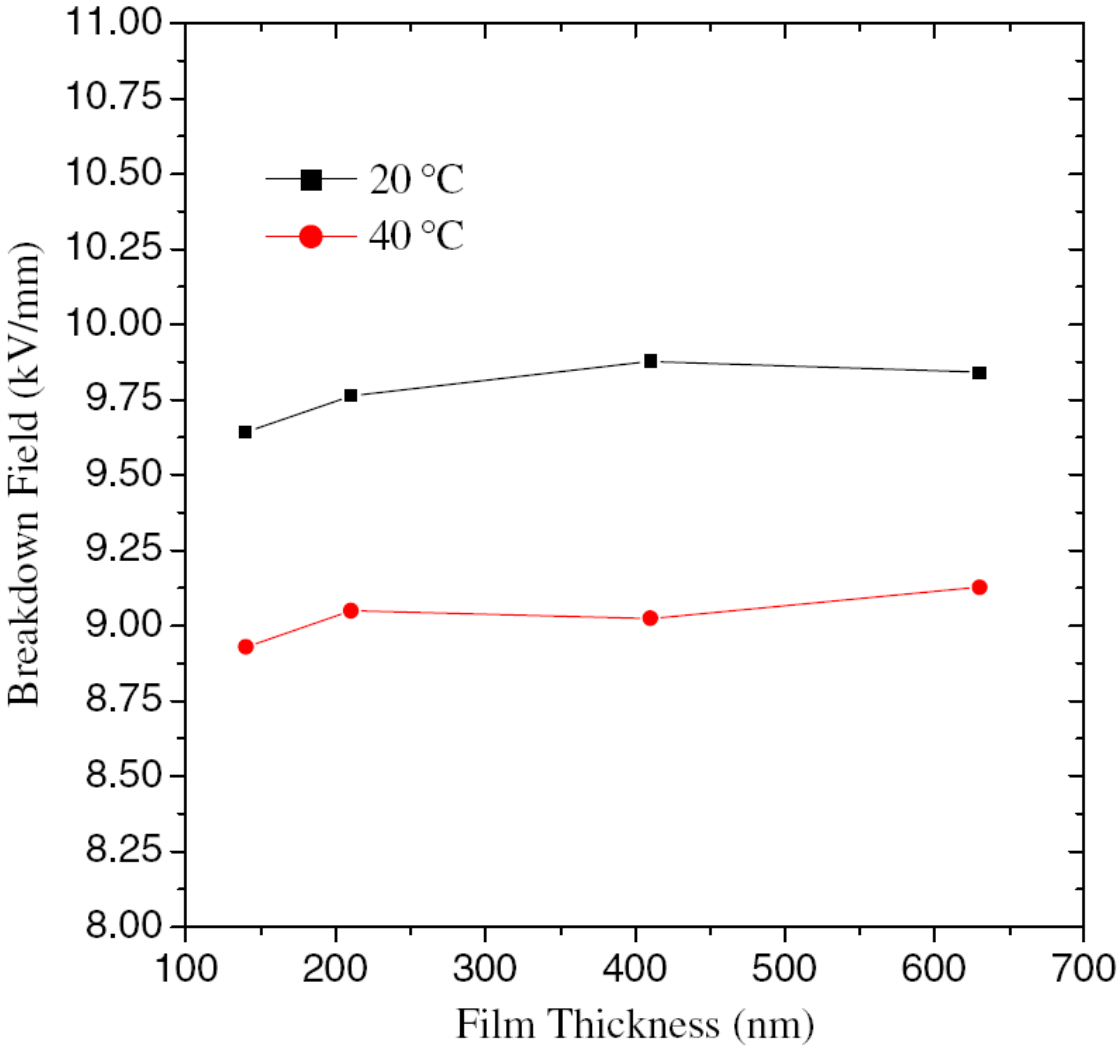

Figure 2-18 Breakdown field (kV mm−1) of ISAM films (PS-119 and PDDA) as a function of film thickness for two different temperatures and electric field at 1000 Hz and 15% relative humidity.

Summary

We determined the capacitance, dielectric function and breakdown field values of ISAM films at varying temperature, voltage and frequency ranges, and 15% relative humidity. We found that the capacitance, dielectric function and electric breakdown field values were very sensitive to temperature, frequency, applied voltage and humidity. The capacitance and

dielectric function values confirm such conclusions. Higher voltages, temperatures and humidity increase the breakdown of the dielectric material. Overall, it is concluded that this may be a very useful technique for accurately and easily measuring the capacitance, dielectric function and breakdown field values of ISAM films as compared to other techniques (e.g., air gap, parallel plate, electrodes and two-fluid). We also believe the measurement of the thin films can be extended to the characterization of films created by other nanofabrication techniques, and be potentially very useful for quality control and other manufacturing processes.

Chapter 3 LOCALIZED SURFACE PLASMON RESONANCE (LSPR) AND SURFACE-ENHANCED RAMAN SPECTROSCOPY (SERS)

Medical applications for surface-enhanced Raman spectroscopy

SERS has recently been shown effective at detecting sugar which could be of great benefit to people with diabetes [69]. It has also been proposed as a method for the detection of malignant melanoma and as a way of monitoring response to treatment and disease progression [15]. About 8000 people in the United States die each year due to malignant melanoma, a disease that can be successfully treated if detected early enough [13]. The research presented in this chapter is a feasibility study of using SERS for the detection of malignant melanoma.

Scientific interest

The surface-enhanced Raman effect was discovered in 1977 independently by Albrecht and Creighton and by Jeanmaire and Van Duyne who attributed the effect to a charge transfer mechanism and an electromagnetic effect respectively. The effect greatly increases the Raman signal from certain analytes bonded to nano-rough metallic surfaces. It has been under constant study since and has more recently experienced great improvements in the design of substrates which magnify the effect to the point where single molecule detection is possible [70]. This improvement was due to a better understanding in how to build nano-structures that are conducive to LSPR.

Theory of LSPR

The theoretical basis for LSPR was worked out in the 1970's and early 1980's. Fleischmann found that pyridine adsorbed to a roughened silver electrode had an intense Raman signal and theorized that the increase in signal was due to the relatively large surface area of the electrode resulting from the roughening process [71]. In 1977, Van Duyne and Creighton discovered independently that the increase in SERS intensity could not be explained solely by the increase in the surface area of a roughened electrode and proposed a surface-enhancement effect caused by LSPR [72] and a charge transfer mechanism [73]. Surface-enhancement as a LSPR was modeled by Gersten [74-76] and by Kerker [77] among others. A good summary of the effect can be found in Surface-enhanced spectroscopy by Moskovits [78].

For the case of a metallic nanoparticle with a molecule in close proximity **r'**, an incident plane wave with a particular frequency ω_0 meeting a resonance frequency of the metallic nanoparticle will cause the nanoparticle to become polarized and the molecule will behave as a dipole which will have the following dipole moment:

Equation 3-1

$$\mathbf{p}(\mathbf{r}',\omega) = \boldsymbol{\alpha}'\cdot\left[\mathbf{E}_i(\mathbf{r}',\omega_0) + \mathbf{E}_M(\mathbf{r}',\omega_0)\right]$$

where **α'** is the Raman polarizability, $\mathbf{E}_i$ is the incident plane wave and $\mathbf{E}_M$ is the Mie scattered electric field. Therefore the enhancement of the polarizability of the molecule, g_0 is proportional to the dipole moment divided by the normal Raman scattering, or:

Equation 3-2

$$g_0 \propto \left[\mathbf{E}_i(\mathbf{r}',\omega_0) + \mathbf{E}_M(\mathbf{r}',\omega_0)\right]/\mathbf{E}_i(\mathbf{r}',\omega_0)$$

The electric field resulting from the Raman radiation at a distance **r** from the nanoparticle is:

Equation 3-3

$$\mathbf{E}_R(\mathbf{r},\omega) = \mathbf{E}_{dip}(\mathbf{r},\omega) + \mathbf{E}_{sc}(\mathbf{r},\omega)$$

Where $\mathbf{E}_{dip}$ is the dipole field due to the molecule by itself and $\mathbf{E}_{sc}$ is the field scattered off of the nanoparticle. For scattered fields near the same frequency as ω_0 we have an additional enhancement equal to:

Equation 3-4

$$g \propto [\mathbf{E}_{dip}(\mathbf{r},\omega) + \mathbf{E}_{sc}(\mathbf{r},\omega)]/\mathbf{E}_{dip}(\mathbf{r},\omega)$$

If we define G to be the enhancement factor of the Raman signal due to the presence of the nanoparticle and if we assume that the molecule is adsorbed to the surface of the nanoparticle, then we have [77]:

Equation 3-5

$$G \cong 5\left|1 + 2g_0 + 2g + 4gg_0\right|^2$$

In the case where the metallic nanoparticle is a sphere, g and g_0 are the values of $(\varepsilon-1)/(\varepsilon+2)$ for ω and ω_0, respectively, and ε is the complex dielectric function for the nanoparticle. This enhancement factor has a resonance condition when the real component of the dielectric function is close to -2, which occurs in the coinage metals when the irradiation is in the visible or near-UV range. The equation then simplifies to the following for small Raman shifts:

Equation 3-6

$$G = 80\left|gg_0\right|^2$$

Application to SERS-- Fabrication of substrates

In order to facilitate LSPR, substrates should be fabricated that have a nano-rough surface that has features that approximate the metal sphere of the previous section. The method we used for doing this was as follows:

Glass slides were cleaned using the RCA cleaning technique where the slides were first put in to a 1:1:5 solution of ammonium hydroxide, hydrogen peroxide (30% concentration) and water at 75°C for thirty minutes. The slides were then removed, rinsed with de-ionized water and put in to a 1:1:6 solution of hydrochloric acid (30% concentration), hydrogen peroxide (30% concentration) and water at 75°C for thirty minutes. The slides were then rinsed with de-ionized water, dried with nitrogen and ready to use. Polystyrene nano-spheres in solution were drop-cast on to the prepared microscope slides and allowed to dry. The diameter of the spheres used were around 600 nm as this aided in the creation of the appropriately sized nanoparticles. The methods used to fabricate the substrates were based on the work done by Van Duyne's group [79].

The slides were then placed in an electron beam evaporator. The evaporator was placed under a high vacuum and a layer of silver two hundred nanometers thick was deposited. The resulting film was a nano-rough silver surface that had electromagnetic characteristics similar to a collection of the nano-spheres described in the beginning of the chapter. This substrate allows for LSPR to occur giving a large enhancement to the Raman signal of molecules adsorbed to the surface of the substrate. Scanning electron microscopy (SEM) shows that the film has a well covered surface of silver coated spheres.

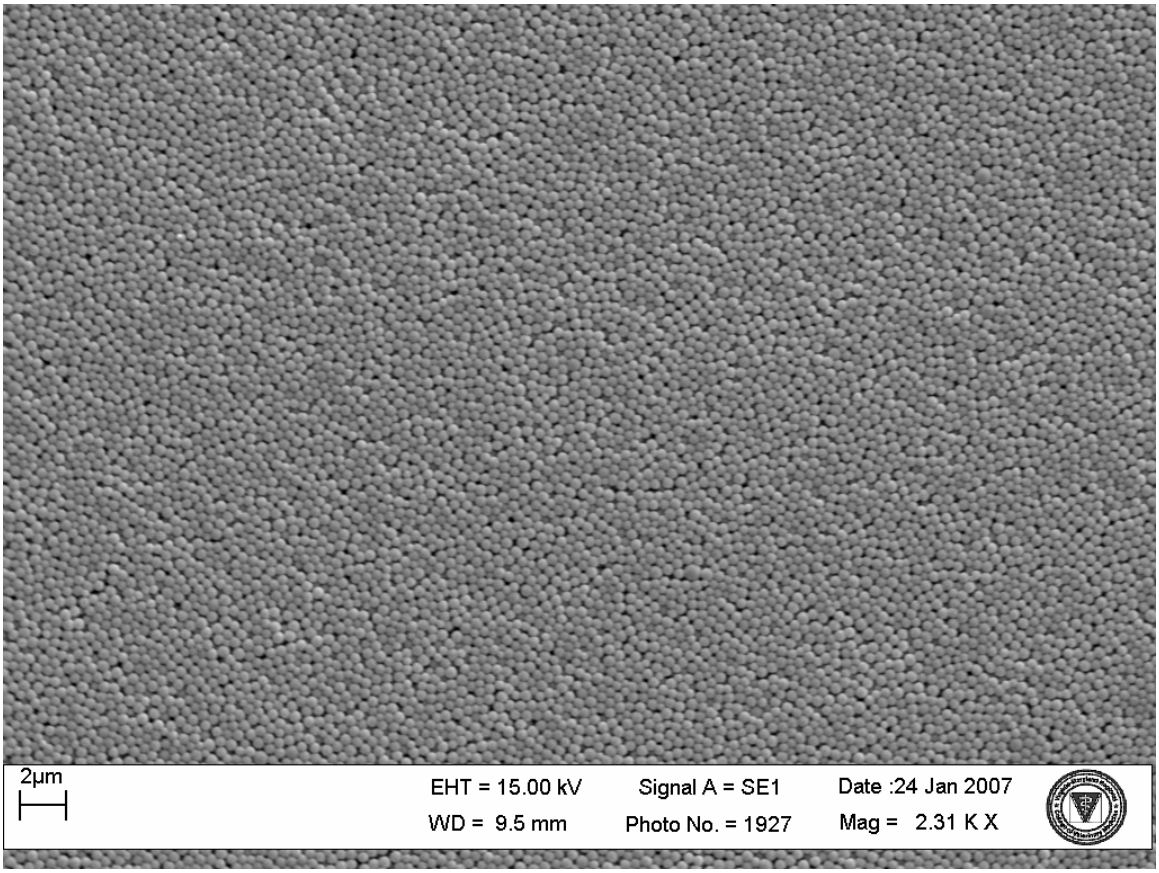

Figure 3-1 SEM image of a silver coated substrate

Description of experimental setup

The SERS measurements were made using a Raman microscope system consisting of a 785 nm diode laser, a microscope and a Roper Scientific 300i spectrometer with a liquid nitrogen cooled CCD camera. The emission of unwanted wavelengths from the diode was removed using a bandpass filter. The beam focus was maintained using a series of lens setup in a 4f focusing system. The direction of the beam path was controlled using dielectric mirrors. A rough sketch of the system is as shown in Figure 3-2:

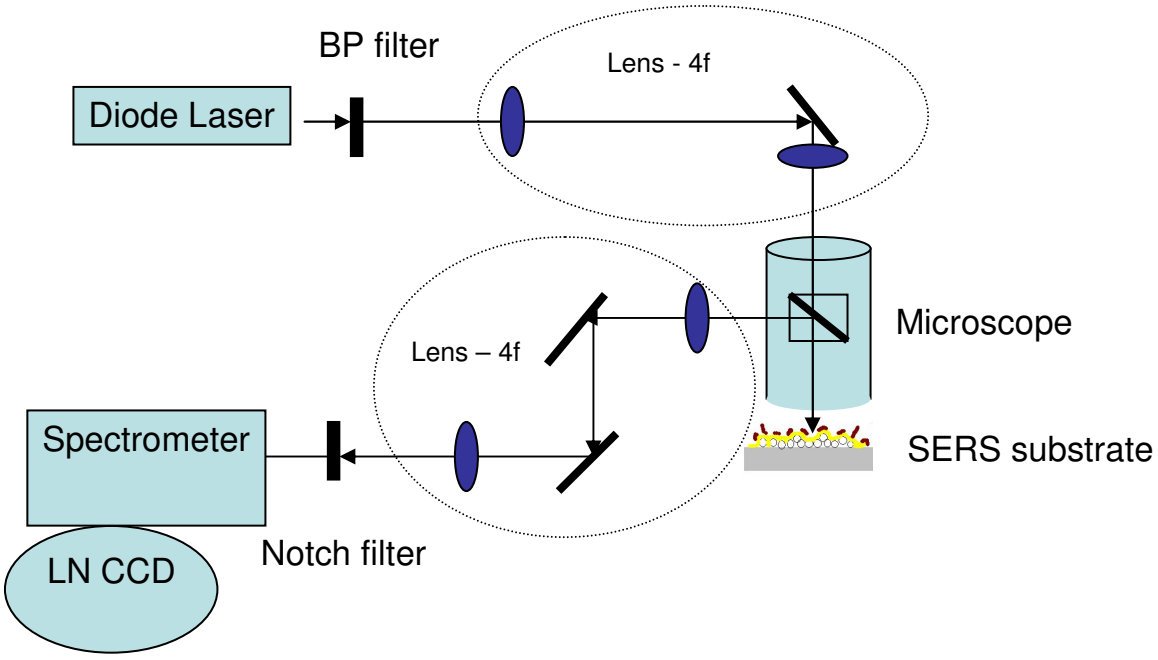

Figure 3-2 Sketch of experimental setup

Target molecules in solution were allowed to electrostatically bond to the prepared substrates for sixty seconds and then rinsed with de-ionized water. The samples were then ready for measurement by the SERS microscope system.

Results of standards

Spectra were collected from several different standards to verify that our system was properly calibrated and sensitive to our substrates. The Raman signal of beta-carotene was collected by dissolving beta-carotene in corn oil and placing a drop of the solution on a slide. The sample was measured using a 5 minute collection time. Beta-carotene was adsorbed to a silvered bead layer as described in the previous section. The SERS signal was then measured showing peaks in appropriate ranges for beta-carotene (C-C, C-H and C=C bonds) along with a few additional minor peaks probably related to the substrate. The SERS signal for beta-carotene was collected in 1 second.

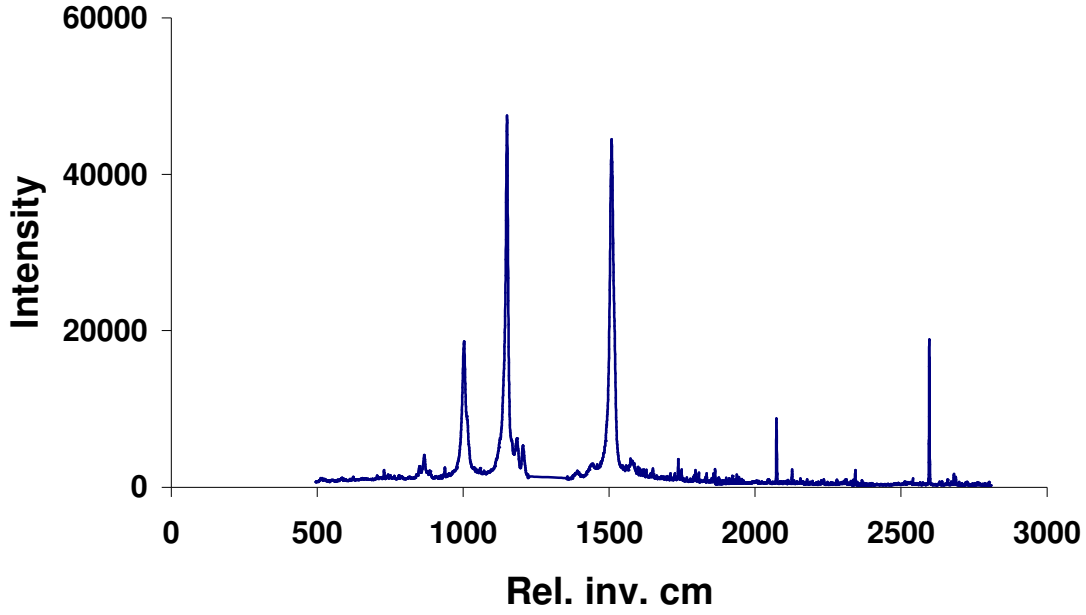

Figure 3-3 Raman spectra of Beta-carotene

The SERS spectra of Nile Blue A was also collected using the same process with an extended collection time of 30 seconds. The resulting spectra show many minor peaks across the collection range also comparing well with what is in the literature. It is also observed that there is a very strong peak with a small Raman shift indicating that there is a surface-enhancement effect as Raman scattering modes for short wavelength shifts will also be enhanced by LSPR. The dip in the signal at around 1250 rel. inv. cm occurred at the edge of an image and is probably an artifact of the measuring process.

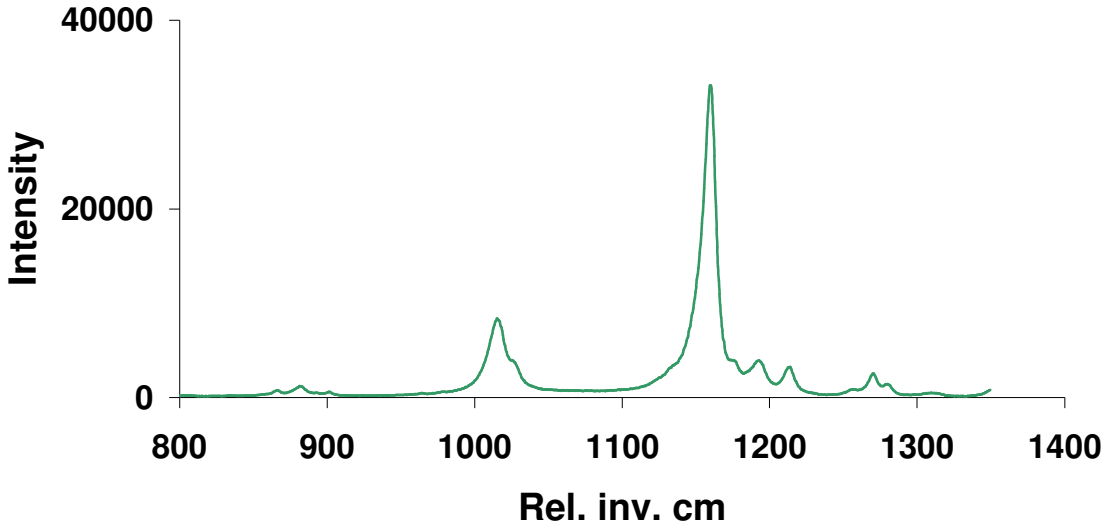

Figure 3-4 SERS spectra of Beta-carotene

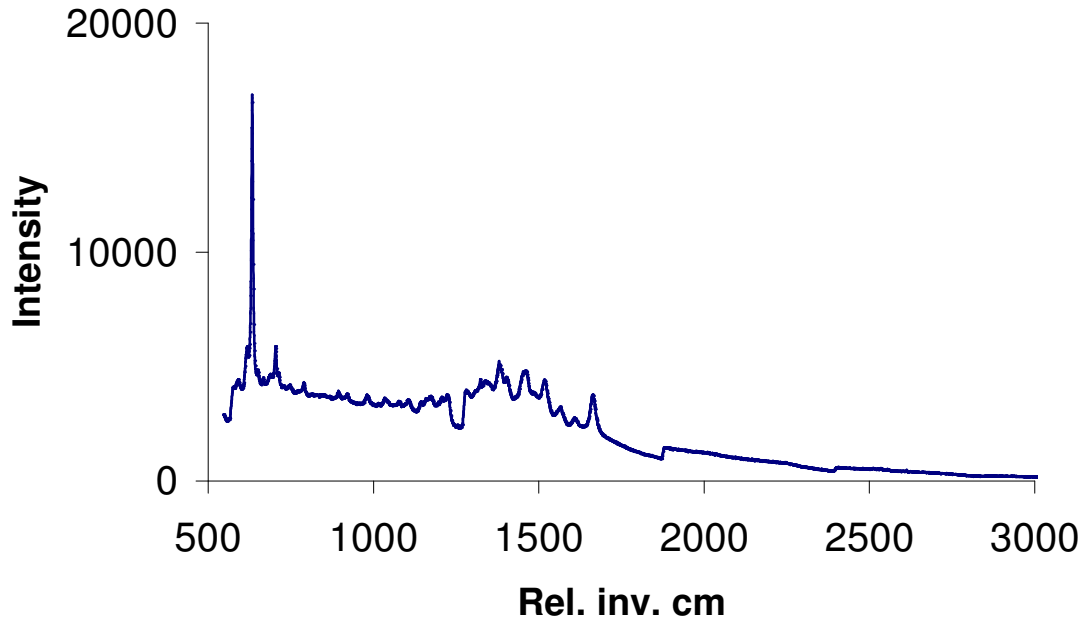

Figure 3-5 SERS spectra of Nile Blue A

Results of sera measurements

Sera were collected from blood samples obtained from healthy horses and from horses with malignant melanoma. The sera were then frozen at -30° C until ready for use. Upon thawing gently by leaving the sample container exposed to room temperature, the sera were drop-cast on to the SERS substrates and allowed to sit for about two minutes. The substrates were then rinsed in deionized water for about 20 seconds. The substrates were placed in the experiment and the SERS spectra were collected. Many of the peaks are shared between the two sample sets. Figure 3-6 shows the averages of samples collected from three healthy horses and from three horses with malignant melanoma. The background of the spectra from the horses with melanoma is somewhat higher than the background of the spectra from the healthy horses. A melanin signal is not visibly present in spectra of the melanoma stricken horses, though there are some peaks that are present in the spectra from horses with melanoma that are absent or diminished in the spectra from healthy horses. These peaks are not consistent enough across our sample set to be labeled as disease markers. Typical signals for a horse with malignant melanoma and a healthy horse are shown in Figures 3-7 and 3-8. Signals from individual samples do vary from the averages, but individual peaks present in the average of spectra from horses with malignant melanoma are not present in the spectra from individual healthy horses.

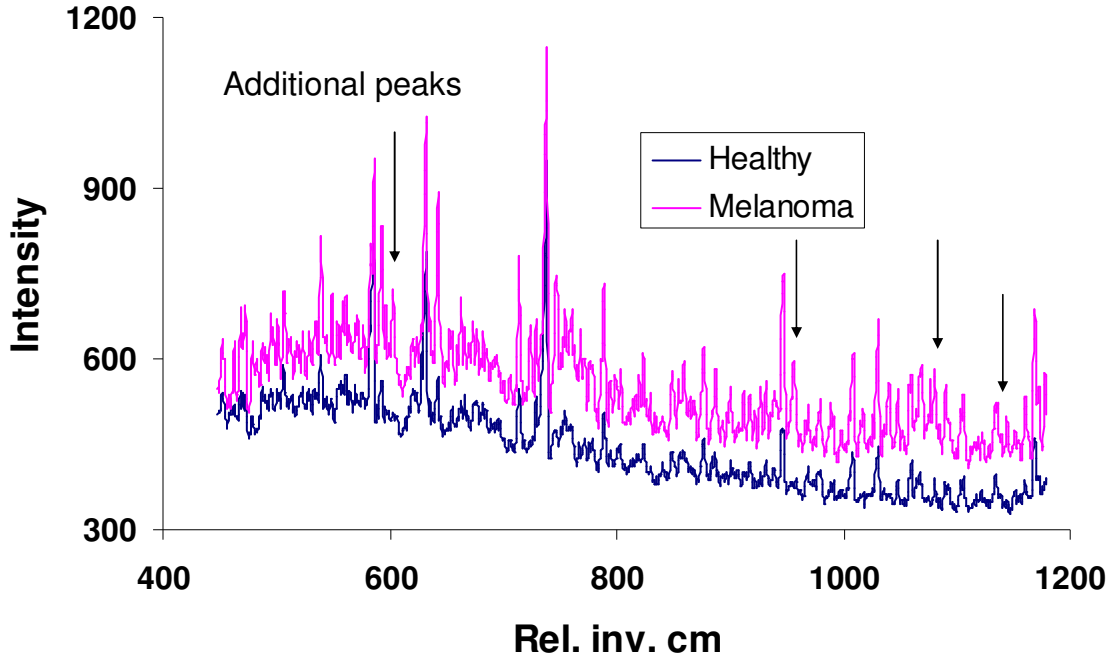

Figure 3-6 SERS spectra of sera samples from healthy horses and horses with melanoma

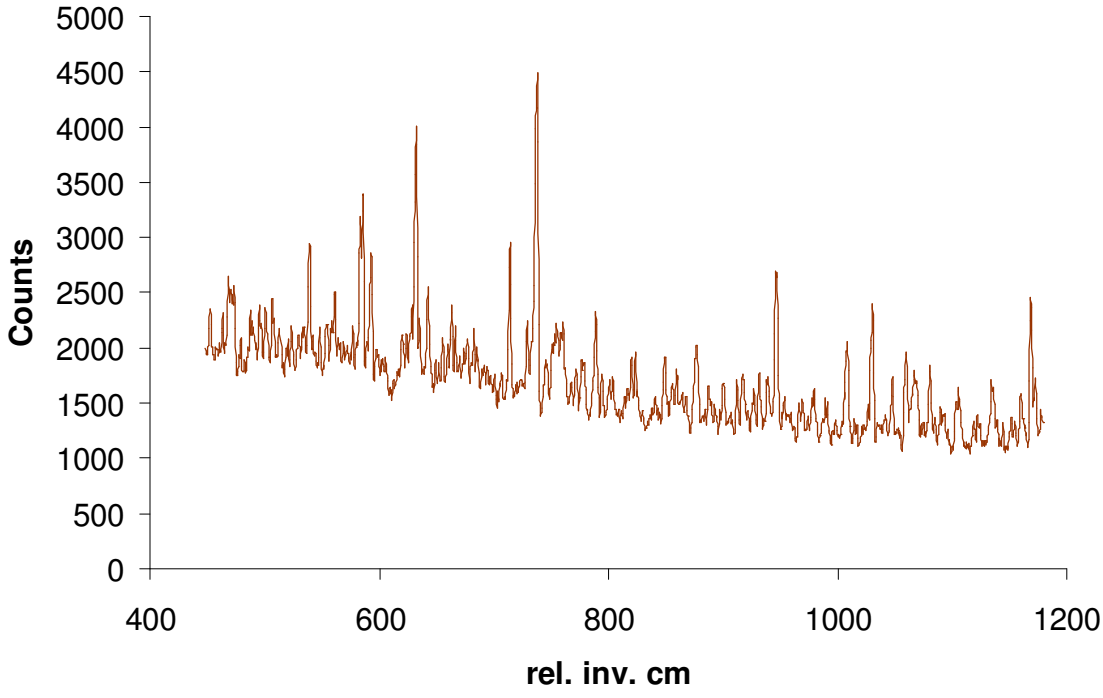

Figure 3-7 Individual SERS spectra of a serum sample from a horse with malignant melanoma

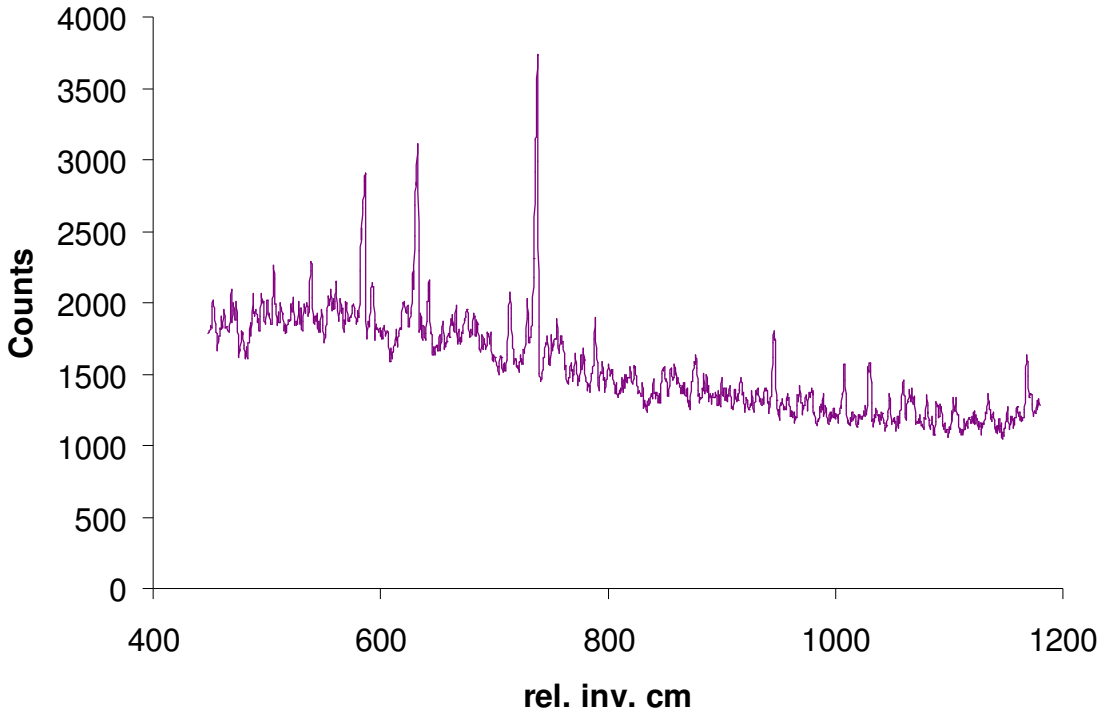

Figure 3-8 Individual SERS spectra of a serum sample collected from a healthy horse

Outlook for future success in cancer detection

This study does show that there are differences between the sera from healthy horses and horses with malignant melanoma. Some changes to the experimental setup might be necessary and the use of statistical processing might also be needed to determine definitively whether a particular serum sample is from a healthy horse or a horse with melanoma, but the future prospect for some type of screening device is promising.

Chapter 4 ABSORBANCE AND FLUORESCENCE MEASUREMENTS OF SERUM

Monitoring protein levels as a method of cancer detection

With over a million new cases of cancer in the U.S. each year, there has been an increasing emphasis the early detection of cancer that has led to a large number of different approaches to finding the disease [13]. Techniques for finding cancer range from imaging techniques such as CT-scans aimed at finding tumor masses to monitoring body fluids for cancer markers such as prostate-specific antigen (PSA) that generally is increased when prostate cancer is present. Many tests though, such as the PSA test, are only useful for detecting certain types of cancer, can have harmful side effects or be too costly for mass screening. Therefore, methods which analyze body fluids and use simple optical spectroscopic techniques could be of great value.

Variations in protein concentration ratios in blood sera have been linked to the presence of cancer in humans [25-27]. An increase in globulin levels is sometimes observed with the growth of cancer [28, 29]. The accurate measurement of these protein concentrations could become part of a routine cancer screening process. Included in this chapter is the result of a spectroscopic study performed on sera collected from healthy dogs and dogs with cancer. Absorbance and fluorescence spectra were collected from dog sera and from primary serum proteins. A process was developed using these signals for determining the concentrations of albumin, globulins and hemoglobin in blood sera. The concentrations were then analyzed for possible use in screening for cancer [3].

Sample collection and processing techniques

From a preliminary sampling of 60 dogs, serum was collected from a network of veterinary clinics in Virginia's New River Valley. Each pet owner volunteered to participate in the study and the attending veterinarian documented each animal's health on a questionnaire. Wolves, dogs with renal failure, hyperthyroidism, epilepsy or Addison's disease were excluded from this cancer screening study, because the absorbance spectra from their serum appeared to be significantly different from those of other breeds of healthy dogs or dogs with cancer. Optical screening of serum for other diseases was viewed as an area for future research beyond the scope of this paper. This study then focused on an optical comparison of serum proteins between a group of 21 healthy dogs and a group of 10 dogs with different forms of cancer; both groups contained a mixture of breeds, ages, and genders. As a separate control group, 8 geriatric dogs were also studied. In one dog with lymphoma, 8 additional serum samples were taken during an eight month period, and these were optically analyzed in order to monitor the patient's response to chemotherapy using the Wisconsin protocol. Statistically, the cancer screening study population included a total of 47 serum samples.

All serum was drawn using standard vacutainers without anticoagulant. This allowed clotting to help separate red blood cells from the serum, and kept the extraction method uniform. Blood was centrifuged at low speeds to gently move the packed cell volume to the base of the tube with minimal rupture of red blood cells. About 1 mL of serum was removed from the top of the tube and frozen for one to three years. About one hour before analysis, samples were thawed, gently mixed, and then diluted to 1/60 of their original concentration by adding 40 μL of serum to 2360 μL of deionized water in a PMMA cuvette, with an optical path length of 1 cm. This initial dilution generally kept the absorbance below 1.5 for wavelengths near 278 nm. If the peak UV absorbance was higher than 1.5, the samples were

diluted further. To maintain solution homogeneity, diluted samples were gently tipped seconds before performing optical spectroscopy or chemical analysis.

Fluorescence spectra of the diluted serum in PMMA cuvettes were acquired on a Hitachi F-4500 fluorescence spectrophotometer from 290 nm to 500 nm every 0.2 nm, at a rate of 240 nm/minute, with excitation at 280 nm, 2.5 nm slits, a 2-second integration time, and a photo multiplier tube bias of 700 V.

Absorbance spectra were acquired on a Hitachi U-2001 UV-vis-NIR spectrophotometer with pure water in a PMMA cuvette as the reference sample. For rapid data acquisition, spectra were recorded every 1 nm from 265 to 500 nm, at 400 nm/minute, with medium detector response and a UV lamp change at 370 nm. The slit width was 2 nm. Every hour, the system response was rechecked by measuring the absorbance spectra of water; if water's absorbance deviated from 0.000 by more than 0.01 near 400 nm, then the baseline was redone.

For comparison, the Veterinary Teaching Hospital Clinical Laboratory Services of the Virginia-Maryland Regional College of Veterinary Medicine performed standard automated colorimetric blood chemistry analysis to monitor albumin, total protein, and hemoglobin in known serum phantom solutions and selected canine sera. To check for other possible sources of absorbance or scattering, bilirubin and lipids were also measured in selected sera.

To compare the accuracy of spectroscopic and chemical analysis methods, known solutions of serum proteins were prepared from fresh powders, all purchased from Sigma-Aldrich (St. Louis, Missouri). Single-solute aqueous reference solutions were made at concentrations of 1 g/L for canine albumin Cohn 5 (catalog # A9263); 1 g/L for canine globulins, mainly α Cohn 4-1 (catalog # G7015); and 0.1 g/L for human hemoglobin, including methemoglobin (catalog # H7379). Mixtures of albumin, globulins, and hemoglobin

within physiological concentration ranges were made for chemical analysis and then diluted for spectroscopic analysis.

Data analysis and processing techniques

On the average, serum from geriatric dogs and dogs with cancer tended to have higher absorbance from 265 nm to 500 nm than was seen in ordinary healthy dogs, Figure 4-1. The large variability in serum absorbance within groups made it difficult to correlate a patient's health group with isolated spectral features.

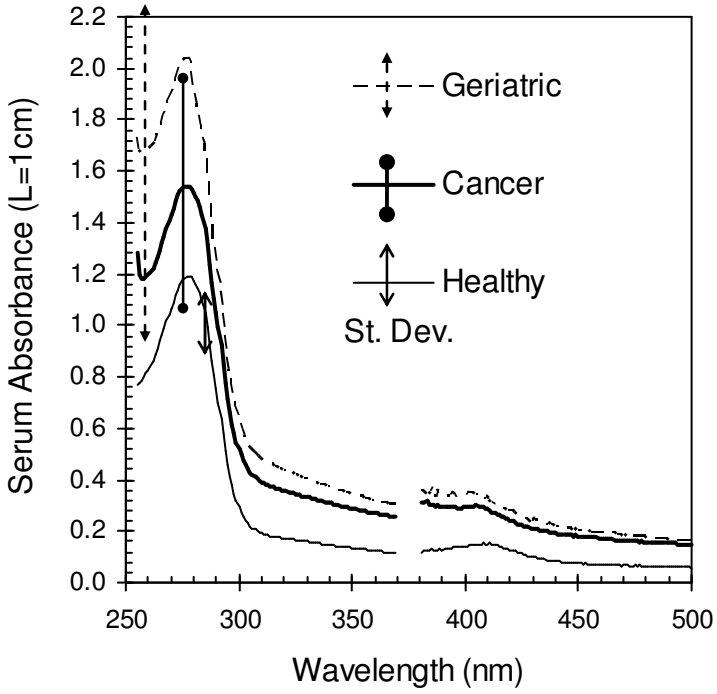

Figure 4-1 Average UV absorbance spectra for diluted serum from dog populations grouped by health status: On the average, the serum absorbance of geriatric patients and those with cancer was higher than that of healthy dogs across the wavelength range from 250 nm to 500 nm; however, there was high variability (standard deviations indicated by error bars) within the cancer and geriatric populations. The absorbance spectra shown are through samples that have been diluted in water to 1/60 of their original concentrations.

Methodical spectral analysis was able to accurately estimate serum composition, because reference solutions of albumin, globulins, and hemoglobin had distinguishable absorbance features, as shown in Figure 4-2. Although all three serum components had a peak near 278 nm, hemoglobin also exhibited a peak near 406 nm, globulins produced a significant "tail" that gradually decreased from 300 to 500 nm while albumin had no such tail or other peak. Likewise, the fluorescence spectra of these reference solutions were also unique, as seen in Figure 4-3. Hemoglobin fluoresced relatively little compared to albumin and the globulins. Globulins produced bright narrow UV emission near 332 nm, which was maximized using excitation at 280 nm. Compared to globulins, albumin fluorescence intensity was lower near 332 nm at the same solute concentration (1 g/L), and its peak was broader, so that albumin actually produced more emission near 300 nm than was seen from globulins. This difference in fluorescence peak shape provided additional information about the relative levels of albumin and globulins in fresh mixtures.

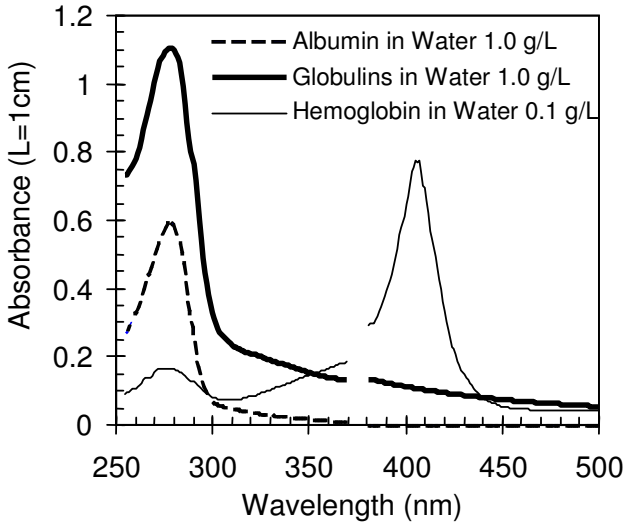

Figure 4-2 Absorbance spectra of reference solutions for primary serum proteins: The spectral gap between 370 and 380 nm is a low signal region between two light sources.

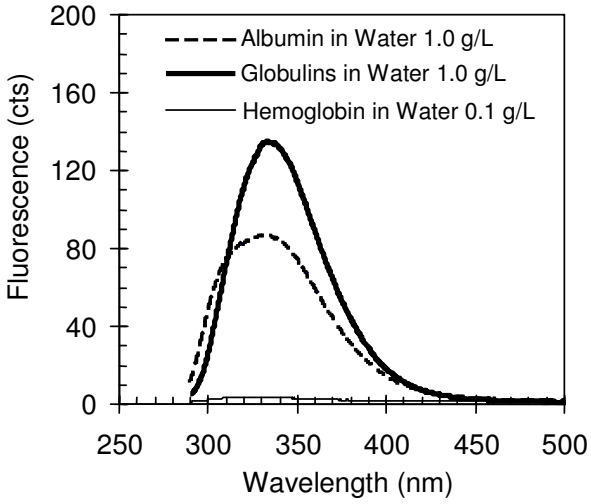

Figure 4-3 Fluorescence spectra of reference solutions for primary serum proteins: Compared to albumin, globulins exhibited enhanced fluorescence near 300 nm, while hemoglobin showed negligible fluorescence.

Absorbance peak amplitudes in Figure 4-4 were proportional to solute concentration, as expected from Beer's Law, so the observed absorbance spectra $Abs(\lambda)$ of known mixtures and diluted serum samples were modeled using Equation 4-1 to generate a fit spectrum $Abs_{fit}(\lambda)$ from a linear combination of the reference spectra for albumin $Albu(\lambda)$, globulins $Glob(\lambda)$, and hemoglobin $Hem(\lambda)$. The coefficients A, G, and H represent the estimated concentrations (in g/L) of albumin, globulins, and hemoglobin in the diluted solution. S represents the relative magnitude of a residual background absorbance (discussed below).

Equation 4-1

$$Abs_{fit}(\lambda) = \frac{A}{1.0} Albu(\lambda) + \frac{G}{1.0} Glob(\lambda) + \frac{H}{0.1} Hem(\lambda) + S \cdot Scat(\lambda)$$

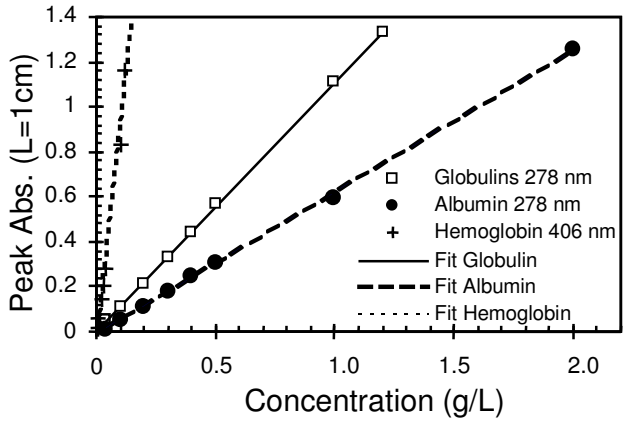

Figure 4-4 Linear absorbance of serum components: The absorbance peak amplitude at the indicated wavelengths was proportional to protein concentration

On several spectra, a high background absorbance was observed across the visible and UV region, which could not be modeled as a linear combination of albumin, globulins, and hemoglobin. To isolate this component mathematically, the residual absorbance was calculated from the sample in Figure 4-5, because it had a particularly high background. This background, $Scat(\lambda)$, was smoothed and normalized so that it equals 1.0 at 350 nm, a convenient reference point where absorbance from other components was small. Canine serum spectra were then reanalyzed with this potential contribution. For those few serum where the fit was improved by including this background component, the globulin concentration estimates were reduced back to realistic physiological levels.

Multiparameter optimization was performed in Excel to estimate the values of the coefficients A, G, H, and S which minimized the mean squared error E_{abs} between the observed and fit absorbance spectra, as defined in Equation 4-2, where n is the number of wavelengths λ in the spectra.

Equation 4-2

$$E_{abs} \equiv \left[\sum_{i=1}^{n} \left\{\left(Abs(\lambda_i) - Abs_{fit}(\lambda_i)\right)^2\right\}\right]^{1/2} \Big/ \sum_{i=1}^{n} \{Abs(\lambda_i)\}$$

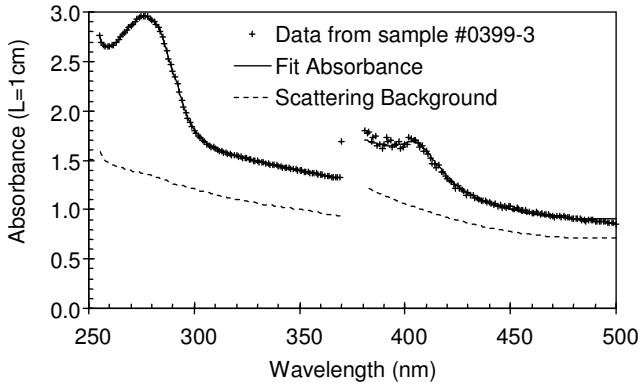

Figure 4-5 Scattering contributions to serum absorbance spectra: The absorbance spectra of some samples exhibited a significant background, which increased towards shorter wavelengths. The dashed curve in this plot shows the smoothed scattering background, Scat(λ), after normalizing the spectra so that Scat(λ=350nm) is 1.

The fluorescence peak counts of albumin and globulin solutions at 332 nm (PF_{albu} and PF_{glob}) increased asymptotically with concentration (in g/L) due to reabsorbance, as seen in Figure 4-6 and characterized by Equation 4-3. After dividing by each original peak height, the normalized fluorescence spectra $F_{albu}(\lambda)$ and $F_{glob}(\lambda)$ from these single-solute solutions maintained their unique peak shapes for concentrations up to about 1 g/L.

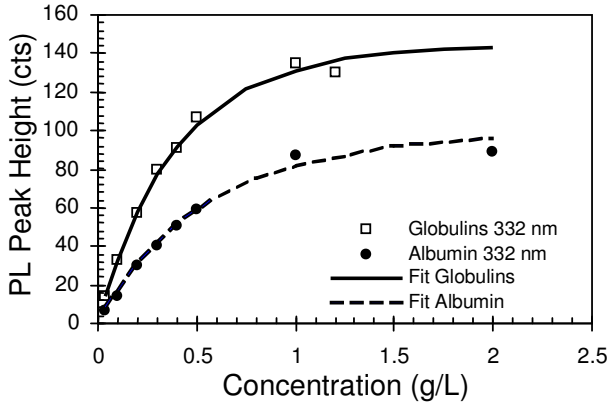

Figure 4-6 Fluorescence of serum components saturates at higher concentrations due to reabsorbance

Fluorescence spectra were modeled by scaling each normalized reference spectra by the calculated peak heights, as shown by Equation 4-4, and the fit error for the fluorescence data, E_f was calculated using an expression analogous to Equation 4-2.

Equation 4-3

$$PF_{albu} = \frac{180A}{1+1.2A^{1.2}} \qquad \text{and} \qquad PF_{glob} = \frac{368G}{1+1.8G^{1.2}}$$

Equation 4-4

$$F_{fit}(\lambda) = \frac{PF_{albu} \cdot F_{albu}(\lambda) + PF_{glob} \cdot F_{glob}(\lambda)}{PF_{albu} + PF_{glob}}$$

The diluted concentration estimates, A, G, H, and S were determined using a least squares regression analysis in order to minimize the sum of the errors, $E_{abs} + E_f$. This procedure was able to closely fit canine serum absorbance and fluorescence spectra as a linear combination of the component reference spectra, as shown in Figure 4-7. The diluted concentration estimates were multiplied by the dilution ratio to determine the concentrations

present in the serum. This method was calibrated against a series of known aqueous protein mixtures that simulated dilute serum.

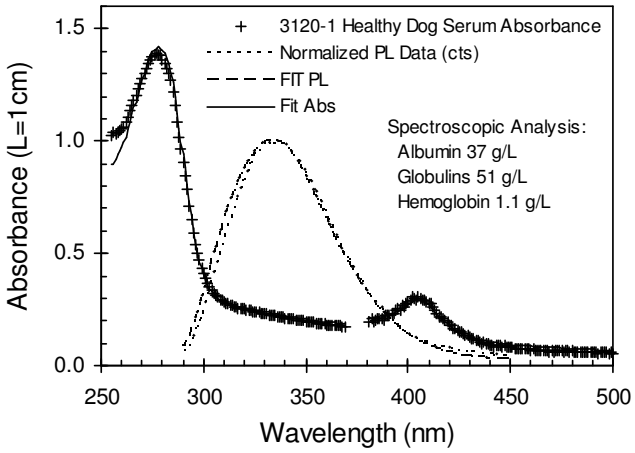

Figure 4-7 Fitting typical serum spectra: Most canine serum spectra were easily modeled as a linear combination of reference absorbance spectra and normalized fluorescence spectra from albumin, globulins, and hemoglobin.

UV spectroscopy was able to closely estimate albumin, globulins, total protein, and hemoglobin concentrations to within 10 percent of the actual concentrations in the multi-component mixtures, as shown in Figures 4-8 – 4-11. Compared to the spectroscopic method described above, standard chemical blood panel results were not as accurate, tended to underestimate globulins and total protein, and tended to overestimate hemoglobin concentrations. Such discrepancies in hemoglobin measurements are to be expected, since the standard serum chemistry methods were designed to characterize high concentrations of hemoglobin in whole blood, not very low concentrations in serum. In contrast, the spectroscopic method was a particularly sensitive and accurate method of monitoring trace hemoglobin levels in serum.

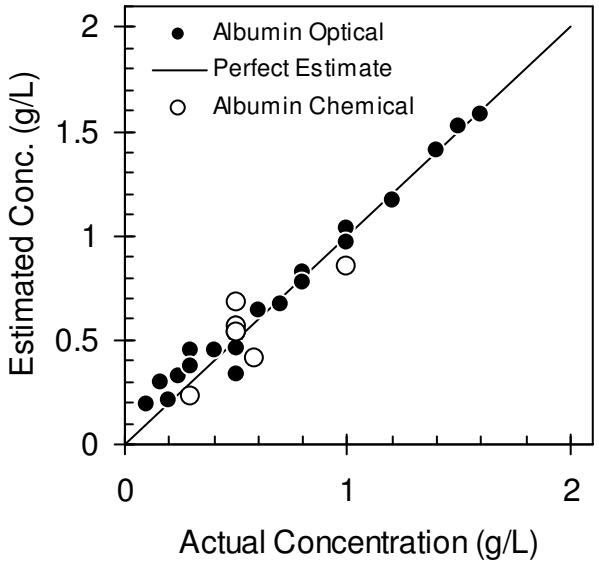

Figure 4-8 Spectroscopic estimates of albumin concentration in mixtures

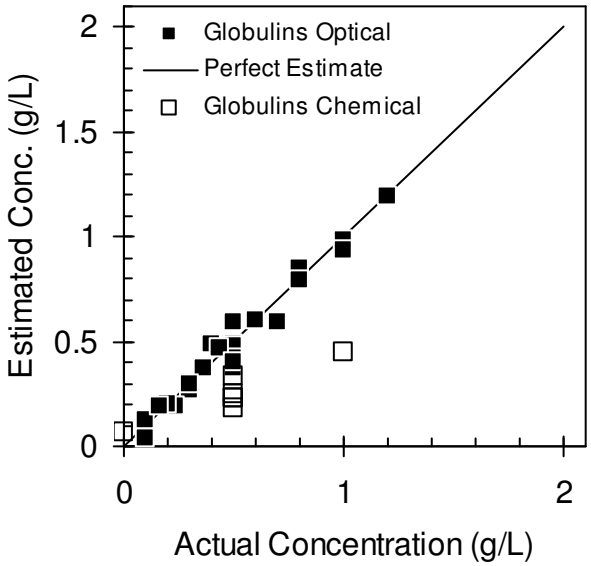

Figure 4-9 Spectroscopic estimates of globulins in mixtures: Standard chemical blood tests (labeled "Globulins Chemical") underestimate globulin concentrations.

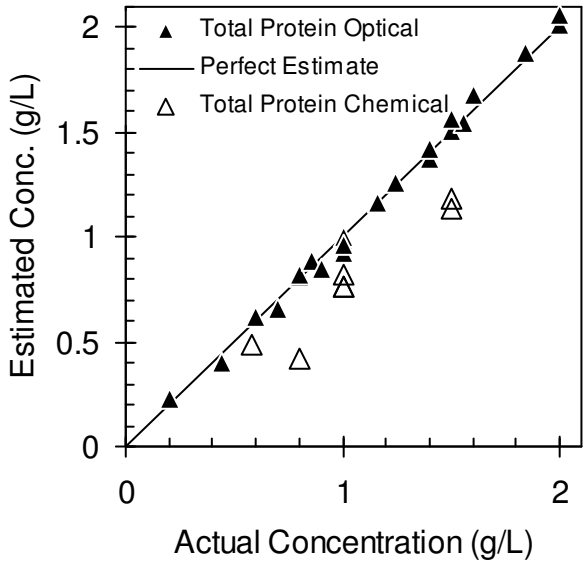

Figure 4-10 Spectroscopic estimates of total protein (albumin + globulins) in mixtures, compared to less accurate chemical test methods used in standard blood tests.

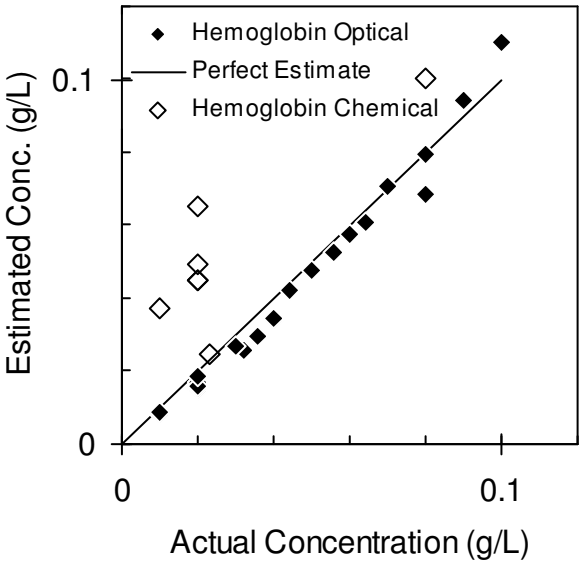

Figure 4-11 Spectroscopic estimates of trace hemoglobin concentrations in mixtures: Standard chemical blood tests (labeled "Hemoglobin Chemical") overestimate low hemoglobin concentrations.

Measurements of albumin, globulins, and hemoglobin concentrations in serum via the spectroscopic method could be useful as part of a general cancer screening process. When globulin concentrations were plotted versus albumin concentrations in Figure 4-12, there was

a range of concentrations with moderate albumin and globulin concentrations that described only healthy patients. Therefore, if the albumin concentration was between 40 and 80g/L, and if the globulin concentration was simultaneously between 17 and 37g/L, then the dog's blood protein concentration ratios were labeled "safe." By plotting hemoglobin versus total protein (albumin plus globulin concentration) in Figure 4-13, it was seen that most dogs with cancer had low serum hemoglobin concentrations. So, if the hemoglobin concentration was below 0.2 g/L, the serum parameters were labeled "suspect", as shown in Figure 4-13. If a dog's serum composition met the "suspect" criteria and did not meet the "safe" criteria, then further tests for cancer would be advised. Using these criteria, about 70 % of the dogs with cancer were correctly detected (30 % false negatives), and about 20 % of those dogs flagged for further cancer testing would be expected not to show any clinical signs of cancer (20 % false positives). This set of criteria effectively reduces the probability of mistakenly flagging a healthy dog for further cancer tests.

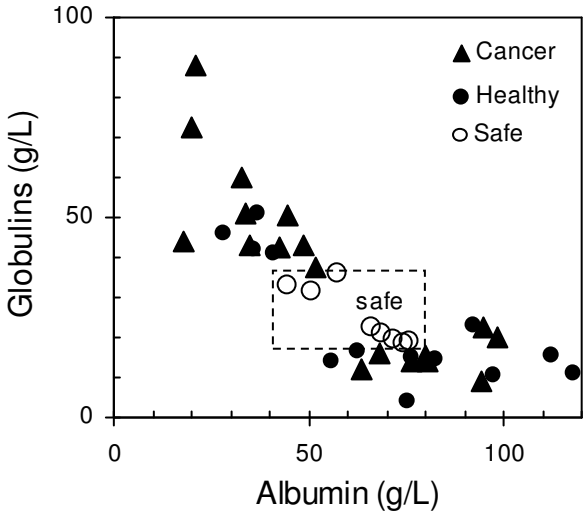

Figure 4-12 Identifying selected low risk patients from based on globulins and albumin concentrations in serum. The "safe" subset of healthy patients could be excluded from the high risk population based on their albumin and globulin concentrations, regardless of their serum hemoglobin and total protein concentrations.

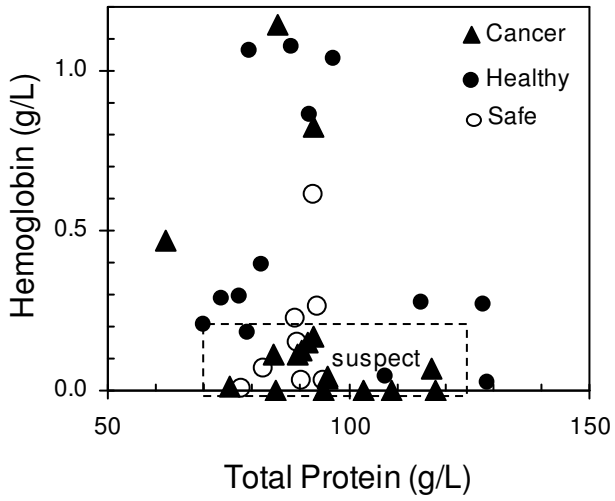

Figure 4-13 Screening for cancer based on hemoglobin and total protein concentrations in serum. Most of the cancer patients had lower serum hemoglobin concentrations than the healthy patients, as shown in the "suspect" compositional region.

Value of technique

This spectroscopic method of analyzing serum exhibited several advantages over conventional photo-chemical blood panels. The spectroscopic protocol described above only required 40 μL of blood serum to simultaneously measure albumin, globulins, and hemoglobin concentrations, with no consumable chemicals besides water. The blood chemistry lab, on the other hand, required 400 μL, because each of these three constituents had to be analyzed in separate volumes with different photometric reagents. Compared to the conventional photo-chemical approach, the spectroscopic method is therefore inherently simpler to automate, while yielding more accurate results, especially in the determination of trace concentrations of hemoglobin in serum. These features facilitate the potential use of serum spectroscopy as part of a preliminary canine cancer screening process.

The UV wavelength range from 250 to 500 nm was well-suited for rapid determination of canine albumin, globulins, and hemoglobin concentrations. Three common

forms of hemoglobin listed below all have a strong peak near 410 ± 5 nm [31]. Therefore, estimates of hemoglobin based on this peak were not affected by hemoglobin's oxidation state or its tendency to form protein complexes. The absorbance wavelength range could have been extended to 650 nm to include well-known secondary peaks for hemoglobin in several forms: oxyhemoglobin at 576 nm, methemoglobin at 630 nm, or methemalbumin at 540 nm [31], however these peaks were not necessary to estimate the total hemoglobin concentration, and they were of negligible amplitude after the ideal 1/60 dilution for UV absorbance. It is possible that the chemical specificity of standard blood panels may limit their accuracy in estimating low hemoglobin concentrations in serum. For example, hemoglobin that is bound to albumin would not bind to the photometric reagent, and so the methemalbumin component would be under-reported. Sensitive hemoglobin monitoring in serum may indirectly characterize red blood cell wall strength or frailty, if the applied stress from the blood drawing technique is kept constant.

The endogenous spectroscopy technique described here is limited, in that it does not detect trace amounts of several common serum pigments. Even when canine serum samples were only diluted to 1/4 of their original concentration for absorbance near unity in visible wavelengths, none of the characteristic visible absorbance peaks were observed for carotenes, xanthophylls, porphyrins, or bilirubin. Using automated colorimetric techniques, bilirubin was generally found at normal physiological concentrations (~2 mg/L) in selected canine serum samples by clinical laboratory services.

Rather than focusing on single marker proteins, this cancer screening technique uses patterns in the patient's albumin, globulins and hemoglobin concentrations. Graphically, the approach shown in Figures 4-12 and 4-13 is similar to principle component analysis, by which populations can sometimes be identified with clusters of data points when one basis vector of

the parameter space variability is plotted versus another. However, the approach documented here has the intuitive benefit of physically defining what each component represents. It is understandable that healthy dogs in this study had moderate levels of globulins, whereas dogs with cancer tended to have either elevated globulins (suggesting in this case a systemic response to carcinoma) or reduced globulins (suggesting an immune suppressed state).

There seems also to be a compensating mechanism in dogs which works to keep the total protein concentration between 70 and 120 g/L. This hypothesis is supported by the clustering of data points along a diagonal line in Figure 4-12, and by the strong negative correlation coefficient between globulins and albumin concentrations in Table 4-1.

This spectroscopic method was able to monitor a patient's response to therapy by tracking concentrations of free hemoglobin in serum as well as albumin and globulin concentrations. This technique could be widely used to optically monitor changes in a patient's health. It is well known that the relative concentrations of albumin and globulins change with a patient's health status. In this case, a dog's response to therapy was optically monitored with the goal of tracking the progression or regression of cancer. Figure 4-14 shows how serum proteins and hemoglobin in a dog varied over the course of its treatment for cancer, which is outlined in Table 4-2. Reduced albumin concentrations were often associated with elevated globulin concentrations, while the total protein concentration remained fairly constant. In practice, such a test could be performed as part of a routine check-up, to establish a healthy baseline pattern. Then, personal deviations from one's own baseline would be clear. This would avoid the challenge of establishing general rules to account for many possible sources of serum compositional variation, such as age, diet, medical history, gender, heredity, etc.

Table 4-1 Correlation coefficients between canine serum protein concentrations and health group*

	G	H	A+G	A	A/G	S
Globulins, G	1.00					
Hemoglobin, H	0.09	1.00				
Total Protein, A+G	0.06	-0.25	1.00			
Albumin, A	**-0.77**	-0.23	**0.59**	1.00		
Albumin:Globulins Ratio, A/G	**-0.74**	-0.04	0.18	**0.71**	1.00	
Scattering, S	**0.34**	**0.72**	-0.13	**-0.35**	-0.18	1.00
Healthy group	**-0.36**	0.06	-0.18	0.17	0.23	-0.22
Cancer group	0.17	-0.01	-0.14	-0.23	-0.15	0.15
Geriatric group	0.25	-0.08	**0.43**	0.07	-0.11	0.10

***In this comparison of 47 samples, correlation coefficients that are larger than 0.28 are statistically significant (i.e. $p < 0.05$), and these coefficients are shown in bold. Underlined coefficients are near this threshold, but the probability is greater than 5 % that the correlation between factors occurs just by chance; so such relationships are worth noting but with caution.**

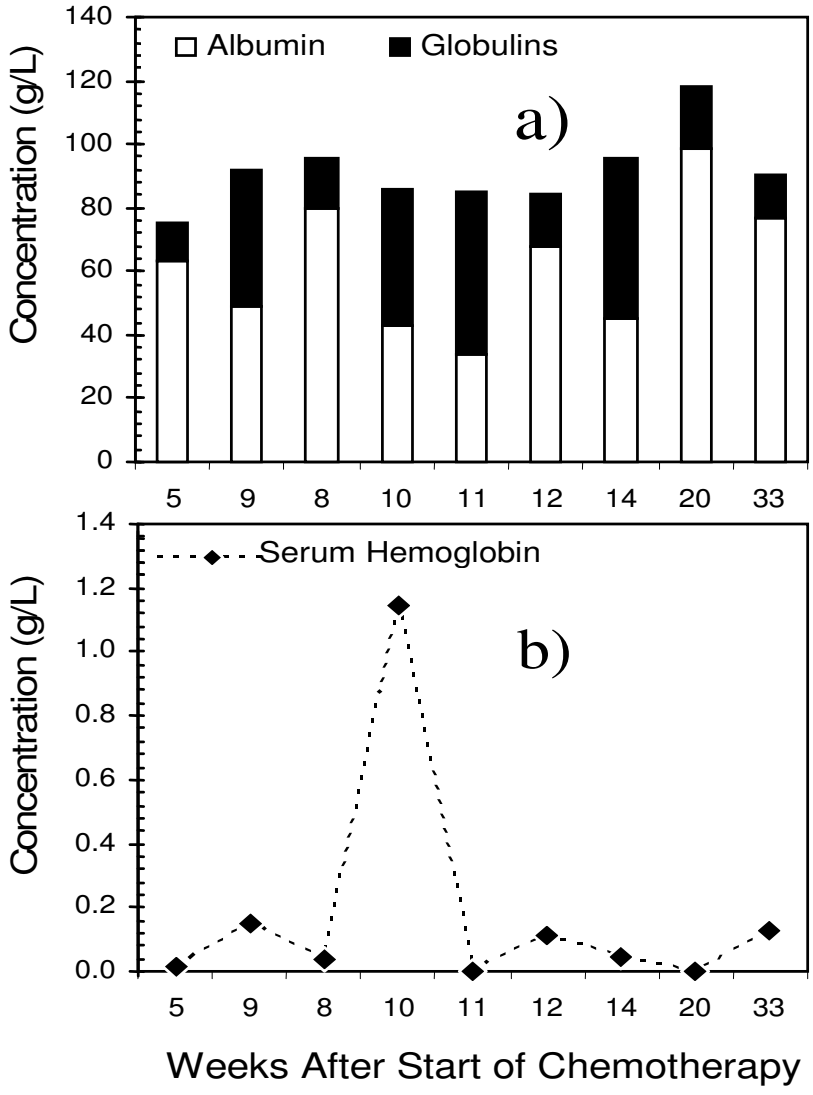

Figure 4-14 Tracking temporal changes in serum composition for a dog with cancer: During the course of treatment following the Wisconsin protocol, fluctuations in serum protein composition a) and hemoglobin levels b) were observed using the optical methods described in this paper. The cause of the hemoglobin spike after 10 weeks of chemotherapy is unknown, but this dog's medical history is outlined in Table 2.

Table 4-2 Medical history of a dog treated for lymphoma

Week*	History
-3	A 5 year old female (not neutered) Border Collie was first examined by Kirby at Companion Animal Clinic. Patient showed neck swelling and generalized lymphadenopathy.
0	Treatment began with injection of chemotherapy following the Wisconsin protocol for 19 weeks.
3	Right submand lymph node was ruptured. Analysis of a fine needle aspirate resulted in diagnosis of lymphoma with high grade cell type.
8	Viveristine was given. Despite cancer, overall health of the dog appeared good.
9	Daxorubacin was given.
12	Cytoxan was given.
14	Tumor has generalized.
19	Last treatment was given.
33	Patient was out of remission for lymphoma, and health had deteriorated from good to fair. Observations included tumor presaps, pophtcals, submand, and enlarged lymph nodes.

***This is the number of weeks after the start of the Wisconsin protocol for chemotherapy. The corresponding results of sequential optical serum analysis are shown in Figure 4-14 a & b.**

The normalized fluorescence spectra shape of known serum phantoms was a helpful indicator of component protein concentrations. On the other hand, the fluorescence spectra of dog serum in this study were considered less reliable, since they showed no significant spectral shape change, even when the absorbance spectra clearly indicated changes in the

albumin to globulin ratio. Perhaps fluorescence is more sensitive than absorbance to serum aging. Further research is needed to assess the stability of serum proteins and their fluorescence spectra after years of frozen storage and after repeated freeze-thaw cycles.

It was hypothesized that the occasional presence of broadband absorbance was due to turbidity, perhaps from aggregated albumin complexes. This was suggested by the association of high scattering with reduced albumin concentrations in serum samples, as seen in the correlation coefficients listed in Table 4-1. The turbidity was highly variable and was not significantly different in the serum of healthy and cancer populations.

To test and refine the initial cancer screening method and identification criteria presented here, further research is needed using a larger population of canine serum samples. The ultimate goal is to develop a preliminary cancer screening method for human serum. It is reasonable to expect that this spectroscopic method, which was demonstrated for canine serum and serum phantom solutions, would also be able to estimate human serum albumin, globulins, and hemoglobin concentrations, possibly using a different ideal dilution ratio to keep the 278 nm absorbance peak amplitude near 1. Of course, human and canine sera have different normal physiological ranges, so the boundaries of the "safe" and "suspect" serum parameter regions would need to be redefined based on statistical analysis of large well-defined patient populations.

Conclusion

A spectroscopic test method was developed for accurately determining the concentration of albumin, globulins, and hemoglobin in blood serum and for characterizing its turbidity. This test method compares measured near-UV absorbance and fluorescence spectra to a linear combination of reference protein spectra. The accuracy of this method exceeds that of

standard blood chemistry panels and it detects trace levels of hemoglobin in any of its common chemical forms, while requiring a total of only 40 μL of serum. This analytical method provided a sensitive way to track changes in serum composition over time to monitor the progression of cancer and to evaluate a patient's response to therapy.

This technique formed the basis of an initial cancer screening test that was demonstrated in a pilot study of 39 dogs. Using logical criteria involving the measured concentrations of albumin, globulins, and hemoglobin in serum, 70% of all patients with cancer were correctly identified as needing further tests; and only 20% of the flagged patients showed no clinical signs of cancer. Since dogs provide a good model of cancer development and effective therapy in humans, a similar approach may help identify humans with undetected cancer.

Chapter 5 DIELECTRIC FUNCTION MEASUREMENTS OF THE MELTING POINT OF DNA

The structure of DNA

The DNA molecules that encode the genetic information of living organisms can be either single stranded (ssDNA) or double stranded (dsDNA). They are made of a proteinaceous/carbohydrate backbone and sequences of four bases, including adenine (A), guanine (G), cytosine (C) and thymine (T) [45]. A is always paired with T connected by two hydrogen bonds and C with G connected by three hydrogen bonds. Thus, the G-C pairing is more stable than the A-T pairing due to the stronger hydrogen bonding. Additionally, the A-T pairings of dsDNA molecules are more vulnerable to melt (or unzip) [45]. The backbone consists predominantly of five carbon sugar molecules that give the DNA strands a chemical polarity. In all DNA molecules, one terminus starts with a phosphate group (called the 5' end), and the other terminus with sugar molecules (called the 3' end).

dsDNA molecules have double helix structures consisting of two ssDNA strands that are bonded in opposite directions (one from 5' to 3' and the other from 3' to 5'). Depictions of DNA molecules are readily available in the literature [45]. DNA melting (denaturization) is the process by which double-stranded DNA unwinds and separates into two complementary single strands through the breaking of hydrogen bonding between the two strands. dsDNA molecules can be melted into two ssDNA by heating or increasing pH (up to pH 11 or more). In addition, electrolyte addition can shift the melting point of the dsDNA toward higher temperature. For this purpose, Pt, Na and K or their complexes are the most commonly used ones [80]. For populations of DNA molecules, the melting

temperature (T_m) is defined as the temperature at which half of the DNA molecules are in the double- stranded state and half are in the single stranded states [81]. There are numerous theoretical models of DNA melting [82]. The melting point is most often found using calorimetric or spectroscopic methods [83]. Spectroscopic techniques, including the observation of the increase in intensity of the Raman profile as bases un-pair during melting, have been shown to be accurate to within 5° C [84] and observing changes in the UV absorbance spectra throughout the transition range with temperatures ranges of up to 15° C [85, 86]. Calorimetry can also be used to determine the melting point of DNA with similar accuracy by calculation from the enthalpy and entropy [87]. Spectroscopic and the more difficult calorimetric techniques can provide enthalpy results differing by more than 10% [88, 89], indicating that an improved method of experimentally determining the melting point of DNA could be of great value. Since cell death in some cancer treatments can be related to DNA unzipping at elevated temperatures (hyperthermy), an alternate way to accurately determine the melting temperature of specific DNA sequences in cancer cells could prove to be very useful in monitoring the course and efficacy of therapy.

The electrical properties of DNA have been studied by a number of different researchers since 1950 [90-93]. In general, however, these investigations did not analyze DNA whose sequences were known or probe in detail the phenomenon of DNA melting of known sequences. These techniques allow the determination of the melting temperature of known short sequences of DNA, but can be difficult to implement, and do not always produce results that are consistent.

A number of different theoretical models for determining the melting temperature of short known DNA sequences have been developed although their predictions are often at variance [82, 94]. The purpose of the present preliminary study is to demonstrate the

capability to accurately determine the melting temperature and to estimate the change in entropy and enthalpy of short known DNA sequences in solution as a function of temperature. This is accomplished through the measurement of the variations of the real relative dielectric function as a function of temperature, electrical field strength and frequency in the vicinity of the melting transition. Experimental data obtained for two different known short sequences of DNA are presented. An analysis methodology is then described and used to determine the melting temperatures, T_m, melting entropy and melting enthalpy of the DNA. A comparison of the values of T_m is then made with the values predicted by the various T_m theories in the literature to provide some measure of their comparative accuracy. Finally, the implementation of this research in a practical high throughput microfluidic device is discussed.

Methods and materials

Determination of T_m

Multiple methods have been developed over the years for predicting the melting temperature, T_m, of short DNA sequences. Basic (or original), salt corrected and nearest neighbor thermodynamic models were used to predict T_m for the two DNA sequences used in our experiments. The basic model [95] computes T_m based on the number of A, T, G, and C bases. In this basic model, the DNA and monovalent salt concentrations are assumed to be 50nM and 50mM, respectively. Three salt corrected models were considered [96-98], which differ in the salt concentration, the G/C content, and the oligonucleotide length adjusting terms. These salt corrected methods assume 50nM for the DNA concentration. Finally, seven nearest neighbors' models were used [99-105]. These take into account the neighboring base sequence but differ in the nearest neighbors' thermodynamic parameters

(i.e. enthalpy, entropy, and free energy transitions). Within these seven models, three salt correction methods were employed [81, 98, 102]. Finally, the most recent nearest neighbors' thermodynamic model, which includes a quadratic term for salt concentration correction as opposed to linear, was used as well [80]. In total, 26 models were used in order to predict T_m for both DNA sequences used in the dielectric experiments in order to validate our experimental process. All of these models assume short DNA sequences (i.e. usually fewer than 30 bases).

Sample preparation

The sequences were purchased from Integrated DNA Technologies. Sequence 1 was 5'-CAAAATAGACGCTTACGCAACGAAAAC-3' along with its complement and sequence 2 was 5'-GGAAGAGACGGAGGA-3' along with its complement. The molecules were dissolved in RNase-fFree Duplex Buffer (100 mM/liter potassium acetate, 30 mM/liter HEPES and pH 7.5). The sequences were supplied as 163.1 nmole of sequence 1 and 179.1 nmole of sequence 2, respectively. After a high speed centrifugation of the oligonucleotides in tubes (prior to opening), the DNA samples and 5 ml of buffer solution were mixed and heated to 94° C for two minutes in a hot bath. The molecules in the prepared solution were allowed to hybridize into dsDNA sequences as the solution cooled to room temperature. The sample solutions were then stored in a freezer at -20° C until use.

The volume of the measurement cell used was 2.44 ml. The DNA mole fraction for the sequences can then be calculated from the amounts of DNA molecules that were present in the cell during measurements (i.e. 0.080 and 0.087 μmole for sequences 1 and 2 respectively).

Equation 5-1

$$\text{mole fraction} = \frac{n_{DNA}}{n_{DNA} + n_{H_2O} + n_{potassiumacetate} + n_{HEPES}}$$

where the n_x refers to the moles of component x. The DNA mole fractions were found to be equal to 6.0×10^{-7} and 6.5×10^{-7} for sequences 1 and 2 respectively.

Description of fluid cell

A fluid cell was fabricated from a 5.4 mm sheet of Plexiglas for measurements of the dielectric function. The cylindrical sample containment chamber had a diameter of 24 mm, a thickness of 5.4 mm and a volume of 2.44 ml, and was sealed using 60 μm thick plastic sheets. The cell is shown in Figure 5-1. Based on the concentration of the sample and the volume of the measurement cell, the amount of dsDNA initially in the cell for measurement purposes was ~0.080 and 0.087 μmole for sequence 1 and 2 respectively. This implies that when the cell was filled with dsDNA initially, there were 4.8×10^{16} molecules of sequence 1 in solution for the first series of measurements and 5.2×10^{16} molecules of sequence 2 in solution for the second series of measurements that contributed to the dielectric response.

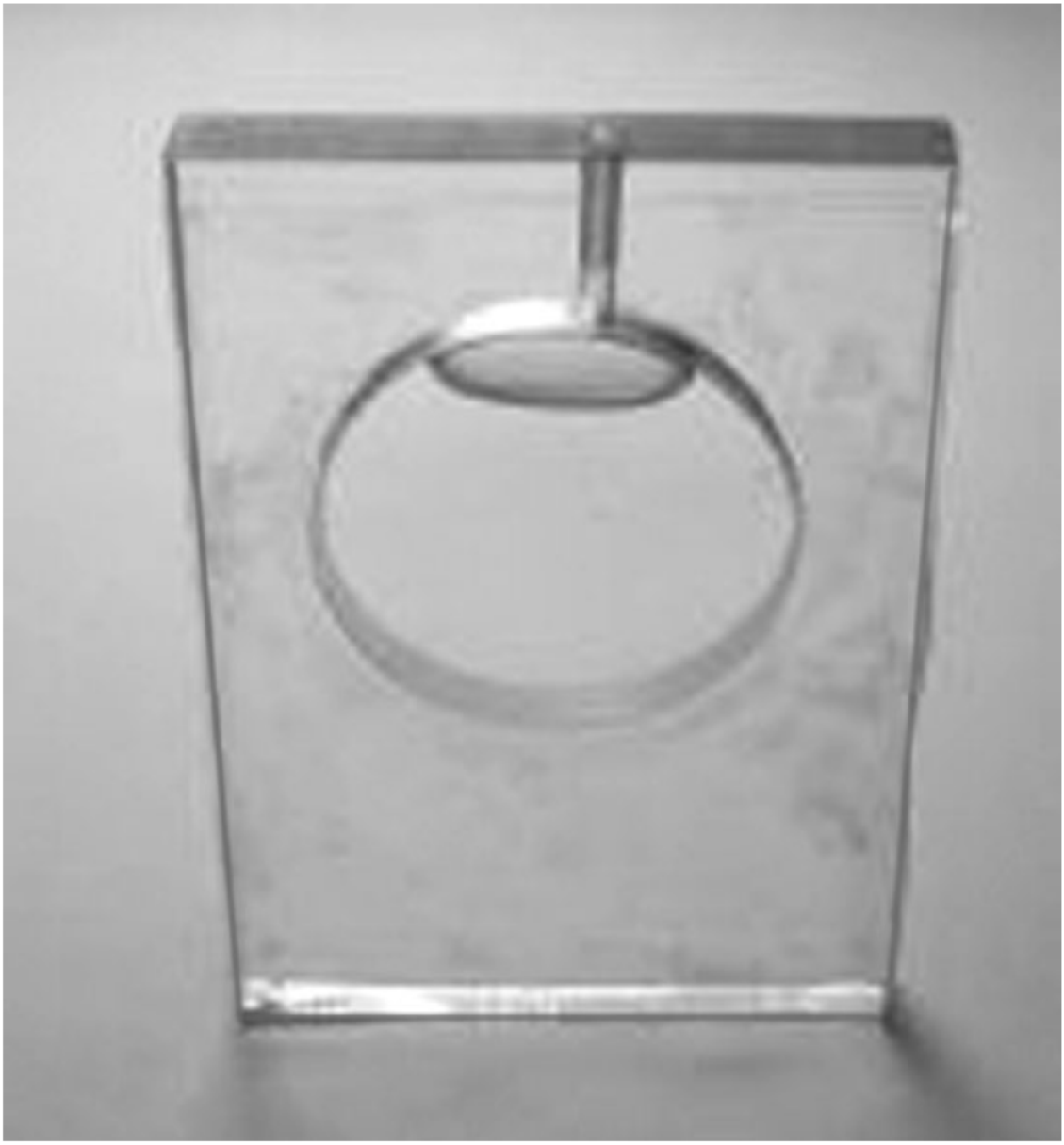

Figure 5-1 Plastic dielectric fluid cell

Measurement electrodes

The measurement electrode configuration used a standard guard ring configuration as shown in Figure 5-2. The diameter of the inner electrode was 24 mm, with a 1 mm gap separating it from the guard ring. The separation between the guarded electrode and the plane opposite was 5.52 mm (cell chamber thickness plus the thickness of the two plastic cover sheets). The

central electrode was connected to a low-Z input cable, the base plate was connected to a high-Z input cable and the guard ring was connected to the grounded cable shields[106].

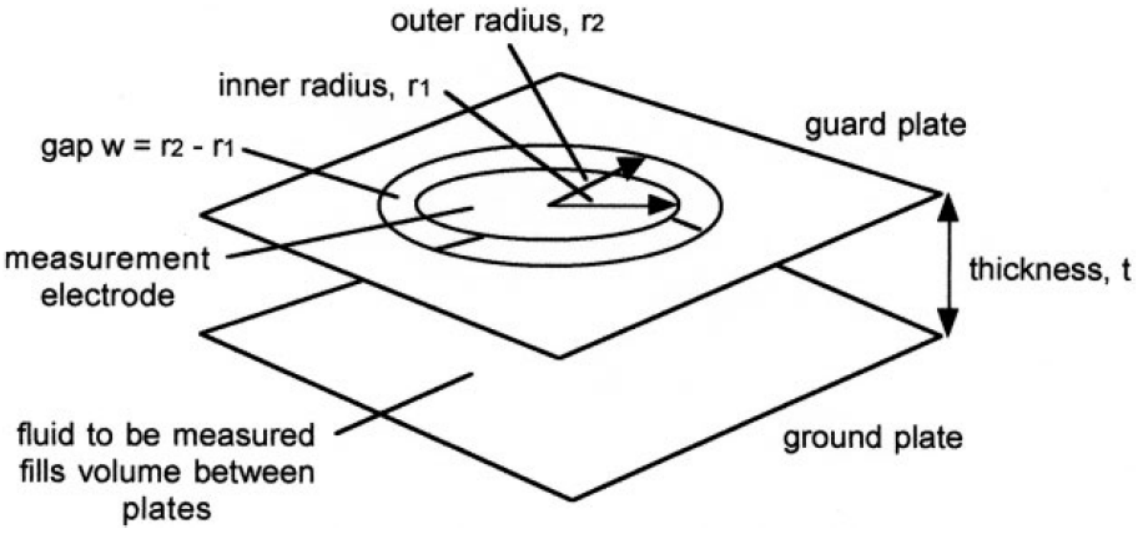

Figure 5-2 Configuration of measurement electrodes

Calibration of fluid cell

The electrical properties of the fluid cell were determined using the measurement electrodes and a commercially available AH 2700A Ultra-Precision 50 Hz-20 kHz Capacitance Bridge manufactured by Andeen-Hagerling, Inc. In order to compensate for the effects of fringing fields and the presence of the two plastic cover sheets, the cell was calibrated using the known dielectric function variation of distilled water with temperature [106]. The linear relationship of cell capacitance to real relative dielectric function was found to be

Equation 5-2

$$\varepsilon = 33.1 + 0.565\ C$$

where ε is the real relative dielectric function and C is the measured cell capacitance in pF. The correlation constant for the calibration fit was $r = 0.998$.

Experiment configuration

The experimental set-up is shown in Figure 5-3. The fluid cell was placed in a temperature and humidity controlled chamber (Espec SH-240 manufactured by Hendrick Environmental Systems & Controls, Inc.) which was used to vary and control the temperature. A feed-through cable connected the cell and measurement electrodes to the external capacitance

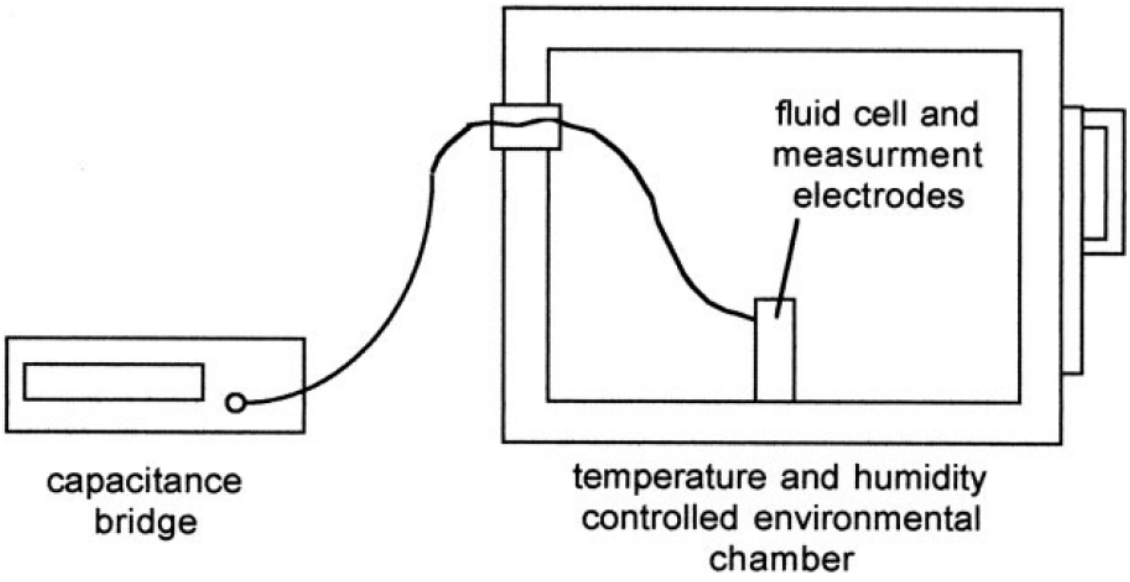

Figure 5-3 Experimental setup

bridge. During the tests, temperature, frequency and voltage were varied over the ranges ~40-65° C, 50 Hz to 20 kHz, and 0.01 V to 15 V, respectively. The variation in measurement field strength (between 1.8 V/m and 2.7x103 V/m) was shown not to significantly affect the measurement values, as opposed to the frequency variations which clearly did. There was a stabilization interval of 60 minutes for every temperature change before a measurement was taken. Each experimental run began at a low temperature (~40° C). The temperature was then increased in discrete increments (2° C) with measurements taken after the temperature had stabilized. A matching set of measurements was made decreasing the temperature back to the initial starting temperature. When it appeared that

there was hysteresis in the data, a limited number of runs were done using a 24 hour stabilization time. When this was done, the apparent hysteresis became less than the measurement variability. Hysteresis may exist, but this experiment did not show any clear evidence of it.

The settling time for the system was quite long and the 2° C step size was established so that the experiment could show proof of concept in a reasonable amount of time. It initially appeared that there was hysteresis evident in the full temperature cycling from below the melting temperature to above the melting temperature and then back down to the initial starting temperature. This apparent hysteresis narrowed as dwell time before each measurement was increased. Various dwell times were investigated and the data indicated that the transition temperatures derived from the sigmoid function fits to the data from a complete temperature cycle were relatively insensitive to dwell times of an hour or more and temperature increments of 2° C or less. Given that the measurement system was not automated, a one hour dwell time before measurement and a 2° C measurement interval allowed a single cycle of measurements to be completed in a reasonable amount of time without a significant sacrifice in the accuracy of the results derived from the data.

Due to the limited number of measurement points and DNA sequences investigated, the results have been labeled as preliminary and more testing would need to be done to verify the results before this method can become a benchmark test for determining the melting temperature and binding energy of short sequences of DNA in solution. In future experiments, the density of measurement points, especially around the melting point should be significantly increased.

Experimental results

Using the experimental set-up shown in Figure 5-3, two sets of measurements were made. First, the dependence of the pure buffer solution as a function of temperature and frequency was determined. A combined data set consisting of four measurement runs on the buffer solution was created. This data set is shown in Figure 5-4a along with quadratic fits to the data. As can be seen, the values of the dielectric function varied smoothly in each case. Second order polynomial fits to the data (using the Kalidagraph® software package) are quantified in Table 5-1 where the quadratic form used was

Equation 5-3

$$\varepsilon = A + B\,T + C\,T^2$$

with ε being the real part of the dielectric function and T the temperature in °C.

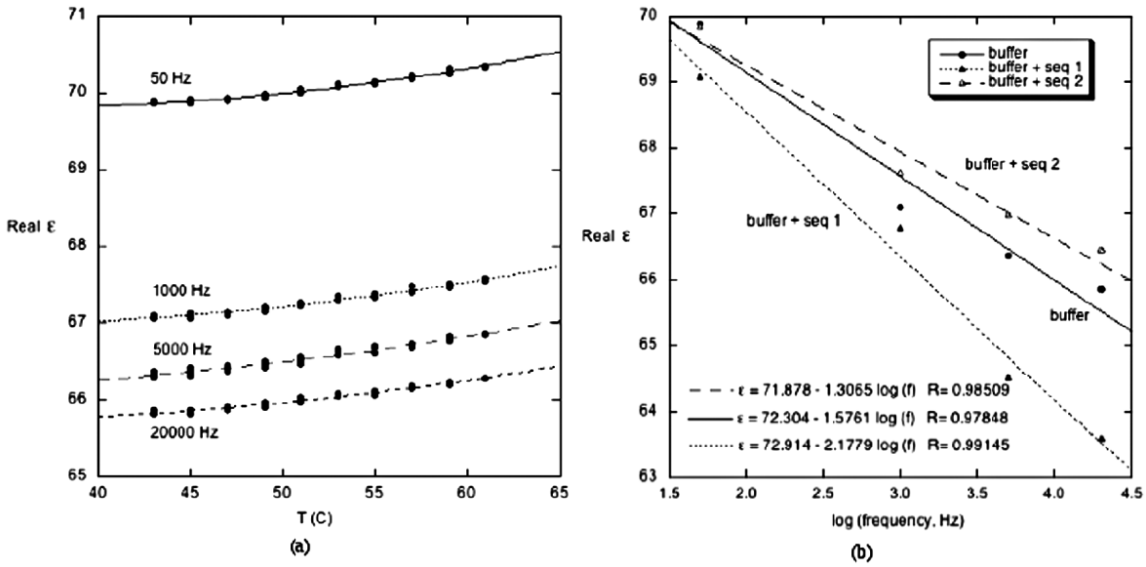

Figure 5-4 (a) Real ε *vs.* temperature for buffer solution at various frequencies, (b) real ε as a function of log (frequency) for buffer solution, buffer solution + sequence 1 and buffer solution + sequence 2, all at 45°C.

The effect of adding the DNA sequences to the buffer solution is shown in Figure 5-4b which is a plot of the dielectric functions of the buffer, buffer+sequence 1 and buffer+sequence 2 vs the log of the frequency, all at a temperature of 45° C. As can be seen, the principal changes induced by adding the DNA sequences to the buffer are to modify the solution dielectric function at constant frequency and to modify the rate of decrease of dielectric function as a function of frequency relative to the pure buffer solution. The addition of sequence 1 increases the rate of decrease while the addition of sequence 2 makes the rate of decrease smaller. For each solution, the rate of decrease of dielectric function in the log of frequency appears to be approximately linear.

Table 5-1 Quadratic fits to real ε vs. temperature in °C for the buffer solution used to suspend the DNA sequences

	A	B	C	*r*
ε (50 Hz)	70.8	–0.056	0.0008	0.990
ε (1 kHz)	67.5	–0.038	0.0006	0.988
ε (5 kHz)	66.3	–0.021	0.0005	0.979
ε (20 kHz)	66.1	–0.027	0.0005	0.986

Next, the dependence of the dielectric function of the buffer solution containing the DNA sequences as a function of temperature and frequency was measured. The result of these measurements is shown in Figure 5-5a and 5-5b for sequence 1 and sequence 2 respectively. As can be seen, the values of the dielectric function also varied smoothly in each case. A change in state can be seen to occur that can be identified with the sequence melting temperatures, T_m. The equation for the dielectric function as a function of

temperature is displayed as Equation 5-4 which follows from the melting point equation (3) detailed by SantaLucia [81].

Equation 5-4

$$\varepsilon = \varepsilon_z + (\varepsilon_m - \varepsilon_z)\frac{1}{1+e^{-\frac{\Delta S + R\cdot\ln C_T}{k}+\frac{\Delta H}{kT}}}$$

The ε_z parameter represents the relative dielectric function of the double stranded (ds) or zipped DNA while ε_m represents the dielectric function of the single stranded (ss) or melted DNA. C_T is the concentration of the dsDNA in solution in the zipped state, R is the universal gas constant and k is Boltzmann's constant. Kalidagraph® was used to solve for the melting entropy ΔS, and the melting enthalpy ΔH, which are displayed along with the theoretical values in Table 5-2. The left side of the table displays the entropy and enthalpy for the two sequences at each frequency tested, while the right half of the table displays the experimental averages, $\Delta S_{average}$ and $\Delta H_{average}$, and the theoretical results ΔS_{theory} and ΔH_{theory}, were calculated using the Nearest Neighbors method which compare favorably to our experimental results.

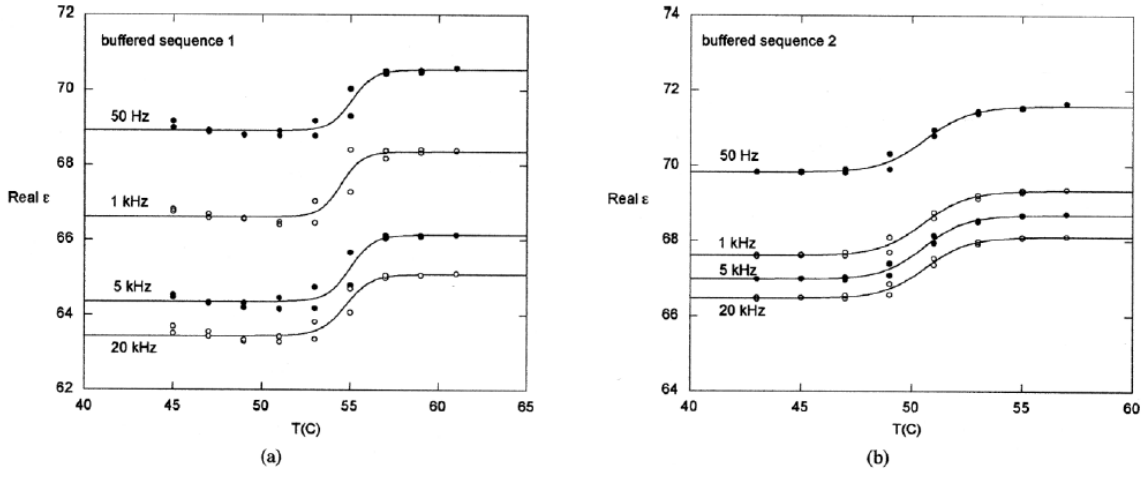

Figure 5-5 Real ε vs. temperature for (a) buffered sequence 1 and (b) buffered sequence 2

Table 5-2 Modified sigmoid function (Equation 5-4) fits to real ε vs. temperature in °C for the buffered solutions with DNA sequences 1 and 2

	ΔS_{ex}	ΔH_{ex}		$\Delta S_{average}$		$\Delta H_{average}$
	cal/K	**kcal/mol**		**cal/K mol**		**kcal/mol**
S1 (50 Hz)	661.2	188.8	S1	663.3	S1	189.4
S1 (1 kHz)	664.6	189.6	S2	429.5	S2	111.5
S1 (5 kHz)	662.5	189.2				
S1 (20 kHz)	664.9	189.9		ΔS_{theory}		ΔH_{theory}
S2 (50 Hz)	430.7	111.9		cal/K mol		kcal/mol
S2 (1 kHz)	429.2	111.4	S1	590.8	S1	224.0
S2 (5 kHz)	429.0	111.3	S2	328.3	S2	125.7
S2 (20 kHz)	428.9	111.3				

Figure 5-6 displays the different values of T_m obtained at the different frequencies based on the curve fits. The melting temperature for sequence 1 is about 54.9 °C and the melting temperature for sequence 2 is about 50.6 °C. The real dielectric function of the buffered ds DNA and ss DNA vary as a function of frequency as seen in Figure 5-7. The decrease in the real dielectric function is linear with the logarithm of the frequency which indicates that the DNA strands act as randomly oriented dipole moments which become polarized in the presence of an external electric field. These differences between the real dielectric function of ds and ss DNA for both sequences as a function of frequency can be seen in Table 5-3. Finally, Table 5-4 displays the base pair fractions within the two sequences along with the sequence lengths.

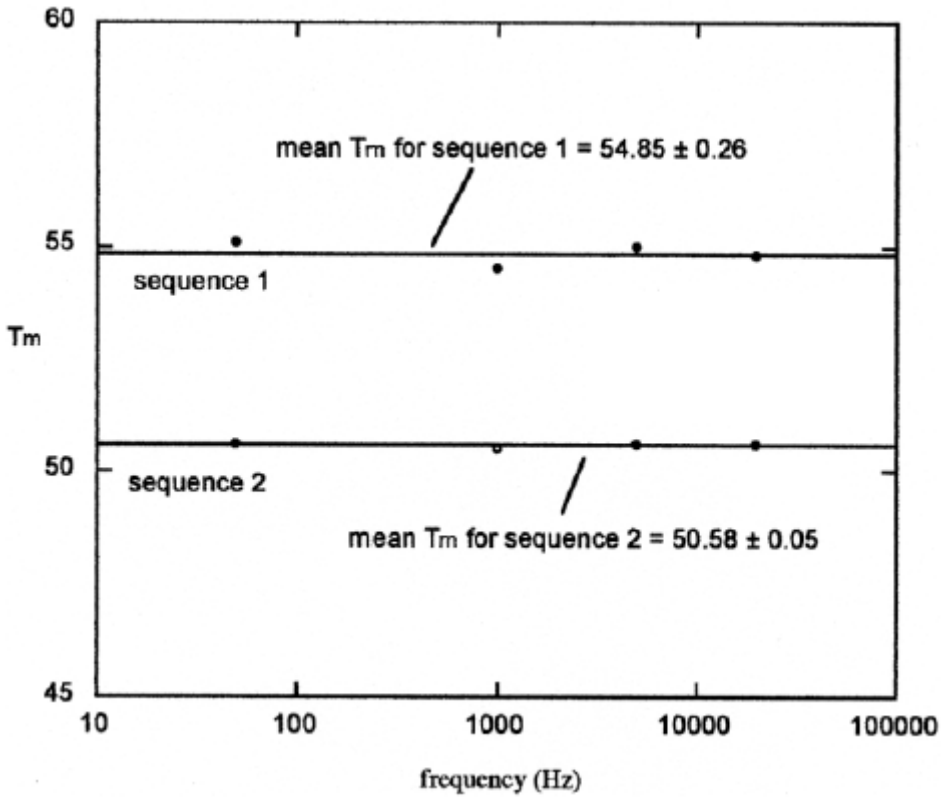

Figure 5-6 T_ms for both sequences

Table 5-3 Real ε of ds and ssDNA for sequences 1 and 2

	ε (1,ds)	ε (1,ss)	ε (2,ds)	ε (2,ss)
50 Hz	68.9 ± 0.1	70.5 ± 0.2	69.8 ± 0.1	71.6 ± 0.2
1 kHz	66.6 ± 0.1	68.3 ± 0.2	67.6 ± 0.1	69.3 ± 0.2
5 kHz	64.4 ± 0.1	66.2 ± 0.2	67.0 ± 0.1	68.7 ± 0.2
20 kHz	63.4 ± 0.1	65.0 ± 0.2	66.5 ± 0.1	68.1 ± 0.2

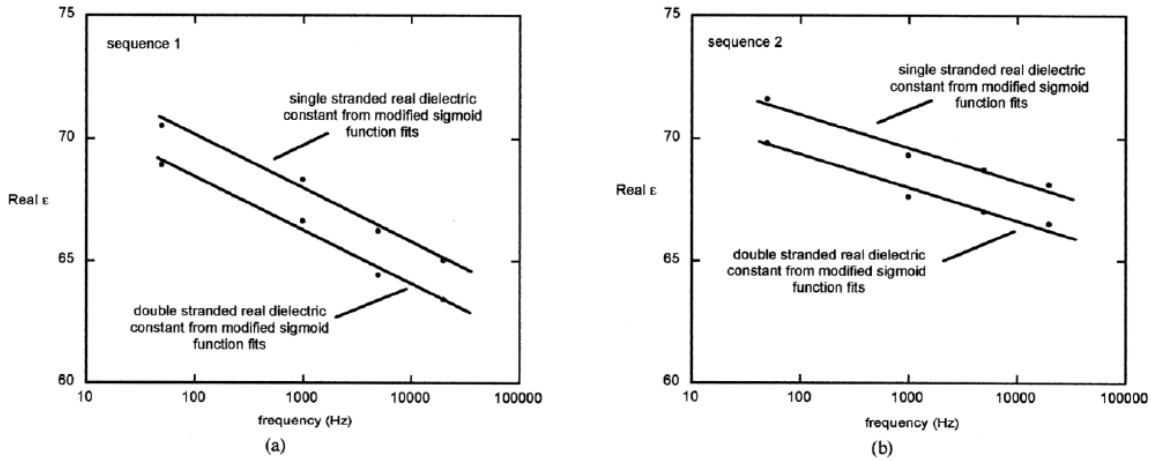

Figure 5-7 Real ε difference between ds and ss states for (a) sequence 1 and (b) sequence 2

Table 5-4 Base pair fractions and number of bp in the two sequences

	S1	S2
GC	15%	53%
CG	26%	7%
AT	48%	4%
TA	11%	0%
GC–CG	41%	60%
AT–TA	59%	40%
Number of bp	27	15

Using the 26 models described earlier to calculate T_m, Figure 5-8 (a) and (b) illustrates the predicted T_m values for DNA sequences 1 and 2, respectively. The histogram bars in Figure 5-8 are related to the references as indicated in Table 5-5. Figure 5-9 illustrate the mean and standard deviation ($\pm 1\sigma$) for these predicted T_m values based on i) the 26 models, ii) only the 3 salt corrected models, and iii) only the 22 nearest neighbors' thermodynamic models.

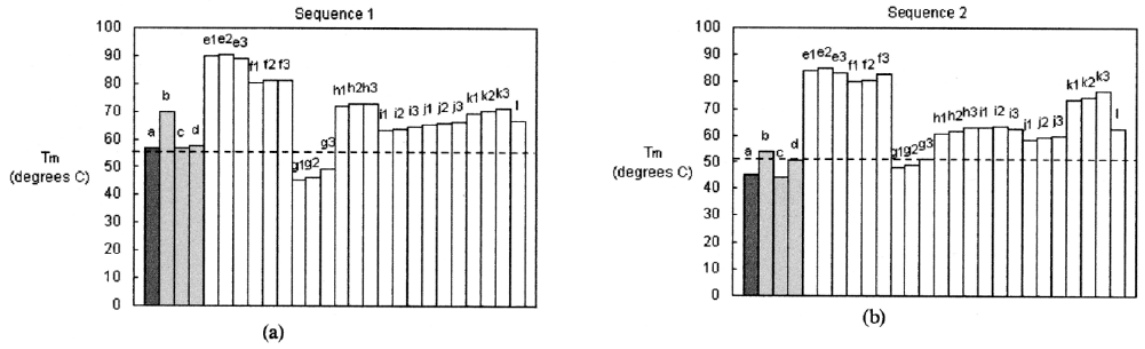

Figure 5-8 (a) Calculated melting temperature, Tm, for DNA sequence 1 (27 bases). In this histogram, the bars are numbered from a to l, corresponding to Tm values calculated using the basic model a, the salt-corrected models b–d, and the nearest neighbors' thermodynamic parameters e1–l. The numbers 1, 2, 3 next to the letters e–k correspond to ref. [81, 98, 102], salt correction term, respectively. The dashed line represents the value of Tm reported in this paper based on the dielectric measurements of DNA sequence 1 in solution. (b) Calculations repeated for sequence 2. The histogram bars are related to the references as indicated in Table 5-5.

Table 5-5 Relationship of references to histogram bars in Figure 5-8

Bar in histogram	Model used to calculate T_m	References
A	Basic model – Marmur, 1962	[26]
B	Salt-corrected model – Howley, 1979	[27]
C	Salt-corrected model – Rychlik, 1989	[28]
D	Salt-corrected model – Wetmur, 1991	[29]
e1	Nearest neighbors' model – Breslauer, 1986; Salt correction term – Wetmur, 1991	[30, 29]
e2	Nearest neighbors' model – Breslauer, 1986; Salt correction term – SantaLucia, 1996	[30, 34]
e3	Nearest neighbors' model– Breslauer, 1986; Salt correction term – SantaLucia, 1998	[30, 12]
f1	Nearest neighbors' model – Freier, 1986; Salt correction term – Wetmur, 1991	[31, 29]
f2	Nearest neighbors' model – Freier, 1986; Salt correction term – SantaLucia, 1996	[31, 34]
f3	Nearest neighbors' model – Freier, 1986; Salt correction term – SantaLucia, 1998	[31, 12]
g1	Nearest neighbors' model – Sugimoto, 1995; Salt correction term – Wetmur, 1991	[32, 29]
g2	Nearest neighbors' model – Sugimoto, 1995; Salt correction term – SantaLucia, 1996	[32, 34]
g3	Nearest neighbors' model – Sugimoto, 1995; Salt correction term – SantaLucia, 1998	[32, 12]
h1	Nearest neighbors' model – Sugimoto, 1996; Salt correction term – Wetmur, 1991	[33, 29]
h2	Nearest neighbors' model – Sugimoto, 1996; Salt correction term – SantaLucia, 1996	[33, 34]
h3	Nearest neighbors' model – Sugimoto, 1996; Salt correction term – SantaLucia, 1998	[33, 12]
i1	Nearest neighbors' model – SantaLucia, 1996; Salt correction term – Wetmur, 1991	[34, 29]
i2	Nearest neighbors' model – SantaLucia, 1996; Salt correction term – SantaLucia, 1996	[34, 34]
i3	Nearest neighbors' model – SantaLucia, 1996; Salt correction term – SantaLucia, 1998	[34, 12]
j1	Nearest neighbors' model – Allawi, 1997; Salt correction term – Wetmur, 1991	[35, 29]
j2	Nearest neighbors' model – Allawi, 1997; Salt correction term – SantaLucia, 1996	[35, 34]
j3	Nearest neighbors' model – Allawi, 1997; Salt correction term – SantaLucia, 1998	[35, 12]
k1	Nearest neighbors' model – Xia, 1998; Salt correction term – Wetmur, 1991	[36, 29]
k2	Nearest neighbors' model – Xia, 1998; Salt correction term – SantaLucia, 1996	[36, 34]
k3	Nearest neighbors' model – Xia, 1998; Salt correction term – SantaLucia, 1998	[36, 12]
L	Nearest neighbors' model – Allawi, 1997; Salt correction term – Owczarzy, 2004	[35, 11]

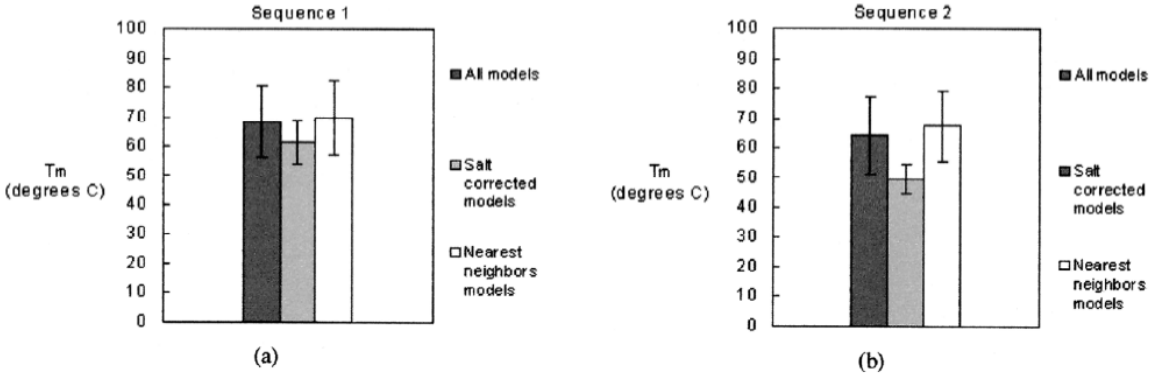

Figure 5-9 (a) Mean and SD for predicted T_m values for sequence 1 based on (i) all 26 models, (ii) only the 3 salt-corrected models, and (iii) only the 22 nearest neighbors' models. The error bar corresponds to ±1σ SD and (b) mean and SD for predicted T_m values for sequence 2 based on (i) all 26 models, (ii) only the 3 salt-corrected models, and (iii) only the 22 nearest neighbors' models. The error bar corresponds to ±1σ SD.

Analysis of results

Herein is described the results of a preliminary effort to develop a dielectric measurement and analysis protocol for determining the melting temperature of short double stranded sequences of DNA in solution. The steps involved in this protocol are:

1. Sample preparation (hybridized DNA sequence in solution).
2. Measurement of the real dielectric function of bulk fluid sample containing DNA as a function of temperature.
3. Fitting experimental data to a modified sigmoid function of the form indicated by the nearest neighbors method.
4. Extracting T_m from the modified sigmoid function fit.
5. Extracting the melting entropy and the melting enthalpy from the modified sigmoid function fit.

Use of this experimental and analytical protocol allows the melting temperature, T_m, of the DNA in solution to be accurately determined and the entropy and enthalpy to be estimated. The data from the limited experimental demonstration presented here supports the hypothesis that the order of the transition is second order due to the fact that no hysteresis was observed.

The development of an improved protocol for the determination of T_m can be seen to be of significance when consideration is given to the fact that the theoretical models used to predict T_m do vary and the most commonly used experimental techniques - spectroscopic and calorimetric - have relatively limited accuracy. The approach presented here and similar electrical measurement-based approaches [91] offer considerable promise that a new generation of high throughput and high accuracy techniques for determining T_m can provide

the basis for identifying which theoretical models most accurately describe the transition dynamics of DNA melting of short sequences in solution.

It is important to note what is not claimed here. There is a long history of the measurement of the dielectric and electronic properties of biological materials [92] with more than half a century of results published in the literature. It is also true that it is very difficult to infer the microscopic electrical properties of polar molecules in polar fluids [107]. No claims of measurement of the microscopic dielectric function, polarizability or conductivity of short sequences of DNA are made here. Instead, the macroscopic case of a bulk fluid containing short DNA sequences being interrogated at low frequency and low electric field strengths have been considered. The difference between the ds DNA and ss DNA manifests itself as a difference in the bulk real dielectric function of the fluid. From that difference the transition or DNA melting point can be estimated, as well as the entropy and enthalpy of the DNA sequence. All that is needed to do this is some quantitative measure of the transition from one form of DNA to the other. Doubtless, there are many other parameters that could have been measured, but the measurement protocol described here was found to be quite straightforward to implement and gave consistently repeatable results. These results can provide a test for any future theoretical analyses of these particular sequences suspended in this particular buffer fluid at the microscopic level.

Comparison with theoretical models

A recent study [94] has analyzed the correlation and similarities of the T_m values predicted using three thermodynamic parameter tables, which was also used for predicting T_m [100, 102, 104]. 108 random sequences were generated allowing for various salt concentrations and C/G content. These three models were found to correlate only for

simultaneously short sequences (i.e. between 16 and 18 base pairs) and C/G content comprised between 30 and 50%. The 2 sequences used in this study for dielectric measurements do not fall into this category, which agree with the observed large errors reported earlier. Although there have been 11 thermodynamic parameter tables reported in the literature [80], all the thermodynamic parameters calculations (i.e. enthalpy, entropy, and free energy transitions) have been based on oligonucleotide sequences containing at most 16 bases. Thus, these parameter tables, and therefore all nearest neighbors' models, are very accurate for short sequences with C/G content within 30 to 50%, but otherwise induce significant disagreement in the prediction of T_m. Accurate determination of T_m has to be done empirically.

Note that the measured values for T_m based on dielectric measurements (i.e. T_m=54.9±0.3° C and 50.6±0.1° C for sequences 1 and 2, respectively) fall within 1.64 σ from the mean. Given the larger variation within all 26 predicted T_m values, the methodology presented here for determining T_m gives results that are comparable to predicted T_m values. In particular, the advantages of using dielectric measurements for determination of T_m include small standard deviation and transition width.

Finally, novel T_m prediction methods which use different thermodynamic parameters such as a recently published consensus T_m calculation method [108] claim to provide more accurate calculations of DNA T_m's based on correlation studies. These consensus T_m calculation methods have not been used in this preliminary study but could be considered for use in future work.

Suggestions for future work

The results presented here only represent a demonstration of principle. In order for the protocol's real value to be established, an extensive study involving a large number of different DNA sequences needs to be conducted. In such a study, the T_m of each sequence should be determined according to protocol and compared with spectroscopic and calorimetric determinations of T_m. In the longer term, devices need to be developed to reduce the measurement time and to increase the throughput. Such a device could be implemented using bridge circuits as shown in Figure 5-10. In Figure 5-10a the basic bridge circuit is shown for one element of a conceptual microfluidic device for measuring the T_m's of a large number of DNA sequences simultaneously. The impedance Z1 is assumed to be the impedance of a fluid chamber containing buffer solution only. The impedance Z2 is assumed to be the impedance of a companion fluid chamber containing double stranded DNA molecules suspended in buffer. If the two impedances are the same, the voltage differential between points 1 and 2 on the bridge will be $\Delta V = 0$. ΔV will then provide a measure of the difference between the impedances of the buffer+cell and DNA+buffer+cell. Qualitatively, one would expect to see ΔV vary with temperature as shown in Figure 5-10b and allow accurate determination of T_m according to the protocol described above. The experimental set-up for a self-contained device is shown in Figure 5-10c while a single element of the device is shown schematically in Figure 5-10d. Finally, the electrode configuration for a single sample chamber is shown schematically edge-on in Figure 5-10e.

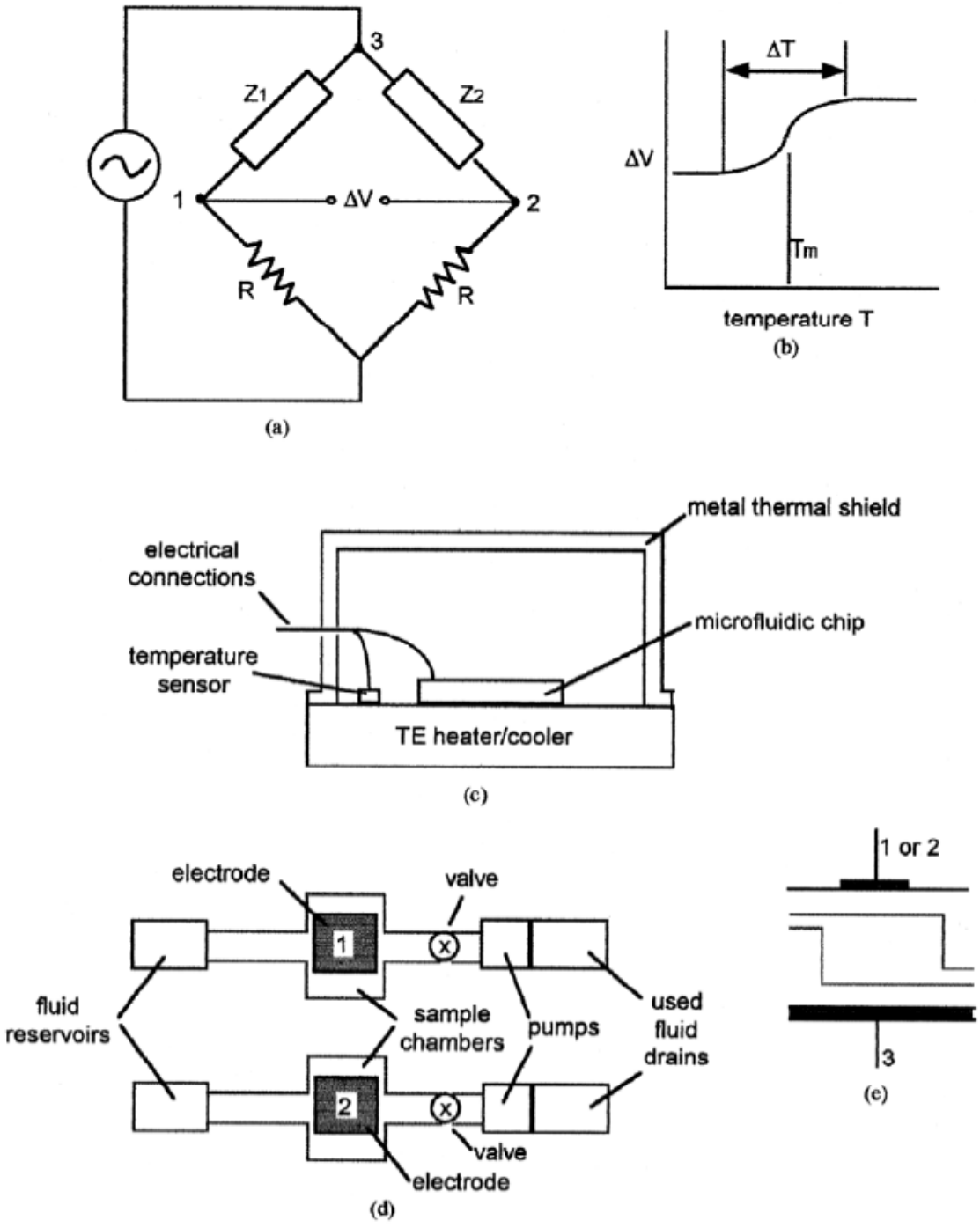

Figure 5-10 Advanced device concept sketches: (a) bridge circuit measurement configuration, (b) anticipated output, (c) measurement setup, (d) top view/one element, and (e) electrode configuration for single sample chamber, edge view.

Device operation would include filling the fluid reservoirs with pure buffer or DNA+buffer as appropriate, opening the microfluidic valves and pumping until the sample chambers were full. The valves would then be closed and the temperature of the thermoelectric cooler would be stepped through an appropriate temperature range with the temperature T and the voltage difference ΔV recorded digitally at each step. When the measurements have been completed, the valves would be opened again and the fluid in the system would be pumped into the used fluid drain reservoirs, the system purged with buffer, and the valves would be closed. The data obtained would then be processed digitally to determine the T_m's and an estimate made of the binding energies of each molecule in solution.

Although the microfluidic concept presented here might not be implemented in the detail shown, nonetheless, any practical high throughput device will probably follow the same design principles. Future work could be focused in two areas: (1) the design and completion of a study using the protocol and equipment on hand to investigate the properties of a significant number of different short DNA sequences as we have previously described, and (2) to begin the development of a high throughput microfluidic device to make these measurements more accessible and practical for the scientific community [4].

REFERENCES

1. Geist, B., W.B. Spillman, and R.O. Claus, *Thermal cycling and the optical and electrical characterization of self-assembled multilayer Nile Blue A-gold thin films.* Applied Optics, 2005. **44**(30): p. 6357-6360.
2. Asmatulu, R., et al., *Dielectric constant and breakdown field studies of electrostatic self-assembled materials.* Smart Materials & Structures, 2005. **14**(6): p. 1493-1500.
3. Dickerson, B.D., et al., *Canine cancer screening via ultraviolet absorbance and fluorescence spectroscopy of serum proteins.* Applied Optics, 2007. **46**(33): p. 8080-8088.
4. Spillman, W.B., Jr., et al., *Preliminary dielectric measurement and analysis protocol for determining the melting temperature and binding energy of short sequences of DNA in solution.* Biotechnol J, 2008. **3**(2): p. 252-63.
5. Decher, G. and J.B. Schlenoff, *Multilayer thin films : sequential assembly of nanocomposite materials.* 2003, Weinheim: Wiley-VCH. xix, 524 p.
6. Liu, Y.J., A.B. Wang, and R. Claus, *Molecular self-assembly of TiO2/polymer nanocomposite films.* Journal of Physical Chemistry B, 1997. **101**(8): p. 1385-1388.
7. Liu, Y.J. and R.O. Claus, *Strong enhancement of optical absorbance from ionic self-assembled multilayer thin films of nanocluster Pt and polymer dye.* Journal of Applied Physics, 1999. **85**(1): p. 419-424.
8. Liu, Y.J., Y.X. Wang, and R.O. Claus, *Layer-by-layer ionic self-assembly of Au colloids into multilayer thin-films with bulk metal conductivity.* Chemical Physics Letters, 1998. **298**(4-6): p. 315-319.
9. Okamoto, T., I. Yamaguchi, and T. Kobayashi, *Local plasmon sensor with gold colloid monolayers deposited upon glass substrates.* Opt. Lett., 2000. **25**(6): p. 372-374.

10. Enejder, A.M.K., et al., *Raman spectroscopy for noninvasive glucose measurements.* Journal of Biomedical Optics, 2005. **10**(3): p. 031114-9.

11. McCain, S.T., et al., *Multimodal multiplex Raman spectroscopy optimized for in vivo chemometrics - art. no. 60930F.* Biomedical Vibrational Spectroscopy III: Advances in Research and Industry, 2006. **6093**: p. F930-F930

278.

12. Huang, Z.W., et al., *Raman spectroscopy of in vivo cutaneous melanin.* Journal of Biomedical Optics, 2004. **9**(6): p. 1198-1205.

13. Jemal, A., et al., *Cancer Statistics, 2005.* CA Cancer J Clin, 2005. **55**(1): p. 10-30.

14. Nie, S. and S.R. Emory, *Probing Single Molecules and Single Nanoparticles by Surface-Enhanced Raman Scattering.* Science, 1997. **275**(5303): p. 1102-1106.

15. Qian, X.M., et al., *In vivo tumor targeting and spectroscopic detection with surface-enhanced Raman nanoparticle tags.* Nature Biotechnology, 2008. **26**(1): p. 83-90.

16. Cotran, R.S., et al., *Robbins pathologic basis of disease.* 6th ed. 1999, Philadelphia: Saunders. xv, 1424 p.

17. Mycek, M.-A. and B.W. Pogue, *Handbook of biomedical fluorescence.* 2003, New York: Marcel Dekker. xv, 665 p.

18. Diamandis, E.P., *How are we going to discover new cancer biomarkers? A proteomic approach for bladder cancer.* Clinical Chemistry, 2004. **50**(5): p. 793-795.

19. Gad, S.C., *Drug discovery handbook.* 2005, Hoboken, N.J.: Wiley-Interscience. xix, 1471 p.

20. Pritzker, K.P.H., *Cancer biomarkers: Easier said than done.* Clinical Chemistry, 2002. **48**(8): p. 1147-1150.

21. Aebersold, R. and M. Mann, *Mass spectrometry-based proteomics.* Nature, 2003. **422**(6928): p. 198-207.

22. Li, J.N., et al., *Proteomics and bioinformatics approaches for identification of serum biomarkers to detect breast cancer.* Clinical Chemistry, 2002. **48**(8): p. 1296-1304.

23. Statnikov, A., et al., *A comprehensive evaluation of multicategory classification methods for microarray gene expression cancer diagnosis.* Bioinformatics, 2005. **21**(5): p. 631-643.

24. Pineda, A.A., *Selective plasma component removal.* 1984, Mount Kisco, N.Y.: Futura Pub. Co. xii, 214 p.

25. Law, M.R., et al., *Serum albumin and mortality in the BUPA study. British United Provident Association.* Int J Epidemiol, 1994. **23**(1): p. 38-41.

26. Darne, B., P. Ducimetiere, and L. Guize, *Serum-Albumin and Mortality.* Lancet, 1990. **335**(8685): p. 350-351.

27. Stevens, R.G., et al., *Body iron stores and the risk of cancer.* N Engl J Med, 1988. **319**(16): p. 1047-52.

28. Feldman, B.V., et al., *Schalm's veterinary hematology / editors, Bernard V. Feldman, Joseph G. Zinkl, Nemi C. Jain.* 5th ed. 2000, Philadelphia: Lippincott Williams & Wilkins. xxxi, 1344 p.

29. Hubmann, M.R., M.J.P. Leiner, and R.J. Schaur, *Ultraviolet Fluorescence of Human Sera .1. Sources of Characteristic Differences in the Ultraviolet Fluorescence-Spectra of Sera from Normal and Cancer-Bearing Humans.* Clinical Chemistry, 1990. **36**(11): p. 1880-1883.

30. Welle, S., *Human protein metabolism*. 1999, New York: Springer. xi, 288 p.

31. Henry, R.J., D.C. Cannon, and J.W. Winkelman, *Clinical chemistry; principles and technics.* 2d ed. 1974, Hagerstown, Md.,: Medical Dept. xii, 1629 p.

32. Beri, R. and R. Chandra, *Chemistry and Biology of Heme - Effect of Metal-Salts, Organometals, and Metalloporphyrins on Heme-Synthesis and Catabolism, with Special Reference to Clinical Implications and Interactions with Cytochrome-P-450.* Drug Metabolism Reviews, 1993. **25**(1-2): p. 49-152.

33. Kondo, M., et al., *Heme-Biosynthetic Enzyme-Activities and Porphyrin Accumulation in Normal Liver and Hepatoma-Cell Lines of Rat.* Cell Biology and Toxicology, 1993. **9**(1): p. 95-105.

34. Munson, B.R., *A review: biochemical alterations associated with mouse spleen cells infected with Friend virus.* Journal of medicine, 1973. **4**: p. 354-370.

35. Harris, D.M. and J. Werkhaven, *Endogenous porphyrin fluorescence in tumors.* Lasers Surg Med, 1987. **7**(6): p. 467-72.

36. Jichlinski, P., et al., *Clinical evaluation of a method for detecting superficial surgical transitional cell carcinoma of the bladder by light-induced fluorescence of protoporphyrin IX following the topical application of 5-aminolevulinic acid: preliminary results.* Lasers Surg Med, 1997. **20**(4): p. 402-8.

37. Mang, T.S., et al., *Fluorescence Detection of Tumors - Early Diagnosis of Microscopic Lesions in Preclinical Studies.* Cancer, 1993. **71**(1): p. 269-276.

38. Leca-Bouvier, B. and L.J. Blum, *Biosensors for protein detection: A review.* Analytical Letters, 2005. **38**(10): p. 1491-1517.

39. Sapan, C.V., R.L. Lundblad, and N.C. Price, *Colorimetric protein assay techniques.* Biotechnology and Applied Biochemistry, 1999. **29**: p. 99-108.

40. Weiss, M., *Utility of follow-up tests for detecting recurrent disease in patients with malignant melanomas.* Journal of the American Medical Association, 1995. **274**(21): p. 1703-1705.

41. Pena, L., et al., *Canine inflammatory mammary carcinoma: histopathology, immunohistochemistry and clinical implications of 21 cases.* Breast Cancer Res Treat, 2003. **78**(2): p. 141-8.

42. Elhadj, S., G. Singh, and R.F. Saraf, *Optical Properties of an Immobilized DNA Monolayer from 255 to 700 nm.* Langmuir, 2004. **20**(13): p. 5539-5543.

43. Luo, D., *The road from biology to materials.* Materials Today, 2003. **6**(11): p. 38-43.

44. Zaludova, R., V. Kleinwachter, and V. Brabec, *The effect of ionic strength on melting of DNA modified by platinum(II) complexes.* Biophysical Chemistry, 1996. **60**(3): p. 135-142.

45. Calladine, C.R. and H.R. Drew, *Understanding DNA : the molecule & how it works.* 2nd ed. 1997, San Diego, Calif.: Academic Press. xi, 283 p.

46. Pedone, F., F. Mazzei, and D. Santoni, *Sequence-dependent DNA torsional rigidity: a tetranucleotide code.* Biophysical Chemistry, 2004. **112**(1): p. 77-88.

47. Armitage, N.P., M. Briman, and G. Gruner, *Charge transfer and charge transport on the double helix.* Physica Status Solidi B-Basic Research, 2004. **241**(1): p. 69-75.

48. Cai, L., H. Tabata, and T. Kawai, *Self-assembled DNA networks and their electrical conductivity.* Applied Physics Letters, 2000. **77**(19): p. 3105-3106.

49. Fornes, J.A., *Dielectric relaxation around a charged colloidal cylinder in an electrolyte.* Journal of Colloid and Interface Science, 2000. **222**(1): p. 97-102.

50. Natarajan, G., R. Malathi, and E. Holler, *Helix-coil transitions in DNA using a pH variation method: Case of a melting paradox as a function of ionic strength.* Analytical Biochemistry, 1996. **237**(1): p. 152-155.

51. Rouzina, I. and V.A. Bloomfield, *Force-induced melting of the DNA double helix. 2. Effect of solution conditions.* Biophysical Journal, 2001. **80**(2): p. 894-900.

52. Glass, A.M., et al., *Interaction of Metal Particles with Absorbed Dye Molecules - Absorption and Luminescence.* Optics Letters, 1980. **5**(9): p. 368-370.

53. Chen, S.W., *Self-assembling of monolayer-protected gold nanoparticles.* Journal of Physical Chemistry B, 2000. **104**(4): p. 663-667.

54. Sih, B.C., A. Teichert, and M.O. Wolf, *Electrodeposition of oligothiophene-linked gold nanoparticle films.* Chemistry of Materials, 2004. **16**(14): p. 2712-2718.

55. Takei, H., *Surface-adsorbed polystyrene spheres as a template for nanosized metal particle formation: Optical properties of nanosized Au particle.* Journal of Vacuum Science & Technology B, 1999. **17**(5): p. 1906-1911.

56. Fang, H.J., et al., *Self-assembly of the [60]fullerene-substituted oligopyridines on Au nanoparticles and the optical nonlinearities of the nanoparticles.* Chemical Physics Letters, 2002. **364**(3-4): p. 290-296.

57. Park, S.Y., *Structure formation, melting, and optical properties of gold/DNA nanocomposites: effects of relaxation time.* Physical Review B, 2003. **68**(22): p. 224201-01-11.

58. Ho, P.S., J. Leu, and W.W. Lee, *Low dielectric constant materials for IC applications.* Springer series in advanced microelectronics,. 2003, Berlin ; New York: Springer. xix, 309 p.

59. Nalwa, H.S., *Handbook of low and high dielectric constant materials and their applications.* 1999, San Diego: Academic Press.

60. Callister, W.D., *Materials science and engineering : an introduction.* 5th ed. 2000, New York: Wiley. xxi, 871 p.

61. Dakhel, A.A., *Dielectric and optical properties of samarium oxide thin films.* Journal of Alloys and Compounds, 2004. **365**(1-2): p. 233-239.

62. Mathai, C.J., et al., *Characterization of low dielectric constant polyaniline thin film synthesized by ac plasma polymerization technique.* Journal of Physics D-Applied Physics, 2002. **35**(3): p. 240-245.

63. Paddison, S.J., D.W. Reagor, and T.A. Zawodzinski, *High frequency dielectric studies of hydrated Nafion (R).* Journal of Electroanalytical Chemistry, 1998. **459**(1): p. 91-97.

64. Sahu, D.R., et al., *Effect of thermal plasma heating on the dielectric properties of Al-Zr composites.* Proceedings of the Institution of Mechanical Engineers Part L-Journal of Materials-Design and Applications, 2002. **216**(L2): p. 127-132.

65. Velumani, S., et al., *Dielectric and conduction studies on hot-wall deposited CdSe films.* Solar Energy Materials and Solar Cells, 2004. **81**(3): p. 323-338.

66. Wagle, S. and V. Shirodkar, *Dielectric properties of thin film Al-1/Sb2Pb1Se7/Al devices.* Brazilian Journal of Physics, 2000. **30**(3): p. 554-559.

67. Lehninger, A.L., D.L. Nelson, and M.M. Cox, *Lehninger principles of biochemistry.* 5th ed. 2008, New York: W.H. Freeman. 1 v. (various pagings).

68. Biloiu, C., et al., *Amorphous fluorocarbon polymer (a-C : F) films obtained by plasma enhanced chemical vapor deposition from perfluoro-octane (C8F18) vapor. II. Dielectric and insulating properties.* Journal of Vacuum Science & Technology A, 2004. **22**(4): p. 1158-1165.

69. Wu, Z.-S., et al., *Gold colloid-bienzyme conjugates for glucose detection utilizing surface-enhanced Raman scattering.* Talanta, 2006. **70**(3): p. 533-539.

70. Stiles, P.L., et al., *Surface-Enhanced Raman Spectroscopy.* Annual Review of Analytical Chemistry, 2008. **1**(1): p. 601-626.

71. Fleischmann, M., P.J. Hendra, and A.J. McQuillan, *Raman spectra of pyridine adsorbed at a silver electrode.* Chemical Physics Letters, 1974. **26**(2): p. 163-166.

72. Jeanmaire, D.L. and R.P. Van Duyne, *Surface raman spectroelectrochemistry: Part I. Heterocyclic, aromatic, and aliphatic amines adsorbed on the anodized silver electrode.* Journal of Electroanalytical Chemistry, 1977. **84**(1): p. 1-20.

73. Albrecht, M.G. and J.A. Creighton, *Anomalously intense Raman spectra of pyridine at a silver electrode.* Journal of the American Chemical Society, 1977. **99**(15): p. 5215-5217.

74. Gersten, J.I., *Theory of Surface Plasmarons .2. The Effect of a Finite Thickness of the Accumulation Layer.* Surface Science, 1980. **97**(1): p. 206-218.

75. Gersten, J.I., *The Effect of Surface-Roughness on Surface Enhanced Raman-Scattering.* Journal of Chemical Physics, 1980. **72**(10): p. 5779-5780.

76. Gersten, J.I., *Theory of Surface Plasmarons.* Surface Science, 1980. **92**(2-3): p. 579-592.

77. Kerker, M., D.S. Wang, and H. Chew, *Surface Enhanced Raman-Scattering (Sers) by Molecules Adsorbed at Spherical-Particles.* Applied Optics, 1980. **19**(19): p. 3373-3388.

78. Moskovits, M., *Surface-Enhanced Spectroscopy.* Reviews of Modern Physics, 1985. **57**(3): p. 783-826.

79. Haynes, C.L., et al., *Nanoparticles with Tunable Localized Surface Plasmon Resonances*, in *Radiative Decay Engineering.* 2005. p. 47-99.

80. Owczarzy, R., et al., *Effects of sodium ions on DNA duplex oligomers: Improved predictions of melting temperatures.* Biochemistry, 2004. **43**(12): p. 3537-3554.

81. SantaLucia, J., *A unified view of polymer, dumbbell, and oligonucleotide DNA nearest-neighbor thermodynamics.* Proceedings of the National Academy of Sciences of the United States of America, 1998. **95**(4): p. 1460-1465.

82. Owczarzy, R., et al., *Thermodynamic treatment of oligonucleotide duplex-simplex equilibria.* Proceedings of the National Academy of Sciences of the United States of America, 2003. **100**(25): p. 14840-14845.

83. Owczarzy, R., *Melting temperatures of nucleic acids: Discrepancies in analysis.* Biophysical Chemistry, 2005. **117**(3): p. 207-215.

84. Duguid, J.G., et al., *DNA melting investigated by differential scanning calorimetry and Raman spectroscopy.* Biophysical Journal, 1996. **71**(6): p. 3350-3360.

85. Plum, G.E., et al., *Thermodynamic Characterization of the Stability and the Melting Behavior of a DNA Triplex - a Spectroscopic and Calorimetric Study.* Proceedings of the National Academy of Sciences of the United States of America, 1990. **87**(23): p. 9436-9440.

86. Zeng, Y., A. Montrichok, and G. Zocchi, *Length and statistical weight of bubbles in DNA melting.* Physical Review Letters, 2003. **91**(14): p. -.

87. Privalov, G., et al., *Precise Scanning Calorimeter for Studying Thermal-Properties of Biological Macromolecules in Dilute-Solution.* Analytical Biochemistry, 1995. **232**(1): p. 79-85.

88. Liu, Y. and J.M. Sturtevant, *Significant discrepancies between van't Hoff and calorimetric enthalpies. II.* Protein Sci, 1995. **4**(12): p. 2559-61.

89. Wu, P., S. Nakano, and N. Sugimoto, *Temperature dependence of thermodynamic properties for DNA/DNA and RNA/DNA duplex formation.* European Journal of Biochemistry, 2002. **269**(12): p. 2821-2830.

90. Allgen, L.G., *A dielectric study of nucleohistone from calf thymus.* Acta Physiol Scand Suppl, 1950. **22**(76): p. 1-140.

91. Archer, M., M. Christophersen, and P.M. Fauchet, *Macroporous silicon electrical sensor for DNA hybridization detection.* Biomed Microdevices, 2004. **6**(3): p. 203-11.

92. Pethig, R., *Dielectric and electronic properties of biological materials.* 1979, Chichester, [Eng.] ; New York: Wiley. xiv, 376 p.

93. Takashima, S., *Study of helix-coil transition of DNA by dielectric constant measurement.* Biopolymers, 1966. **4**(6): p. 663-76.

94. Panjkovich, A. and F. Melo, *Comparison of different melting temperature calculation methods for short DNA sequences.* Bioinformatics, 2005. **21**(6): p. 711-22.

95. Marmur, J. and P. Doty, *Determination of the base composition of deoxyribonucleic acid from its thermal denaturation temperature.* J Mol Biol, 1962. **5**: p. 109-18.

96. Howley, P.M., et al., *A rapid method for detecting and mapping homology between heterologous DNAs. Evaluation of polyomavirus genomes.* J Biol Chem, 1979. **254**(11): p. 4876-83.

97. Rychlik, W. and R.E. Rhoads, *A computer program for choosing optimal oligonucleotides for filter hybridization, sequencing and in vitro amplification of DNA.* Nucleic Acids Res, 1989. **17**(21): p. 8543-51.

98. Wetmur, J.G., *DNA probes: applications of the principles of nucleic acid hybridization.* Crit Rev Biochem Mol Biol, 1991. **26**(3-4): p. 227-59.

99. Allawi, H.T. and J. SantaLucia, Jr., *Thermodynamics and NMR of internal G.T mismatches in DNA.* Biochemistry, 1997. **36**(34): p. 10581-94.

100. Breslauer, K.J., et al., *Predicting DNA duplex stability from the base sequence.* Proc Natl Acad Sci U S A, 1986. **83**(11): p. 3746-50.

101. Freier, S.M., et al., *Improved free-energy parameters for predictions of RNA duplex stability.* Proc Natl Acad Sci U S A, 1986. **83**(24): p. 9373-7.

102. SantaLucia, J., Jr., H.T. Allawi, and P.A. Seneviratne, *Improved nearest-neighbor parameters for predicting DNA duplex stability.* Biochemistry, 1996. **35**(11): p. 3555-62.

103. Sugimoto, N., et al., *Thermodynamic parameters to predict stability of RNA/DNA hybrid duplexes.* Biochemistry, 1995. **34**(35): p. 11211-6.

104. Sugimoto, N., et al., *Improved thermodynamic parameters and helix initiation factor to predict stability of DNA duplexes.* Nucleic Acids Res, 1996. **24**(22): p. 4501-5.

105. Xia, T., et al., *Thermodynamic parameters for an expanded nearest-neighbor model for formation of RNA duplexes with Watson-Crick base pairs.* Biochemistry, 1998. **37**(42): p. 14719-35.

106. Fraden, J. and American Institute of Physics., *AIP handbook of modern sensors : physics, designs, and applications*. Modern instrumentation and measurements in physics & engineering. 1993, New York: American Institute of Physics. xiii, 552 p.

107. Scaife, B.K.P., *Complex permittivity: theory and measurement*. Science and technology series. 1971, London,: English Universities Press. vi, 170 p.

108. Panjkovich, A., T. Norambuena, and F. Melo, *dnaMATE: a consensus melting temperature prediction server for short DNA sequences*. Nucleic Acids Res, 2005. **33**(Web Server issue): p. W570-2.